University of Bath

UNIVERSITY OF BATH

PHD

Nonlinear optical phenomena in fluoride glass and hybrid fibres

Fischbach, Stefan

Award date:
2017

Awarding institution:
University of Bath

Link to publication

Nonlinear optical phenomena in fluoride glass and hybrid fibres

Stefan Fischbach

A thesis submitted for the degree of Doctor of Philosophy

University of Bath

Department of Physics

February 7, 2017

Abstract

This thesis investigates nonlinear optical phenomena in non-silica fibres, in a first part utilising a fluoride fibre, followed by the exploration of hybrid fibres with an organic single crystal inside a fibre capillary. The unique properties of $55ZrF_4$, $18BaF_2$, $6LaF_3$, $4AlF_3$, $17Na_F$ (ZBLAN) glass allow the creation of optical fibres with a highly extended transmission window on the longer wavelength side. We investigated the properties of ZBLAN fibres in order to optimise supercontinuum (SC) generation in a ZBLAN fibre pumped by an optic parametric amplifier. To study applications of the ZBLAN SC we integrated the SC into a pump-probe setup, being used as a near-infrared broadband probe source. We have carried out proof-of-principle measurements on an organic copolymer thin-film, showing the possibility of utilising a ZBLAN SC, allowing to extend the usability of broadband sources to the near- and mid-infrared, while simplifying the usage of the setup.

The second part of this thesis explores the possibilities of hybrid fibres by using a hollow-core silica capillary with an organic single-crystal inside. We have developed and optimised a method to grow an organic semiconducting crystal inside a hollow core capillary based on the Bridgman-technique. We could demonstrate the filling of the inner capillary for diameters down to 1 µm and with different materials based on the anthracene structure, opening up possibilities for various hybrid fibres. The quality of the single-crystals was evaluated by micro-Raman and X-ray diffraction measurements. We could access nonlinear properties of the crystal by coupling light with an energy lower than the band-gap into the fibre. Stimulated by two-photon absorption photo-luminescence from the fibre core was observed for the hybrid fibre. The results obtained for the hybrid fibres gives rise to a vast amount of possibilities for different hybrid fibres with tailored optical properties of organic materials and their optimisation in the guiding of light.

Acknowledgements

First of all I want to thank my supervisor Dr. Enrico Da Como for the great opportunity to my Ph.D. in his research group. Not only has he helped me with his knowledge of photonics and opto-electronics, but also the various discussions about scientific and experimental topics have shown new ways to go with my research. Thank you for your support and advise making this thesis possible.

Thanks to the members of our group and final year students working with us, who kept the work fun and made it interesting. I especially want to thank Daniele, Tommaso, Harry, Sam, Sara and Rebecca for the time together.

Working together with the CPPM allowed me to benefit of their great facilities for fibre related research. The knowledge about optical fibres in the group was very helpful and I especially want to thank Jonathan Knight, William Wadsworth, Andriy Gorbach, Jim Stone and Fei Yu for their help with the understanding of fibre optical processes, theoretical models and experimental use.

My work would not have been possible without the continuous involvement of your technicians. In the first place Harry Bone helped whenever there was a problem coming up and found fast solutions. Paul Reddish built and repaired various parts to the specifications I needed. Wendy Lambson provided support in the various chemical problems. Edwina Wilkinson relentlessly carried out purchases of consumables, parts and devices for us. Alan George, Simon Dodd,Ashley Brewer, Jennifer Williams,Steven Renshaw and Peter Sykes where a big help with various tasks of running our lab safe and efficiently.

Not to be missed in this list are my parents who ultimately allowed me to pursue my scientific education up to my Ph.D.. They gave me the support where it was needed, and let me choose my way independently where I was going my way.

Last but not least I want to thank Natasha for being with through this whole time, making times more enjoyable, sometimes more endurable and keep looking forward.

Contents

Contents

Contents

References   **139**

Appendix   **155**

Contents

2

1 Introduction

Optical spectroscopy studies the interaction of light - or more general electromagnetic radiation - with matter as a function of wavelength. In the 17th century spectroscopy started to develop with its most famous researcher being Isaac Newton [1]. First experiments used the dispersion of visible, white light in a glass prism [2]. But only in the second half of the 19th century spectroscopes were used as devices to study material properties more systematically [3].

Spectroscopy is not limited to visible light, but the source of electromagnetic radiation used strongly dictates which types of interactions and phenomena can be probed. The whole spectrum of photons can be used with wavelengths in the range of microwaves and Terahertz [4] on the one end and x-rays [5] and gamma-radation [6] on the high energetic end of the available spectrum. The different types of interaction between photons and matter - absorption, emission, reflection, elastic and inelastic scattering to name some - give rise to a vast amount of different spectroscopical techniques from which one can choose the suitable method for the desired materials and phenomena to study [7].

With the presentation of the first working laser in 1960 by Theodore Maiman [8] the basis for many new applications was set as for the first time coherent light sources with high intensities became available. One of the fields highly benefiting from the invention of the laser is nonlinear optics (NLO), needing high, coherent light intensities. Second harmonic generation was observed in 1961 for the first time [9] and followed by an ever increasing amount of research [10], [11].

Laser technology and nonlinear optics are highly connected to each other as lasers allowed nonlinear effects to be experimentally observed while the available bandwidth of lasers gained from nonlinear effects. Nd:YAG lasers

with the most intense lasing line at 1064 nm [12] are often used to generate a frequency doubled output at 532 nm [13]. The titanium-sapphire laser [14] can be mode-locked, utilising the Kerr-effect to generate pulses with a temporal length in the fs range [15] and high peak intensities. Optical parametric amplification or generation, first demonstrated in 1965 [16], is used to created tunable laser sources, adding more flexibility for many experiments.

The generation of femtosecond or attosecond laser pulses also opens up the possibility to observe many opto-electronic processes in real time using time-resolved spectroscopy methods [17]. The time resolution is ultimately limited by the temporal width of the probing light pulse interacting with matter [18].

In the scope of this work femtosecond pulses have been used for transient absorption measurements. With the photon wavelength defining the allowed interactions between photons and matter to be probed, many interesting optical resonances of semiconductors or semimetals, ascribed to phonons, polarons or intersubband transitions, can be found in the near- (NIR) or mid-infrared (MIR) [19]. While for visible and NIR light broadband laser sources are available thanks to supercontinuum generation, the situation changes for longer wavelengths. In most pump-probe configurations for MIR experiments parametric amplification or generation is used to obtain a tunable source for probe pulses and a photoexcitation of the sample with visible light [20], [21], [22], [23]. In this work we combine transient spectroscopy for the NIR/MIR with the advantages of optical fibres.

Already in the late 19th century people tried to transmit light signals through different media, but again the invention of the laser triggered a vast amount of research and applications for optical, waveguiding fibres. In 1965 the first optical data transmission system was demonstrated by Manfred Börner and a patent was given for it in the following year [24]. Conventional optical fibres are based on the effect of total internal reflection between a medium with higher refractive and a medium with lower refractive index. In the classical form an optical fibres is built with two regions: the core with the higher refractive index surrounded by the concentric cladding with lower refractive index [25]. Typically both are made of fused silica, and dopants are added

for changing the core refractive index [26]. Due to the geometry and size of optical fibres, light can be confined to a small diameter over long distances. As nonlinear optical effects depend on the light intensity and interaction length, optical fibres allow to drastically increase the combination of these two compared to classical bulk optical elements [27].

With silica being the material of choice due to many advantages in the fabrication process and the high transmission for telecommunications applications, the spectral range for these fibres is limited to the optical properties of fused silica, especially limiting the transmission of MIR photons. Many other types of glasses have shown to have interesting properties, like strongly extended transmission windows [28] or enhanced nonlinear coefficients [29]. The downside for many materials is their thermal and chemical stability. One of the materials combining good properties for the transmission, nonlinear coefficients with chemical stability is the compound glass ZBLAN ($55ZrF_4$, $18BaF_2$, $6LaF_3$, $4AlF_3$, $17Na_F$), making it a unique platform for fibre fabrication [30]. Recent research took advantage of the properties of ZBLAN fibres and many groups have explored the possibility to generate supercontinua (SC) [31] which extend to 6 µm [32]. In the last years research focused on high power SC generation, increasing the average MIR power [33], [34], [35].

While silica fibres have been used for visible spectroscopy as SC sources [36] as well as bulk material materials like sapphire plates, ZBLAN has been used for IR microscopy [37]. In this work we have explored the possibilities to generate a NIR/MIR SC in a ZBLAN fibre to utilise it for ultrafast transient absorption spectroscopy.

In this thesis we also have studied the interaction of light in a hybrid fibre consisting of a hollow core silica capillary with an organic semiconducting single crystal in its core. In 2000 the nobel prize in chemistry was awarded for *the discovery and development of conductive polymers* [38]. This shows the importance of organic semiconductors and by today many applications are using organic semiconductors like organic light-emitting diodes (OLEDs) [39], organic solar cells [40] or organic field-effect transistors (OFET) [41]. In contrast to inorganic semiconductors, where electronic properties are defined by the elements electron configuration, organic materials offer a huge amount of

different structures. With electronic properties depending on the molecular structure, one can change these properties by changing the molecule. This offers the chance to engineer properties directly in the direction of desired applications.

Many π-conjugated materials show high nonlinear coefficients [42], making them interesting materials for photonics. We have used standard crystal growing techniques that have been applied to grow fibre crystals, to grow organic crystals inside a fibre capillary. Although filled fibres have been studied before [43], [44] and recent research concentrates on nonlinear effects of fibres filled with liquids [45], [46], investigating fibres with a organic, semiconducting single crystal offers new, interesting phenomena. For example we have observed photoluminescence stimulated by a two-photon absorption inside the filled core.

This thesis will begin to give an overview about the background and relevant theory, necessary for the understanding of the work, in chapter 2. The first topic covered is optical fibres. For this some optical properties of glasses are explained with extra details about heavy metal fluoride and ZBLAN glass. The waveguiding mechanism for optical fibres is explained and different phenomena for supercontinuum generation are presented. The final section explains the filling of a hollow core fibre with liquid, which is needed the crystal growth inside the fibre capillary. Standard techniques for crystal growth from a melt are presented. The second topic covers organic photonic materials. Electronic and optical properties are explained together with the origin of the semiconducting character. Quasiparticles determining charge-carrier dynamics are introduced and finally basic nonlinear properties are explained.

Chapter 3 gives an overview of the experimental techniques used. For this different optical analysis techniques and devices are shown. Furthermore materials and sample preparation methods are also covered.

Chapter 4 deals with the planning, realisation and optimisation of an ultra-fast spectroscopy setup. First the classical design is shown, before upgrading the setup with the ZBLAN fibre. The SC generation is explored and characterised and the whole setup with the ZBLAN SC as a probe is demonstrated by measurements of a conjugated polymer blend.

Chapter 5 and 6 both deal with hollow core fibres filled with single crystal organic semiconductors. While in chapter 5 the experimental development of the crystal growth together with structural analysis and quality evaluation are in the foreground, chapter 6 concentrates on optical properties of these fibres and their analysis.

2 Background

In this chapter an overview is given about background information and theory for relevant topics. In section 2.1 basic principles of crystal growth from melt are discussed. Section 2.2 and 2.3 some considerations about glasses are introduced followed by an explanation of wave guiding in optical fibres and some consequences from these effects and the filling of hollow core fibres in 2.4. The last big section 2.5 covers organic photonic materials.

2.1 Crystal growth from melt

In an ideal crystal all atoms are exactly arranged by the crystal lattice. In real crystals deviations from this can never be completely avoided. The ideal crystal structure leads to important properties, one to mention here is the possibility to transmit electromagnetic waves without scattering. Single crystals are almost perfect structures and can be grown with several different techniques. However, problems like crystal defects or impurities have to be minimised in order to optimise intrinsic material properties. The growth of crystals is a complex field still not completely understood. Crystals can be grown from a supersaturated solution - by slow cooling, evaporation or with a temperature gradient. Growth from vapour with a temperature gradient is possible with or without chemical transport as well as growth in the solid state. We will concentrate here on methods for the growth from the melt.

Growth from the melt is the most popular method to grow large single crystals while maintaining a fast growth rate. The main idea behind these methods is to melt a polycrystalline material followed by a cooling process below the freezing point in order to crystallise it. Typically a polycrystalline

material is obtained. Special methods have to be applied to transform this into the growth of a single crystal. This method requires the material to melt without decomposition, have low chemical reactivity at the melting point, and it must not have a polymorphic transition. A problem can arise from a high vapour pressure at the melting point. Depending on the material to be grown and its melting point different techniques can be chosen like the Bridgeman-Stockbarger [47], [48], Czochralski [49] or zone melting method to mention just some important ones [50].

In the Bridgman or Stockbarger method the molten material is contained in a crucible and then progressively frozen from one end. To achieve this progressive freezing either a furnace with a temperature gradient can be stationary and the crucible is moved along the temperature gradient or the crucible is stationary while the furnace is moved. A third method is to keep both of them stationary and cool the furnace. In order to achieve the growth of a single crystal instead of a polycrystalline material a seed crystal is used to start the growth. This can be achieved either by specific shapes of the crucible or by inserting an external seed crystal, that is partially molten while in contact with the melt.
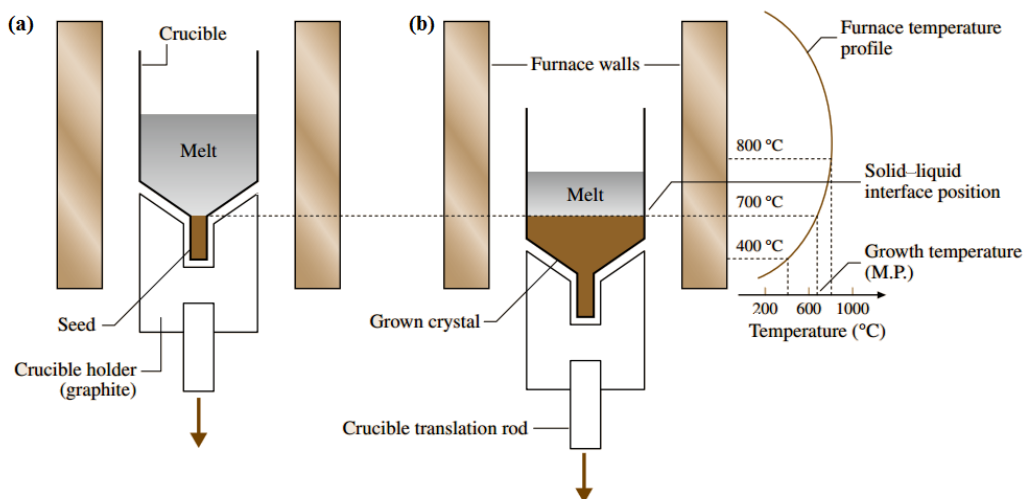
Figure 2.1.1: *Scheme of a Bridgeman growth setup using a single zone furnace at the beginning of the growth (a) and with the partially grown crystal (b). On the right side an exemplary temperature profile is added [51].*

In figure 2.1.1 a schematic of a typical Bridgeman growth process is shown. In this example an open one zone furnace is used with the respective temperature profile on the right side. In figure 2.1.1 (a) the growth process is shown at the beginning, the seed crystal is at the bottom of the crucible, with the melt above it. By a downwards translation of the crucible, the melt progressively moves into a colder temperature zone. When the temperature falls below the melting temperature, it starts to crystallise and the solid-liquid interface moves through the material according to the temperature profile (figure 2.1.1 (b)).

As mentioned above, the growth from the melt offers the possibility to grow large crystals at fast growing rates (rates of 1 mm/min are used in industrial processes [51]) and the setup needed to realise such a growth can be quite simple. On the other hand there are also intrinsic disadvantages, many of them arising from the material being in direct contact with the crucible. The contact of the solid-liquid interface with the crucible can be the cause for the crucible to act as a nucleation site. Special care has to be taken to avoid irregularities on the surface of the crucible. A convex shape of the solid-liquid interface is desirable, as spontaneous nucleations grow out of the crystal rather than growing into the crystal [50].

Another problem that arises from the contact with the crucible is stress induced into the crystal while both the crucible and the crystal are cooling. For this two different conditions have to be considered: a vertical and a horizontal system. In the vertical system the crystal is surrounded completely by the crucible and for that reason the crystals grows with a higher stress induced. The advantage on the other hand is the symmetric shape of the crystal. In a horizontal system the top side of the crystal is not in contact with the crucible and for that reason the crystal has space to expand. The shape typically is a more irregular D-shape. With many different techniques to chose from, it is important to match the technique to the properties of the material to be grown and to the desired crystal properties, like size and dimensions. Further finishing can be optimised by polishing or sand-blasting or even by coating the crucible with a different material.

In order to avoid problems due to the contact of the solid-liquid interface with the crucible other methods have been developed. One of these methods

is the Czochralski process [49]. In this method a crystal is therefore pulled up or down from the melt, that is kept at a constant temperature. For this work we concentrate only on the Bridgeman technique and a modified version of it.

A better way to control the temperature profile inside the furnace with respect to the architecture shown in figure 2.1.1 on the right side is to use a two-zone furnace. This gives a much better defined and controllable temperature profile. The loaded crucible can be set in the beginning in the top-zone well above the melting temperature, while the second zone is set to be below the freezing point with the seed being in this zone. In order to increase the temperature gradient , a baffle can be used to separate the two zones permitting a much steeper temperature gradient.

Choosing the right parameters for an optimal crystal growth is not trivial. Often they can be only found empirically and might need a long time to be explored. The high demands for the crucible have been already discussed, but further one of the most critical parameters to choose is the setting of the temperature gradient and the growth rate. Typically a too high temperature gradient in the furnace will lead to an increase in the dislocation density, as the faster crystallisation gives less time for atoms or molecules to arrange in a perfect crystal structure. Further a too high temperature gradient can cause inhomogeneities. The temperature in a furnace is controlled by a feedback loop and a higher gradient is more likely to lead to the formation of thermal oscillations and for that reason to variations in the growth rate. On the other hand if the gradient is chosen too small also increased inhomogeneity will occur. This is explained by a more likely constitutional supercooling [52]. If the temperature gradient in the melt itself exceeds the temperature gradient of the furnace and for that reason the one driving the crystallisation, for example by convection or heat transfer, supercooled material can exist in front of the solid-liquid interface. This will lead to polycrystallinity that can even result in the formation of cracks due to induced stress. The effect of supercooling increases with a higher growth rate. A method to decrease the effect is by introducing stirring of the melt. Convection inside the melt leads to a natural stirring effect, but also external stirring might be applied.

For volatile materials evaporation during the heating can cause problems and has to be kept small in order to grow good quality crystals. One method for small vapour pressure materials is to use an inert gas at a high pressure on top of the melt. In figure 2.1.2 (a) this is illustrated by a bell cover above the crucible with the melt that seals of the crucible before pressurised gas can flow into the chamber. Further a suitable skin can be created on top of the melt to reduce evaporation. The melt can be also completely encapsulated into a solid without contact to the gas phase (figure 2.1.2 (b)) by a small, distinct melting zone with the charge material sealing the top of the melting zone .
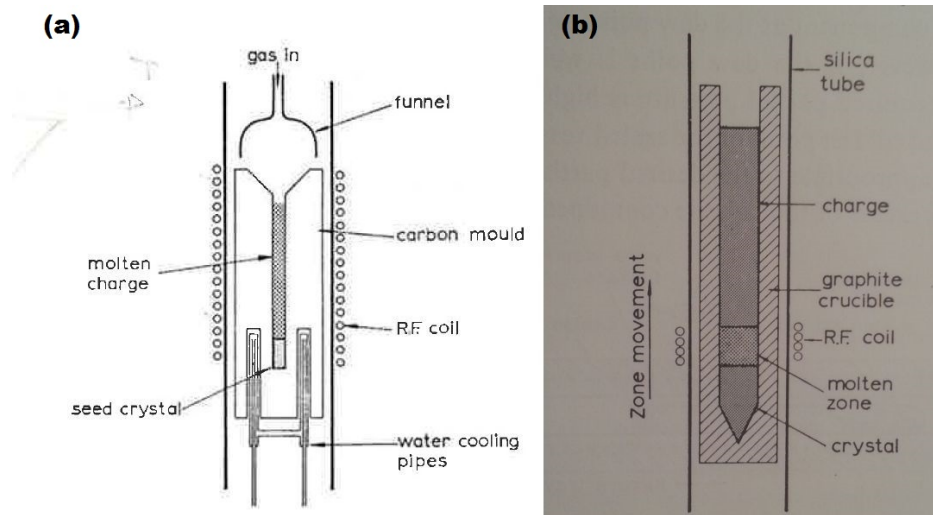
Figure 2.1.2: *(a): A mold for casting germanium crystals. The funnel can be lowered in order to apply gas pressure to the molten germanium. (b) Example of a setup for encapsulating the melt [50].*

Organic crystals

The growth of crystals is a commonly used technique for inorganic materials, like in the semiconductor industry. But in the same way are organic single crystals interesting and in the need for a low density of structural defects. In general similar growing methods can be applied to organic materials, but care has to be taken about characteristics of organic materials. Many organic materials show melt degradation and applying higher temperatures can be very

critical. For that reason crystal growth from solution is the most commonly used technique for organic single crystals. However, often growth rates are as low as 0.1-1 mm per day not. Another problem occurring is the creation of impurities by inclusion of solvent into the crystal lattice. The highest quality crystals are obtained by vapour growth, like simple growth by sublimation or by sublimation along a temperature gradient with a carrier gas [53]. Often very thin, crystallographic perfect platelets are obtained, with a surface reaching cm^2 [54]. The growth from the melt offers also here to grow the largest crystals with high rates of growth. Most commonly used is the Bridgman technique, with the downside being the higher amount of defects as the crystal growths inside a crucible. For organic crystals the stress induced during the cooling process is especially critical as organic crystals are softer.

2.2 Glasses

Glasses have a long history of applications, many of them based on the optical properties. Most important is the transmittance of visible light through silica glass, enabling the use as windows. But also for optics it is an important material due to reflection and refraction, opening possibilities for many applications like mirrors, lenses or more complex waveguiding effects. By adding metallic salts coloured glasses with tuned optical properties can be created. Often glass is referred to silica glass, but many other glasses based on different compositions have been fabricated and explored with interesting properties.

Glass is an amorphous solid material without an ordered crystal structure. Usually they are produced by fast quenching of the molten material and in this way generating a " frozen liquid ". As the liquid gets supercooled, the atoms have not enough time to be arranged in a crystal structure, and present a structure similar to the liquid phase. Glasses are not in a thermodynamically stable state of a crystal, and for that reason are defined metastable. As it has no crystal structure, glass shows long-range disorder, while there is still a short-range order. The order to the nearest neighbours is determined by the

chemical bonds of the glass atoms or molecules and can for that reason change with the particular material used.

The transmission of light through glass is possible because of its amorphous structure. Polycrystalline materials on the other hand hold a large amount of different facets and grain boundaries, each acting as possible scattering centres, strongly decreasing the transmission of light. Not only the optical properties make glass such an important material, but also its mechanical, electrical and chemical properties are important for many applications [55], [56].

2.2.1 Transmittance of glass

Scattering

Some part of light shone on a piece of glass can be scattered. If the incident light has a frequency ω_0 and the scattered light has the same frequency ω_0 we call this elastic scattering or Rayleigh scattering. Scattered light can be also shifted in its frequency $\omega_s = \omega_0 + \omega_R$, caused in an energy transfer between the photon and the glass. This inelastic scattering is due to the interaction of photons with the phonons caused by vibrations of molecules and atoms of the material. For Raman scattering the interaction is with optical phonons, while interaction with acoustic phonons is called Brillouin scattering [57].

Compared to the intensity of the incident light, the intensity of scattered light decreases by several orders of magnitude from Rayleigh scattering to
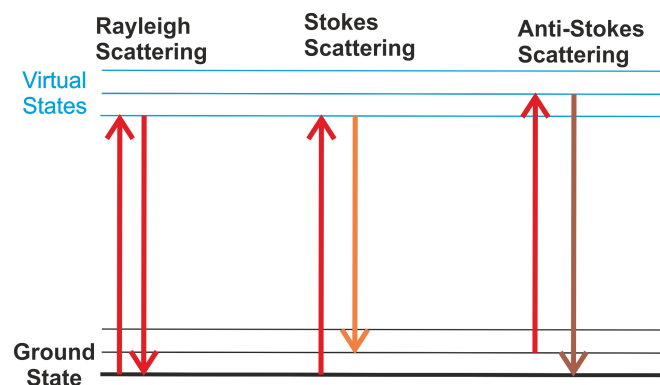

Figure 2.2.1: *Schematic of the energy levels for Rayleigh and Raman scattering*

Raman scattering to Brillouin scattering, respectively. Both momentum and energy have to be conserved during the scattering process:

$$\Delta k = k_1 - k_2; \quad \Delta \hbar \omega = \hbar \omega_1 - \hbar \omega_2 \tag{2.1}$$

with k being the wavevector, ω the angular frequency, $\hbar$ the Planck constant and 1 and 2 representing the incident and scattered light. For Rayleigh scattering there is no energy transfer $\Delta k = 0$. For the inelastic scattering we can differentiate two different processes, for $k_1 > k_2$ energy is transferred from the photon to a vibrational mode (Stokes) and for $k_1 < k_2$ the energy is transferred from a vibrational mode to a photon with the photon gaining energy (anti Stokes). The energy levels for both Rayleigh and Raman scattering are visualised in figure 2.2.1.

Rayleigh scattering is caused by fluctuations in the polarisability of a transparent material or gas. Typically these origin in fluctuations in the density. Atoms or molecules that are small in comparison to the wavelength λ of the photons act as scattering centres. The light scattering coefficient α_s due to thermal diffusions caused by density fluctuations can be expressed as [58]

$$\alpha_s = \frac{8\pi^3}{3} \frac{k_B T_F}{\lambda^4} \frac{n^8 p_{12}^2}{\rho v_1} \tag{2.2}$$

with k_B the Boltzman constant, T_F the fictive temperature at which the density fluctuations of the liquid glass are frozen, n the refractive index of the scattering centre, p_{12} the longitudinal elasto-optic constant and v_1 the longitudinal sound velocity. From equation 2.2 we see that the scattering is proportional to λ^{-4} and therefore has a strong dependence on the wavelength of the incident light. The scattering effect is much stronger for light with shorter wavelengths.

These *intrinsic* scattering effects, due to the structure of the glass itself, are the ultimate limiting factor to the transmission of a given type of glass. This is important when it comes down to ultra-low loss applications like optical fibres or laser glasses. On the other hand *extrinsic* scattering effects can be controlled

by the production process. These scattering centres can be for example bubbles, inclusions or impurities in the glass.

Absorption

Besides of scattering effects limiting the transmission of light through the whole spectrum of incident light, the possible transmission window of a glass is restricted by its absorption. The transmission window is restricted by absorption effects on the short and long wavelength side, that have to be considered separately because of their different origin.

The absorption of photons with higher energy arises from the electronic transition between atoms or ions. For SiO_2-glass the energy levels are determined the sp^3-hybrid orbitals of the silicon atom and the three p-orbitals of the oxygen atoms. Together they form molecular orbitals with new energy levels as illustrated in figure 2.2.2 (a), leading to strong and weak binding orbitals (SB, WB), a lone pair state (LP) and anti-binding states (SA, WA) as can be seen in figure 2.2.2 (a) and (b). In this configuration the conduction band is formed by the anti-binding states SA and WA, while the valence band consists

Figure 2.2.2: *(a): Electronic transition of a SiO_2-molecule. The sp^3-hybrid orbitals from the silicon atom and p-orbitals of the oxygen atoms form weak and strong binding (WB, SB) , anti-binding (SA, WA) and a lone pair state (LP). (b): Diagram of the energy levels of SiO_2. [57]*

of the WB, SB and LP states. The electronic transition can take place between valence and conducting band, and a simplified scheme as seen in figure 2.2.2 (b) consists of two energy levels with a band gap of 10.5 eV for non-bridging oxygen and 11.7 ev for bridging oxygen.

This leads to a resonant absorption in the UV around 106-118 nm. The purity of the glass is very important for the transmission close to the UV-edge, as impurities can easily introduce intra-gap energy states in between the valence and conduction band and lower the photon energy needed to be absorbed. The UV-absorption edge can be described by the absorption coefficient α_{UV} with an exponential dependence known as Urbach's rule [59]:

$$\alpha_{UV}(\omega) = \alpha_0 exp \left\{ \frac{-\sigma \left[E_g(T) - \hbar\omega \right]}{k_B T} \right\} \tag{2.3}$$

α_0, σ and the energy dependent gap E_g are fitting parameters independent of ω.

The ultraviolet cutoff frequency λ_0 is defined by the wavelength that has an absorption coefficient $\alpha = 50 cm^{-1}$ [57]. This cutoff frequency for inorganic glasses mainly depend on the atomic number of the anions and cations in the structure. While for the anion an increasing atomic number leads to an increase of the cutoff frequency, for cations the cationic field strength Z/a^2 is the important parameter, with Z the atomic number and a the ionic radius [57].

The infrared absorption of glass is far below the energy gap for an electronic transition. The absorption in this region is due to a coupling of the electromagnetic field of the photons to vibrational modes of the glass. These can be multi-phonon processes as well as fundamental vibrational bands. The IR absorption edge can be also described with an exponential dependence [60] similar to equation 2.3:

$$\alpha_{IR}(\omega) = \alpha_0 \left[N(\omega_0) + 1 \right]^{\omega/\omega_0} \left[N(\omega) + 1 \right]^{-1} exp(-C\omega) \tag{2.4}$$

with $N(\omega) = \left[\exp\left(\frac{\hbar\omega}{k_B T} \right) - 1 \right]^{-1}$, ω_0 an average optical phonon frequency and C a material constant characterising the vibrational anharmonicity. Usually the highest frequency of the IR-absorption can be associated to the network

former, for silica glass the SiO_4 tetrahedon. An empiric formula describing the frequency is the Szigeti equation [61]:

$$\omega = \frac{\sqrt{F/\mu}}{2\pi c} \tag{2.5}$$

with the force constant F, and the reduced mass of the component ions $\mu = \frac{m_1 m_2}{m_1 + m_2}$. The force constant reflects the bonding strength and changes with different types of bonds. This gives possibilities to design properties of a glass by the wanted IR-absorption for specific applications.

To summarise all the intrinsic losses of scattering and absorption, the total intrinsic attenuation coefficient α_t as a function of wavelength is given by equation 2.6 with the first term relating to the multi-phonon absorption, the middle term to the Rayleigh scattering and the last term the UV absorption with A, a, B, C and c being parameters according to the respective physical process [62].

$$\alpha_t = A \exp\left(-\frac{a}{\lambda}\right) + B\lambda^{-4} + C \exp\left(\frac{c}{\lambda}\right) \tag{2.6}$$

In equation 2.6 Raman scattering is not considered because of its much lower scattering cross-section in comparison to Rayleigh scattering as mentioned above.

2.2.2 ZBLAN glass

We have discussed general properties of silica glass so far, with SiO_2 glass being the generic example of a glass and the most commonly used one. Silica glass has very good properties for applications with visible light, with the lower transmission limit in the ultraviolet (UV) and the upper in the near infrared, but lacks transmission for increasing wavelengths above $\approx 2.5\,\mu m$. For applications at longer wavelengths in the mid infrared (MIR) regime different materials have to be used.

Figure 2.2.3 shows the calculated transmission curves for oxide, halide and chalcogenide glasses. The oxide glasses, like silica, show good transmission for shorter wavelength, but the transmission loss has a minimum at below
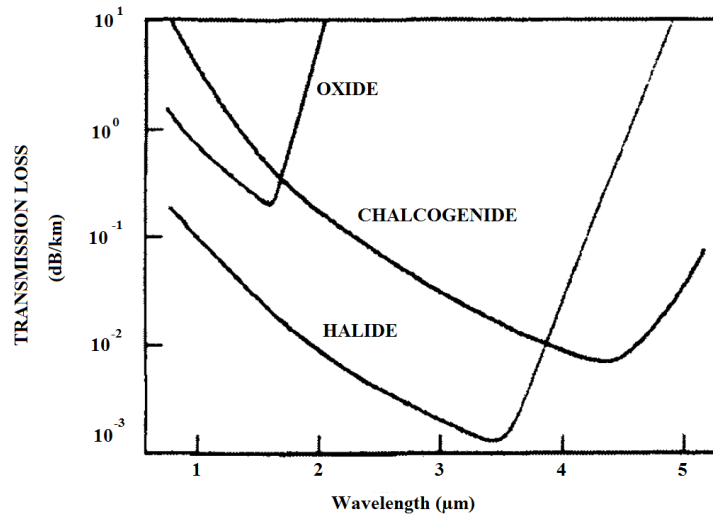
Figure 2.2.3: *Theoretical transmission losses for three general types of glasses [63]*

2 μm and strongly increases for increasing wavelengths. Chalcogenide glasses contain at least one chalcogenide element, sulphur, selenium or tellurium. They exhibit the minimum loss at the longest wavelength and make good candidates for longer wavelength applications, but show a higher overall loss. Halides are compound of a halogen and a second less electronegative element. Their glasses show the lowest overall losses in figure 2.2.3 and show a significantly increased IR transmission in comparison to silica glass. They also have have a shorter IR-cutoff wavelength than chalcogenide glasses. Besides of the optical properties the glass forming properties and the mechanical and chemical stability will determine which glasses can be used for applications.

Some very promising halide glasses are in the class of heavy metal fluoride (HMF) glasses. These special glasses have to overcome several problems compared to silica glass. As fluorine is the most electro-negative element, it has a high preference to form ionic bonds and with that crystals. In order to form a glass the crystallisation has to be avoided. The metal-fluorine bond is weaker than the metal-oxygen or metal-hydroxide bond, making the glass sensitive to corrosion by water. A consequence of this weaker bond is also a lower transition temperature of the glass, giving them a sensitivity to thermal shocks and a low mechanical and chemical strength [62].

In the group of the MHF-glasses the glasses based on ZrF_4 have shown promising results. ZrF_4 itself does not form a stable glass, but by adding a modifier like BaF_2 a glass can be formed. Many different compositions have been investigated. Adding LaF_3 strongly improves the stability, a small amount of AlF_3 decreases the rate of crystallisation of the ZBLA-glass ($55ZrF_4$, $35BaF_2$, $6LaF_3$, $4AlF_3$). Introducing NaF into the system, Ba^{2+} and Na^+ would compete for forming a crystal lattice and create an inter-diffusion barrier. Multi-components make a crystal unit cell more complex and the crystal lattice less favourable. A mismatch in size of different the atom radii is further helping to avoid crystallisation [64]. The glass formed by these compounds is called ZBLAN ($55ZrF_4$, $18BaF_2$, $6LaF_3$, $4AlF_3$, $17Na_F$). As ZBLAN is a composition of different compounds exact properties can vary according to the production process.

We have seen before that the losses in glass on the long wavelength side are dominated by multi-phonon absorption. Equation 2.4 and 2.5 are describing this IR absorption. We can see that the absorption is dependent on the force constant F and the inverse reduced mass μ. In order to shift the IR absorption edge to longer wavelength a weaker bonding and higher atom masses are preferable.

Figure 2.2.4 illustrates the transmission window and shift of the IR absorption edge for silica glass and different HMF-glasses. Curve 2 shows ZBLA which has a similar transmission spectrum to ZBLAN. While silica shows already a decrease to only 50 % transmission for 3 μm, ZBLA can extend the transmission to over 6.5 μm.

Calculations suggest a lower Rayleigh scattering for the ZBLAN glass compared to silica glass, as it was indicated in figure 2.2.3. By now the main mechanism for scattering loss was not the intrinsic glass properties itself, but the imperfection in the production of the glass. This extrinsic scattering is strongly originated in the formation of isolated crystals or bubbles in the glass.

One of the most important applications for low-loss glasses in the extended IR-region are optical fibres with ultra-low losses. In section 4.3 ZBLAN fibres are used for supercontinuum generation with respect to extended NIR/MIR
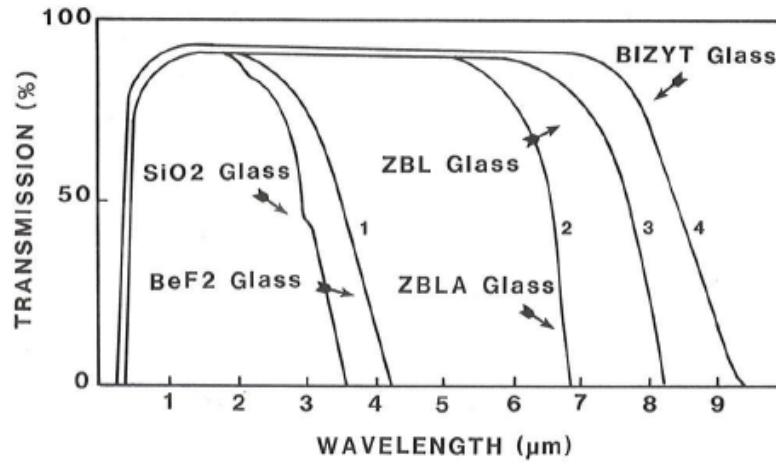
Figure 2.2.4: *Infrared absorption edge from different glasses. The curve 2 shows a similar absorption to ZBLAN [62].*

wavelengths. In section 4.4 it is shown how this can be used for ultrafast spectroscopic applications.

2.3 Optical fibres

Optical fibres are dielectric waveguides of cylindrical shape. They are built of two concentric regions, the core in the middle, surrounded by the cladding. The guiding of light inside an optical fibre is based on the effect of total internal reflection. For this purpose the refractive index of the core has to be slightly higher than the refractive index of the cladding $n_{core} > n_{cladding}$.

In the simple case of a step-index fibre the core is just surrounded by the layer of the cladding as seen in figure 2.3.1, while for graded-index fibres the refractive index gradually decreases with distance from the centre. In this work only step-index fibres are used. Fibres used for telecommunications are typically made out of silica glass, with the core being doped in contrast to the pure cladding. This creates the difference in refractive index with n_{core} being 1.4475 and $n_{cladding}$ being 1.444 at 1500 nm [65].
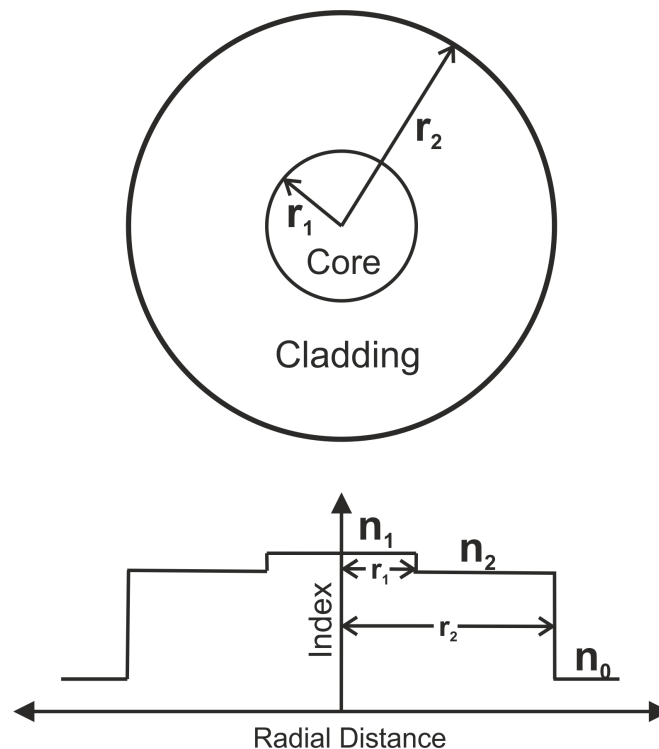

Figure 2.3.1: *Illustration of a step-index fibre with refractive index profile*

Total internal reflection and numerical aperture

If we consider the interface of two dielectric media with the refractive indices $n_1 > n_2$, an incident ray of light will be refracted at the interface of the two media as it is illustrated in figure 2.3.2. This refraction is described by Snell's law:

$$\frac{\sin \Phi_1}{\sin \Phi_2} = \frac{n_2}{n_1} \tag{2.7}$$

For the given refractive indices, Φ_1 is always smaller than Φ_2. For an angle of refraction Φ_2 of 90° the exiting ray travels parallel to the interface of both dielectrics, while Φ_1 is still smaller than 90°. For this case we can define a critical angle of incidence Φ_c and for equation 2.7 follows

$$\sin \Phi_c = \frac{n_2}{n_1} \tag{2.8}$$

For angles greater than Φ_c all the incident light will be reflected back into first medium and we observe the effect of total internal reflection (TIR).
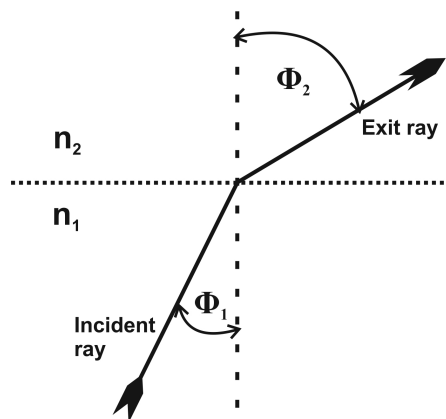
Figure 2.3.2: *Refraction of a ray of light on the interface of two dielectric media with higher and lower refractive index*

Using the TIR at the interface between the core and the cladding of an optical fibre allows light to propagate through the fibre. As we have seen only for angles greater than the critical angle, TIR can occur. For a fibre this means that not every ray of light will be guided through the core. Only for an
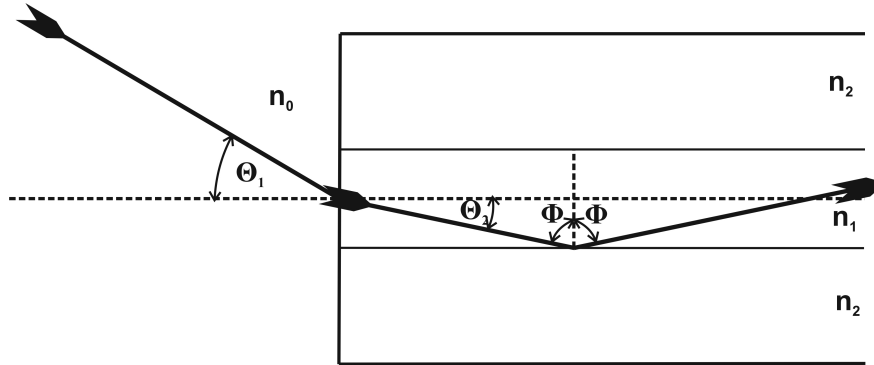
Figure 2.3.3: *A ray of light launched from air into a fibre with refractive index n_1 and n_2*

angle between the ray of light and the optical axis of the fibre smaller than the acceptance angle Θ_a, TIR at the core-cladding interface is possible and light will be guided through the core. According to this angle we can define the cone of acceptance for which light is guided in the core. For bigger angles of incidence light is refracted into the cladding. According to the acceptance angle we can define the cone of acceptance.

In figure 2.3.3 we see a schematic of a ray of light launched from air (n_0) into a fibre with the angle of incidence Φ_1 smaller than the accepting angle. If we consider the interface between the air and the core for equation 2.7 follows

$$n_0 \sin \Theta_1 = n_1 \sin \Theta_2 \qquad (2.9)$$

Using trigonometrical relationships this can be written as

$$n_0 \sin \Theta_1 = n_1 \sqrt{1 - \sin^2 \Phi} \qquad (2.10)$$

Considering the limiting case for total internal reflection we use Φ_c instead of Φ, given by equation 2.8 and Θ_a for Θ_1. The limit gives us the definition of the numerical aperture (NA), an important value of a fibre as it connects just the material properties of the refractive index both for the core and the cladding with the accepting angle of an incoming ray of light.

$$NA = n_0 \sin \Theta_a = \sqrt{n_1^2 - n_2^2} \qquad (2.11)$$

So far we have considered rays of light travelling through a fibre and used geometrical optics, which is a good approximation in the case of large core diameters. For core sizes that are comparable to the wavelength of light electromagnetic mode theory has to be applied [66].

2.3.1 Fibre modes

In order to describe the complete propagation of an electromagnetic wave through a waveguide the Maxwell equations have to be applied and solved. In this place only some important results are shown instead of a complete mathematical description, that can be found in text books [66].

We consider now a planar wave travelling along the ray path through the fibre that was discussed before. The basic solution ψ of the wave equation can be written as

$$\Psi = \Psi_0 \exp\left[i\left(\omega t - \vec{k}\cdot\vec{r}\right)\right] \tag{2.12}$$

where Ψ_0 is the amplitude, ω the angular frequency, t the time, $\vec{k}$ the propagation vector and $\vec{r}$ the coordinate where the field is observed. A *mode* is a stable field distribution perpendicular to the propagation direction, that changes only periodically with its phase along the propagation axis. A mode propagating along the fibre axis z can be described by

$$\exp\left[i\left(\omega t - \beta z\right)\right]$$

with β being the propagation constant. The propagation constant for a particular mode is the component of the wavevector $\vec{k}$ parallel to the optical axis of the fibre.

Depending on either the magnetic or electric field dominating in the transverse plane, the corresponding modes are called transverse electrical (TE) and transverse magnetical (TM) modes. As the distribution is in two dimensions, two integers l, m describe the order of the mode, and overall they can be written as TE_{lm} or TM_{lm} modes.

The propagation constant β is a useful parameter to describe the propagation of modes as it is conserved at the core-cladding interface. Depending on the value of β a mode can be guided. The allowed values of β are limited by the refractive index of the core and cladding.

$$n_2 k_0 < \beta < n_1 k_0$$

In this case we can have a guided mode, with only the evanescent field penetrating into the cladding. Else radiation modes can be observed with an energy flow from the core to the cladding, which means the mode is not guided.

As we have seen from the propagation constant, not all modes are guided inside a fibre. It is useful to define the normalised frequency or V number in order to quantise the guided modes.

$$V = k r_1 \sqrt{n_1^2 - n_2^2} = \frac{2\pi}{\lambda} r_1 \left(NA\right) \tag{2.13}$$

V is a dimensionless parameter and combines three important parameters of a fibre, the core radius r_1, the difference in the refractive indices $\Delta n = n_1 - n_2$ and the operating wavelength λ. For $V < V_c$, with $V_c \approx 2.405$ the cutoff frequency, only the fundamental mode is guided through a fibre. There is no cutoff for the fundamental mode. In this region a fibre is called single mode, while for larger values of V a fibre is called multimode, as it supports more than one guided mode. The number of guided modes per orthogonal polarisation or the mode volume M_s can be estimated by [67]

$$M_s \approx \frac{V^2}{2} \tag{2.14}$$

As V is a function of λ the number of guided modes is depending on the wavelength of the incident light. For a given fibre a cutoff wavelength λ_c can be defined.

$$\lambda_c \approx \frac{2\pi \cdot r_1}{2.405} NA \tag{2.15}$$

By selecting the wavelength of the light coupled into the fibre it can be a multimode fibre for $\lambda < \lambda_c$ or single mode for wavelengths longer than λ_c. Besides of wavelength, the easiest parameter to change the number of modes is the core radius, as a smaller core supports a lower number of modes.

2.3.2 Chromatic dispersion in fibres

Dispersion describes the change of phase velocity depending on its frequency. The refractive index n of a mode travelling through a fibre is a function of ω. As the speed of light inside the fibre is given by $v = \frac{c}{n(\omega)}$ components of the light with different frequencies will travel with different speeds. Considering an optical pulse with a finite spectral bandwidth travelling through the fibre the pulse will be spreading with the travelled distance as components propagate at different speed.

To describe the fibre dispersion the propagation constant β is expanded in a Taylor series around the central pulse frequency ω_0.

$$\beta(\omega) = n(\omega)\frac{\omega}{c} = \beta_0 + \beta_1(\omega - \omega_0) + \frac{1}{2}\beta_2(\omega - \omega_0)^2 + \dots \qquad (2.16)$$

with $\beta_m = \left(\frac{d^m\beta}{d\omega^m}\right)_{\omega=\omega_0}$, $\quad (m = 0, 1, 2, \dots)$

Both β_1 and β_2 can be related to the refractive index $n(\omega)$ through the following equations

$$\beta_1 = \frac{1}{v_g} = \frac{n_g}{c} = \frac{1}{c}\left(n + \omega\frac{dn}{d\omega}\right) \qquad (2.17)$$

$$\beta_2 = \frac{1}{c}\left(2\frac{dn}{d\omega} + \omega\frac{d^2n}{d\omega^2}\right) \qquad (2.18)$$

where n_g is the group index and v_g the group velocity. From equation 2.17 we can find the group velocity, which is the speed the envelope of an optical pulse moves with. β_2 describes the dispersion of individual frequencies with the pulse propagation and for that the broadening of an optical pulse. This is known as group velocity dispersion (GVD) with β_2 being the GVD parameter, given in the unit $\frac{ps^2}{m}$. Another dispersion parameter D can be defined that is

often used in experimental work. It is given in units of $\frac{ps}{nm\cdot km}$ and gives the spreading in picoseconds per nanometre of bandwidth per kilometre of travel.

$$D = \frac{d\beta_1}{d\lambda} = -\frac{2\pi c}{\lambda^2}\beta_2 = -\frac{\lambda}{c}\frac{d^2 n}{d\lambda^2} \qquad (2.19)$$

To calculate the dispersion using equations 2.17 - 2.19 the change of the refractive index $n(\lambda)$ with wavelength has to be known. The refractive index of a transparent glass can be approximated using the Sellmeier equation

$$n^2(\lambda) = 1 + \sum_{i=1}^{j} \frac{B_i \lambda^2}{\lambda^2 - C_i} \qquad (2.20)$$

with B_i and C_i being the experimentally determined Sellmeier coefficients. The Sellmeier equation gives a good approximation of the refractive index for wavelengths being far away from the material resonances. Typically it is calculated for $j \leq 3$, but summing over more contributing terms gives a higher accuracy.

Figure 2.3.4 shows the change of β_2 and D with the wavelength for bulk fused silica. Both parameters become zero around $1.27\,\mu$ m. This point is called the zero-dispersion (ZD) wavelength λ_D. When crossing the ZD point to longer wavelengths both parameters change their sign. The region with D being negative is called the *normal dispersion* regime. Lower frequencies travel faster in this regime, introducing a chirp, with lower frequencies at the front of the pulse. For positive values of D it is called the *anomalous dispersion* leading to the opposite chirp of a pulse. Close to the zero dispersion the pulse propagation might require to include also third-order dispersion terms [67].

While figure 2.3.4 is for bulk fused silica, the dispersion of a silica fibre will show slight changes with respect to this figure. First dopants maybe be used in the core. Second, an effective mode index has to be used for guided modes instead of the material refractive index of the core. The wave guiding contribution to β_2 is in general small, but becomes comparable to the material contribution close to the zero dispersion. The wave guiding contribution depends on fibre parameters like the core radius or the difference of the
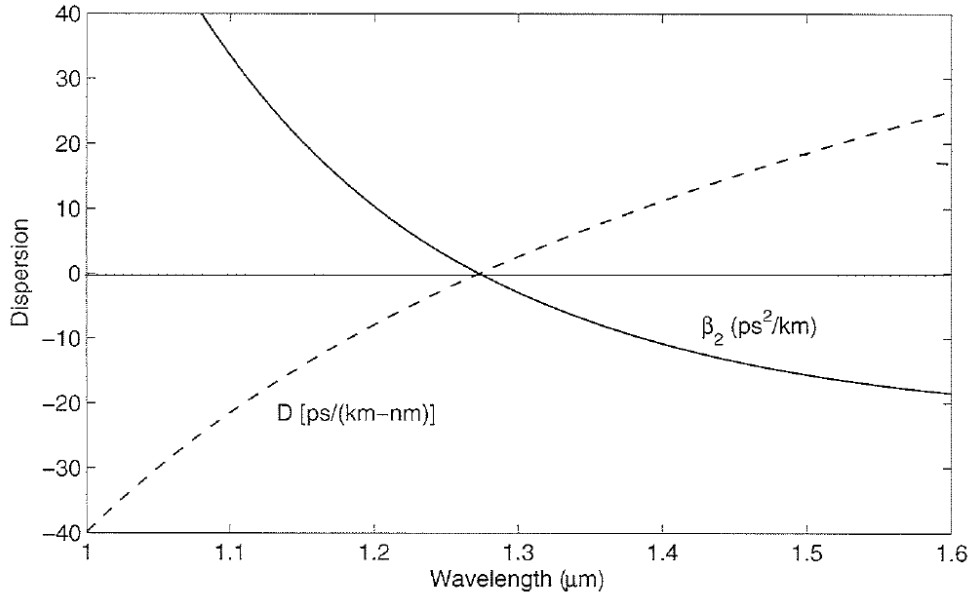
Figure 2.3.4: *Variation of β_2 and D with wavelength for fused silica [67]*

refractive indices. This gives possibilities to influence the dispersion by specific fibre designs, especially the zero dispersion wavelength can be shifted.

In order to understand the influence of waveguiding effects Maxwell's equations have to be considered. Details can be found in many textbooks [68], [69], here we present only briefly the results. Expressing the wave equation in cylindrical coordinates and using the Fourier transformation, it can be seen that Bessel functions solve the differential equation inside the core. This leads to the eigenvalue equation

$$\left[\frac{J'_m(pr_1)}{pJ_m(pr_1)} + \frac{K'_m(qr_1)}{qK_m(qr_1)} \right] \left[\frac{J'_m(pr_1)}{pJ_m(pr_1)} + \frac{n_c^2}{n_1^2} \frac{K'_m(qr_1)}{qK_m(qr_1)} \right] = \left(\frac{m\beta k_0 \left(n_1^2 - n_c^2 \right)}{r_1 n_1 p^2 q^2} \right)^2 \tag{2.21}$$

with $J_m(x)$ the Bessel function, $K_m(x)$ the modified Bessel function, m is an integer, $P = \sqrt{n_1^2 k_0^2 - \beta^2}$ and $q = \sqrt{\beta^2 - n_c^2 k_0^2}$.

It is helpful to define the dispersion length L_D, which gives the length scale for which dispersion effects become important:

$$L_D = \frac{T_0^2}{|\beta_2|} \tag{2.22}$$

where T_0 is the input pulse width.

Additional to dispersion due to the material and the wave guiding, modal dispersion can be found in multimode fibres. As light propagates in different modes, an effective refractive index has to be used, that depends on the mode and light travelling in different modes experiences an additional dispersion.

2.3.3 Fibre losses

The attenuation of the light propagating through a fibre is an important property, as it is a limiting factor for many applications of optical fibres. The loss in a fibre is strongly dependent on the wavelength of propagating light. If P_0 is the power coupled into a fibre of the length L, then the power P_t transmitted through the fibre is

$$P_t = P_0 \exp\left(-\alpha L\right) \tag{2.23}$$

with α being the attenuation constant, that contains losses from all different sources. Typically the loss of a fibre is given in the attenuation of the input signal per km (dB/km). Figure 2.3.5 shows the loss spectrum of a typical silica fibre with both experimental values and theoretical calculations for different sources of loss. There are different categories of sources.

In section 2.2 properties of glass have been presented and discussed. Silica glass is transparent from roughly 200 nm up to 2400 nm. The first reason for loss is the absorption of the fibre material itself. Glass is transparent in the visible region of light, but extending the wavelength more into the UV or IR the absorption of silica glass drastically increases. Intrinsic absorption of the material is given by resonances of the material. For silica these are electronic resonances on the UV side, as absorption bands from the silica molecules can be observed for silica glass. At the other end of the transparent region the absorption is given by vibrational resonances in the IR. Extrinsic absorption is generated through impurities in the material. These can be due to dopants
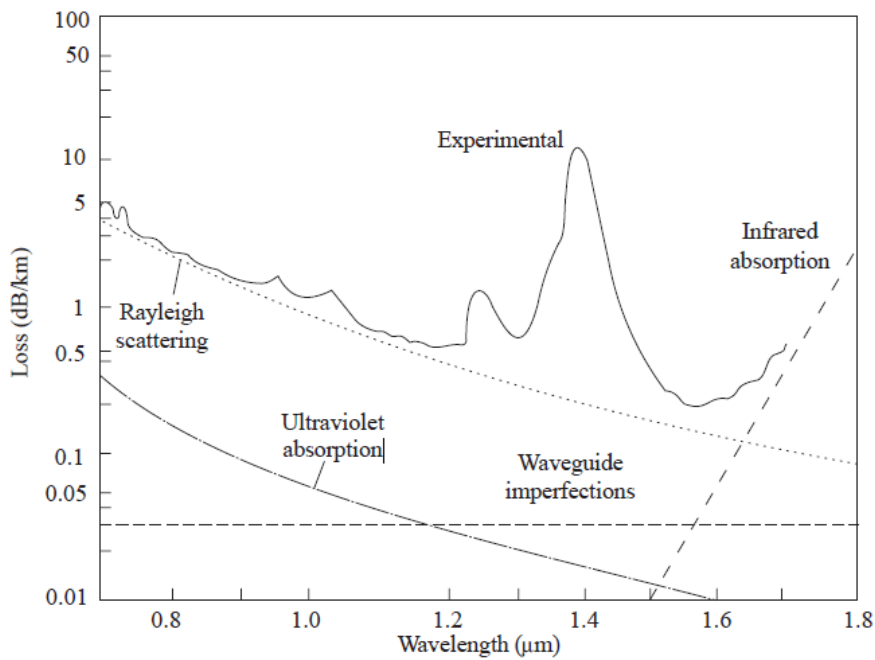
Figure 2.3.5: *Attenuation versus wavelength curve for a low loss fibre [70]*

used for the fibre fabrication, but can also be unwanted impurities from the fabrication process like OH^- ions, that have a strong resonance at 2.73 μ*m* together with several overtones at lower wavelength like the strong peak seen in figure 2.3.5 at around 1.4 μ*m*.

Another mechanism of loss is the Rayleigh scattering. This scattering process is caused by microscopical fluctuations in the density of the material. As silica glass is an amorphous network of SiO_2-bonds without a crystal structure, these fluctuations from the average density occur naturally. The density fluctuations lead to local changes in the refractive index, that can function as scattering centres. In the transmitting region the Rayleigh scattering is the fundamental limit for the loss as it originates in the structure of glass itself, while the absorption limits depend on the composition of the glass and can strongly be influenced by choosing different glasses (dopants). It scales with $\frac{1}{\lambda^4}$ and for that reason the loss due to Rayleigh scattering decreases for longer wavelength.

Other sources of loss for fibres can be bending losses and scattering at the cladding-core interface due to waveguide imperfections or changes in the

refractive index. Bending losses can be explained by the evanescent field travelling through the cladding. With bending of the fibre, the evanescent field on the the outer side has to travel faster to keep up with the field in the core. As the speed of light is limited, energy can be lost by radiation [70].

2.3.4 Supercontinuum generation in fibres

Nonlinearity

The polarisation **P** of a dielectric medium induced by an electric field **E** is given by

$$\mathbf{P} = \epsilon_0 \left(\chi^{(1)} \cdot \mathbf{E} + \chi^{(2)} \cdot \mathbf{E}^2 + \chi^{(3)} \cdot \mathbf{E}^3 + \dots \right) \tag{2.24}$$

ϵ_0 is the vacuum permittivity and $\chi^{(j)}$ is the j-th order susceptibility and a tensor of the rank $j + 1$. The strongest contribution comes from the linear term $\chi^{(1)}$ and leads to refraction and absorption. The nonlinear higher order effects can be neglected for weak fields, but for intense electromagnetic fields also the nonlinear effects have to be considered. The second order susceptibility leads to effects like second-harmonic or sum-frequency generation and only exists for materials without an inversion symmetry in their crystalline structure. The third order susceptibility includes effects like third-harmonic generation, four-wave mixing and nonlinear refraction. Without achieving phase-matching most third-order effects originate in the nonlinear refraction. The total refractive index n_{tot} can be written as

$$n_{tot} = n + n_2 \left| E \right|^2 \tag{2.25}$$

where n is the linear refractive index, n_2 is the nonlinear refractive index and $\left| E \right|^2$ is the light intensity. As n_2 typically has very small values, only for strong intensities the nonlinear term makes a not neglectable contribution to n_{tot}. In this case typically a strong optical pulse induces changes in the refractive index, that leads to many different effects.

A measurement of the efficiency of a nonlinear optical effect can be given by the product $I_0 L_{Eff}$, with I_0 the optical intensity and L_{eff} the effective interaction length. For a given incident optical power P_0 and a focused spot of diameter r the intensity is given by $I_0 = \frac{P_0}{\pi r^2}$ and can be increased by focusing the beam on a smaller area. But at the same time with increasing the focus the length of the focal region decreases, so that the two[1] effects cancel out. In an optical fibre instead the spot size is given by the core radius and can be maintained over the whole fibre length, while the interaction length is only limited by the fibre losses. This means that the nonlinear interaction can be strongly increased inside an optical fibre, allowing nonlinear effects to be observed even in weak nonlinear materials like silica.

Analogue to the definition of the dispersion length we can also define the nonlinear length L_{NL}, which indicates the length for which nonlinear effects become important, as follows:

$$L_{NL} = \frac{1}{\gamma P_0} \tag{2.26}$$

γ is the nonlinear parameter and P_0 is the peak power of the incident pulse. If the length of the fibre L is large in comparison to both the nonlinear and the dispersion length $L \ll L_D, L_{NL}$ both effects play no significant role in the light propagation through the fibre. For a longer fibre length L the ratio of the dispersion and nonlinear length gives a good estimation of which effect is dominating.

$$\frac{L_D}{L_{NL}} = \frac{\gamma P_0 T_0^2}{|\beta_2|} \tag{2.27}$$

For $\frac{L_D}{L_{NL}} \ll 1$ the dispersion-dominant regime is applicable, while for $\frac{L_D}{L_{NL}} \gg 1$ nonlinear effects will dominate. The case of $\frac{L_D}{L_{NL}} \approx 1$ will be discussed below.

Self-phase-modulation

As we have seen above for strong intensities the total refractive index varies with time:

$$\frac{dn_{tot}}{dt} = n_2 \frac{d\,|E|^2}{dt} = n_2 \frac{dI}{dt} \tag{2.28}$$

Considering a pulse propagating through a medium, the phase is given by

$$\Phi(t) = \omega_0 t - kr = \omega_0 t - \frac{2\pi}{\lambda} \cdot n_{tot} L \tag{2.29}$$

The varying refractive index leads to a variation of the Phase over the travel length L. The frequency of the pulse is given by the deviation of the phase:

$$\omega(t) = \frac{d\Phi}{dt} = \omega_0 - \frac{2\pi L}{\lambda} \frac{dn_{tot}}{dt} = \omega_0 - \frac{2\pi L}{\lambda} n_2 \frac{dI}{dt} \tag{2.30}$$

The phase shift or the self-phase modulation (SPM) finally leads to a change of the light frequency in a pulse travelling through a fibre. Additionally in the presence of two pulses, the varying refractive index of one pulse can modulate the phase of a second pulse. This is known as cross-phase modulation (XPM). Neglecting the dispersion effects in a fibre, the SPM introduces a chirp to the pulse propagating through the fibre, while its temporal shape is unaffected. Depending on the sign of $\frac{dI}{dt}$, the chirp generates longer wavelengths at the leading edge of the pulse, and shorter wavelength at the trailing edge.

For a real medium SPM cannot be seen independently from other effects. Especially the combination of SPM and dispersion has to be considered and leads to two different scenarios: The pulse propagating in the normal or anomalous dispersion regime. In the normal dispersion, a consequence of the spectral chirp from the SPM is a temporal chirp due to the dispersion. The longer wavelength components will travel faster, leading to a temporal broadening. In the anomalous regime a completely new situation is created. Due to SPM longer wavelengths are created at the leading edge of the pulse, but because of dispersion effects longer wavelengths travel less fast. This can be used for temporal pulse compression.

Stimulated Raman scattering

Stimulated Raman scattering (SRS) is a fundamentally different process, since an energy transfer occurs to and from the dielectric medium while for effects discussed above, like SPM, the energy is conserved for the light propagating. Light travelling through a dielectric medium can transfer light to the vibrational or rotational modes of the medium. While Rayleigh scattering is an elastic scattering, i.e. the energy of the photon is conserved, Raman scattering is an elastic process with the photon gaining energy from the vibrational modes (anti Stokes scattering) or losing energy to the vibrational modes (Stokes scattering). All processes are illustrated in figure 2.3.6. Usually Raman scattering is a spontaneous effect, but by confining the incident light together with the Raman scattered light in the medium, it can occur as a stimulated process with a much higher efficiency. Optical fibres are a good example for this confinement occurring inside the core of the fibre.

Photons are created with a down shifted frequency, propagating in the same direction as the incident beam, while higher vibrational states are created in the dielectric medium with the energy difference of the incident photon and the down shifted photon $\hbar\Delta\omega$ matching the excitation energy. The incident light acts as a pump while the down shifted light forms the Stokes wave. Through this mechanism energy can be transferred between two co-propagating pulses. For ultrashort pulses with a large spectral bandwidth energy can be transferred
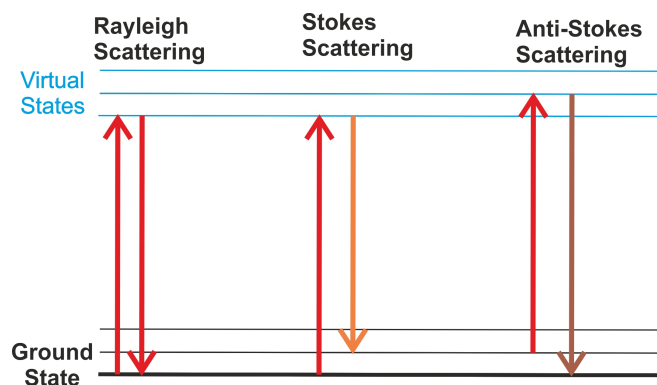

Figure 2.3.6: Schematic of the energy levels for Rayleigh and Raman scattering

from the higher frequencies in the pulse, acting as a pump, to the lower frequencies, shifting the pulse more and more to the longer wavelength side. This is known as intra-pulse Raman scattering.

Optical solitons

A soliton is a wave packet that can travel undistorted over long distances and will keep its shape. A soliton can be formed if dispersive and nonlinear effects balance out. We can understand the formation of solitons in two separate processes. If we first let SPM spectrally broaden a pulse of light, we have a pulse with a positive chirp and no temporal broadening. As a next step we think of the SPM being switched off and instead the dispersion with $\beta_2 < 0$ acts on the pulse, the chirp can be compensated again. By applying both mechanisms at the same time, a pulse can propagate without any distortions just by both effects compensating each other.

Before nonlinear effects and dispersion have been considered separately. We consider equation 2.27 for the cases of the ratio being either large in comparison to one or being small in comparison. We define the parameter N

$$N^2 = \frac{L_D}{L_{NL}} = \frac{\gamma P_0 T_0^2}{|\beta_2|} \tag{2.31}$$

For optical solitons we are now looking at the regime where both dispersion and nonlinear effects have a similar contribution, so $N^2 \approx 1$. Further the parameter N stands for the order of a soliton [67]. $N = 1$ is the fundamental soliton, where dispersion and SPM exactly even out, and a pulse travels without any temporal or spectral distortion. Higher order solitons are described by N being an integer greater than 1 and are called the N-th order soliton. As a higher order soliton propagates, its shape and spectrum changes periodically. The characteristic length z_0 over which the soliton returns to its original state is known as the soliton length z_0 [67].

$$z_0 = \frac{\pi}{2} L_D \tag{2.32}$$

If dispersion and SPM do not balance out exactly, one effect slightly dominates until the second one increases again and the pulse returns to its original shape. Higher order solitons are not stable while fundamental solitons are very stable as the pulse shape adjusts on its own to stabilise the soliton. A higher order soliton undergoing small perturbations like intra-pulse Raman scattering or third-order dispersion will be split into several fundamental solitons at different wavelengths. During the break up process fundamental solitons are ejected from the higher order soliton in the order of their peak power, the highest peak power and shortest duration first. After being ejected they undergo intra-pulse Raman scattering and are being shifted to longer wavelength.

Supercontinuum generation

The process of generating a broad spectral pulse from a narrow pump pulse is called super continuum generation. This allows to generate broadband white-light sources with laser characteristics. The process itself is a complex interaction of many different effects. The most important effects where discussed before, but other effects such as four-wave-mixing, Brillouin scattering or dispersive wave generation can participate as well. Supercontinua can be generated in many different media, like bulk solid matter as well as gaseous media. Optical fibres are a good way to generate supercontinua due to the long interaction length combined with the small core diameter which opens up possibilities to generate supercontinua while pumping at much lower peak powers in comparison to conventional media.

The formation of a supercontinuum strongly depends on the characteristics of the incident pump pulse. As SPM depends on $\frac{dI}{dt}$ it shows much stronger effects for ultrashort pulses. Pumping in the normal dispersion regime will lead to strong SPM and SRS effects, while pumping in the anomalous regime leads to soliton dominated processes.

The nonlinear pulse propagation in an optical fibre can be described by the nonlinear Schrödinger equation (NLSE), which can be found in many textbooks [67]:

$$i\frac{\partial u}{\partial z} + \frac{\partial^2 u}{2\partial\tau^2} + |u|^2\,u = i\delta_3\frac{\partial^3 u}{\partial\tau^3} - is\frac{\partial}{\partial\tau}\left(|u|^2\,u\right) + \tau_R u\frac{\partial\,|u|^2}{\partial\tau} \tag{2.33}$$

with $\tau = \frac{t - \frac{Z}{v_G}}{T_0}$, t is time, Z propagation distance, T_0 the input pulse duration, $z = \frac{Z}{L_D}$, $u = \sqrt{|\gamma|\,L_D A}$, A the pulse amplitude, $\delta_3 = \frac{\beta_3}{6|beta_2|T_0}$, $s = \frac{1}{\omega_0 T_0}$, $\tau_R = \frac{T_R}{T_0}$ and T_R the Raman time constant. The second-order dispersion is described by the second term on the left side, while the third term describes the nonlinearity. The terms on the right side describe the third-order dispersion, self-steepening and Raman scattering. Depending on practical considerations, assumptions might be made and some terms neglected for solving the NLSE. It can be solved with many different numerical methods, but especially the *split-step Fourier method* (SSFM) has been used extensively [71], [72]. While in general dispersion and nonlinearity act simultaneously along the fibre, the SSFM makes the assumption that the dispersive and nonlinear effects can be seen independently when propagating the optical field over a small distance.

2.4 Filling of hollow core fibres

The development of photonic crystal fibres (PCF) has opened up a new way of air guided optical modes. These hollow core fibres as well as simple glass capillaries have the potential to be filled with liquids in order to change their properties. Utilising different filling speeds depending on the diameter of the different cavities in a PCF even selective filling of cores is possible [73], [45].

To understand the filling of hollow core fibres and capillaries, it is important to review capillary forces. Upon bringing a flat surface into contact with a liquid droplet an interface will be formed. In the case of water a contact angle $\Theta > 90°$ will be formed for hydrophobic materials, while for hydrophilic materials the contact angle is smaller than $90°$. We look into the case of a hydrophilic material, that means that water will try to increase the contact surface with the material. For the case of a capillary this is schematically shown in figure 2.4.1.
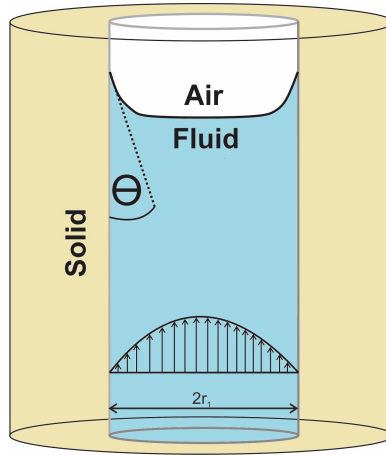
Figure 2.4.1: *Schematic of a capillary (yellow) filled with a liquid (blue) for a contact angle $\Theta < 90\,°$. The interface between air and liquid is shown as well as vectors indicating the filling speed of the liquid.*

The capillary is illustrated in yellow, while the liquid (blue) forms a contact angle Θ with the air (white) as it is typical for a hydrophilic material. For the contact angle Θ being smaller than $90\,°$ the liquid is pulled into the tube by the capillary force [73]:

$$F_C = 2\pi r_1 \sigma \cos \Theta \tag{2.34}$$

with the inner radius of the tube r_1 and the surface tensions σ. In the considered case four forces can act on the liquid: First the capillary force itself, the friction force, which is dependent on the viscosity of the liquid, a force originating from an applied overpressure, and the gravitational force. An important quantity to predict flow patterns of a fluid and different flow regimes is the Reynolds number Re, that is defined by the ratio of inertial to viscous forces. For a fluid in a cylindrical tube the Reynolds number is given by

$$Re = \frac{2r_1 \rho v}{\mu} \tag{2.35}$$

with the density of the liquid ρ, the velocity v and dynamic viscosity of the liquid μ. Typically for values smaller than 2100 laminar flow occurs and turbulent flow for values larger than 4000 with a transition region in between. To estimate the regime for a fibre capillary, water can be considered as a filling

fluid, a tube diameter r_1 of 5 μm and a velocity of a reasonable filling rate of $2.78 \cdot 10^{-4}$ m/s [74]. We can calculate for the Reynolds number Re=$2.77 \cdot 10^{-3}$. For this value we can assume a laminar flow, that is parallel circular layers of fluid that do not mix with each other. The fluid has the highest velocity in the middle of the tube, decreasing to the outside, and has a velocity of zero at the border of the tube. The spatial distribution of the velocity is indicated in figure 2.4.1 is a typical Poiseuille flow.

The friction for an established Poiseuille flow is given by

$$F_f = -8\pi\mu L v$$

with L being the length of the fluid column. An applied overpressure relates to the force $F_P = \Delta P \pi r_1^2$ with ΔP the applied pressure difference. Finally the gravitational force is given by $F_g = -\pi \rho r_1^2 L g$ with the gravitational constant g.

By balancing the different forces acting on the fluid a differential equation can be found that describes the filling of a circular tube with a viscous non-compressible liquid

$$\frac{d^2}{dt^2}\left(L^2\right) + B\frac{d}{dt}\left(L\right) + 2gL = A \tag{2.36}$$

The constants A and B are defined as

$$A = \frac{4\sigma\cos\Theta + 2\Delta P r_1}{\rho r_1}, \quad B = \frac{8\mu}{\rho r_1^2}$$

This differential equation can be solved with various numerical methods or for the case of neglecting the gravitational force in a horizontal setup also analytically.

In [73] theoretical methods are compared with experimental filling of a hollow core fibre. Figure 2.4.2 shows simulated times for water filling of silica capillary tubes. Different hole sizes are compared as well as including and neglecting the gravitational force. One can see that the filling can be speeded up by using larger hole diameters. A second observation is that for water the gravitational force in a vertical setup has to be taken into account for core diameters of 5 μm and above.
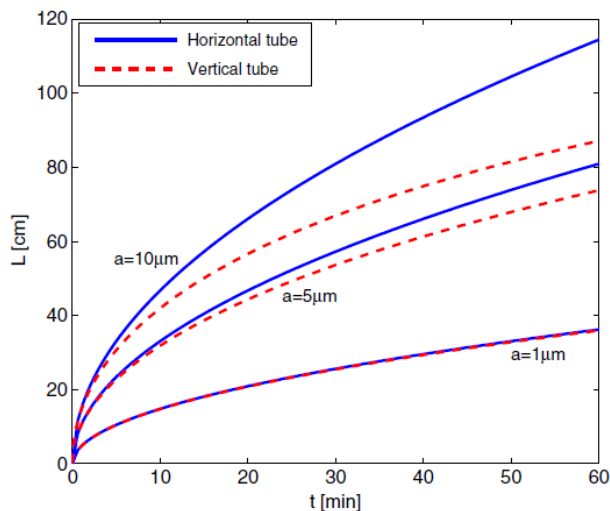
Figure 2.4.2: *Simulations of water filling time for silica capillary tubes for three different hole sizes. Simulations are shown including gravitational force (dashed line) and neglecting gravitational force (solid line)* [74].

2.5 Organic materials in Photonics

2.5.1 Electronic structure of π-conjugated materials

The electronic properties of organic semiconducting materials as they are used in this work are based on the molecular structure of the materials. The basic building block is the carbon atom. As explained in this chapter, carbon atoms can have different types of bonds, which leads to a vast amount of different organic semiconducting materials, from small molecules, with a few atoms in it, to large macromolecules with hundreds of repeating units. In the ground state, the electrons of a carbon atom are distributed within the orbitals in the following way: $1s^2 2s^2 2p^2$, with four electrons in the outer shell. When interacting with other atoms, new hybrid orbitals can be formed that are energetically favourable. These hybrid orbitals exist in different hybridisations depending on the number of covalent bonds formed and have different geometrical shapes and electronic properties. Using at least two and up to all four of the outer orbitals to form hybrid orbitals these are named sp, sp^2 or sp^3 hybrid orbitals. Not hybridised electrons stay in the shape of a p

sp³ carbon   sp³ carbon   sp³–sp³ σ bond
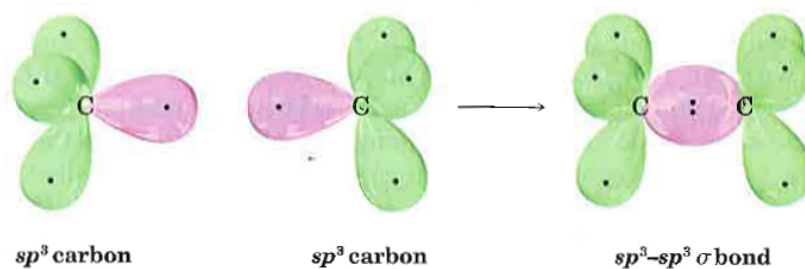
Figure 2.5.1: *On the left side two carbon atoms are shown with sp^3 hybrid orbitals. She hybrid orbital shown in pink is used to form a sigma bond between two carbon atoms [75].*

orbital. The hybrid orbitals align in order to maximise the distance in between each other in a 1-, 2- and 3-dimensional space, leading to a linear shape for two sp hybrid orbitals, a trigonal alignment with 120° angles in between for three sp^2 hybrid orbitals and a tetragonal shape for four sp^3 hybrid orbitals.

A single bond between two carbon atoms or a single bond between carbon and a different atom is formed by a direct overlap of the orbitals on the binding axis. For two carbon atoms this happens in a sp^3 hybridisation as shown in figure 2.5.1. On the left side one can notice two carbon atoms with the sp^3 hybrid orbitals, while the two binding orbitals are shown in pink leading to a σ-bond on the right side. As the electron wave functions overlap between the two nuclei this results in an energetically very favourable state. For this reason the lowest electronic transition between a binding σ orbital and an anti-binding σ* orbital has a high energy gap of the order of 4-5.5 eV [75], [76]. This makes the molecule capable of interacting with UV photons, but not with visible light.

For organic semiconducting materials the sp^2 hybridisation is of fundamental importance. As shown in figure 2.5.2 the three sp^2 orbitals are in a plane, while the remaining p orbital is found perpendicular to the plane. This configuration can show a different type of bonding than the σ bonding we have seen above. The strongest bonding is the σ-bond due to the direct overlap of the electron densities on the binding axis. In this configuration with the sp^2 hybridisation the carbon atom can have three σ-bonds to three different atoms. The additional perpendicular p orbitals allow a π-bond with another
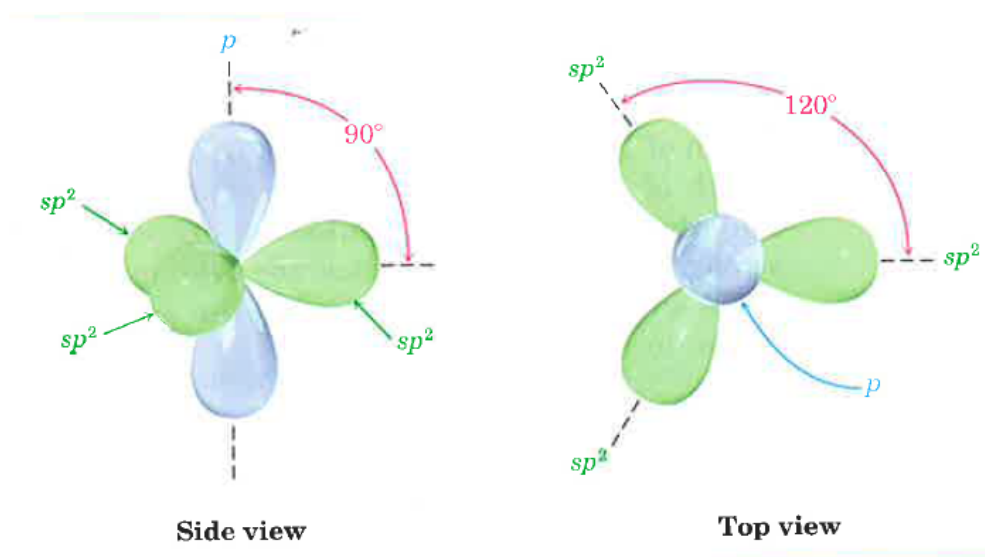
Figure 2.5.2: *Side and top view of a carbon atom with sp² hybrid orbitals in green and a remaining p orbital in blue [75].*

atom that has a singly occupied p orbital. In figure 2.5.3 on the left side two carbon atoms are shown with a sp^2 hybridisation. The pink coloured orbitals overlap to create a σ-bond, while the two green sp^2 orbitals can bond to other atoms. The remaining p orbitals (blue) are perpendicular to the plane of the sp^2 orbitals. On the right side a C=C double bond is shown with the σ-bond in pink and the π-bond in blue. The overlapping π-electron wave function is located above and below the bonding axis. As also illustrated in 2.5.3 the overlap of the wave functions of the p-electrons is smaller than in the σ-bond. This is a reason for the π-bond being weaker than the σ-bond.

The overlap of σ and π orbitals from both atoms creates bonding σ and π orbitals and anti-binding σ* and π* orbitals. The bonding orbitals are lower in energy with respect to the atomic orbitals, while the anti-binding orbitals are shifted to a higher energy. In the ground state, the molecule in figure 2.5.3 has four shared electrons, which occupy the binding orbitals as they are lower in energy. Figure 2.5.4 illustrates the energy levels for a C=C double bond. By forming molecular orbitals and occupying the binding orbitals only, the atoms of the molecule are in an energetically preferable state. The lowest excitation is from the π-level to the π*-level and can be as low as the order of
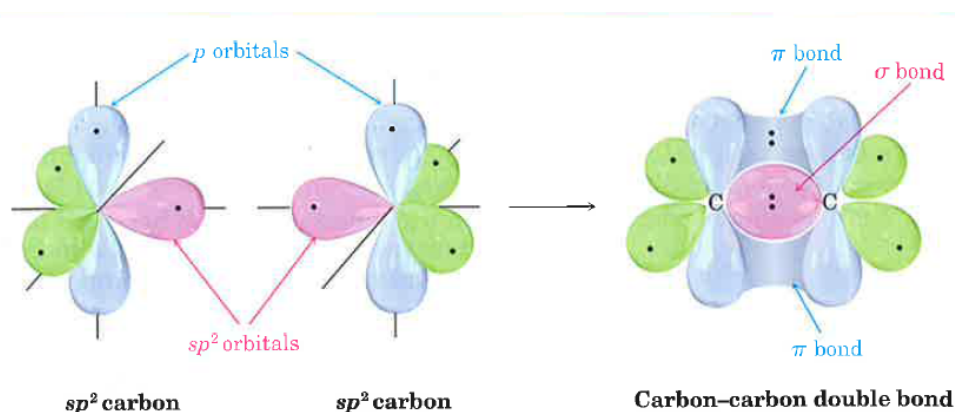
Figure 2.5.3: *On the left side two carbon atoms are shown with sp^2 hybrid orbitals (pink and green) and the perpendicular p orbital (blue). On the right sight the formation of a double bond between two carbon atoms is shown with a σ-bond (pink) and a π-bond (blue) [75].*

1.5 eV [77] and therefore can be excited by visible or UV photons. In general the highest occupied energy level is called highest occupied molecular orbital (HOMO) and the lowest unoccupied energy level is called lowest unoccupied orbital (LUMO). They can be seen in analogy to the band theory for classical semiconductors forming the valence and conduction band.

Between two carbon atoms a triple bond can be also formed. In this case both atoms have a sp-hybridisation that can form a σ-bond. The two remaining p orbitals are perpendicular to the linear sp orbital and also perpendicular to each other. Like for the sp^2-hybridisation the p orbitals can form a π-bond, but in this case two π-bonds. The most simple examples for a carbon single, double and triple bond molecules are ethane, ethylene and acetylene as shown in figure 2.5.5.

So far bonds between two carbon atoms have been explained. The electron wave function is localised in vicinity of the two atoms. Larger molecules can show the very interesting and important effect of the delocalisation of the π-electrons. A typical example of this effect is benzene, which consists of six carbon atoms with one hydrogen atom attached to each in a hexagonal ring. Figure 2.5.6 (a) shows the chemical structure of benzene, with a single and a double bond alternating between the carbon atoms. The hexagonal structure is formed by σ-bonds, while for the π-bonds different possibilities to distribute
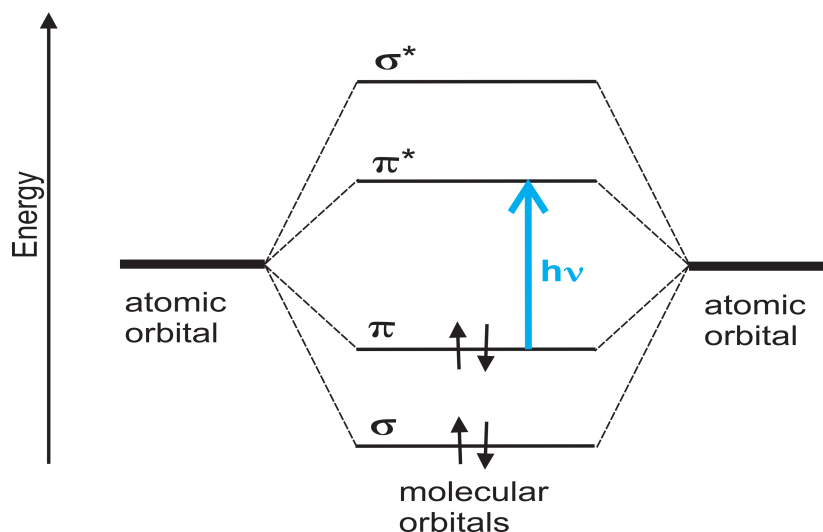
Figure 2.5.4: *Schematic diagram of energy levels of a C=C double bond. The atomic orbitals form binding σ and π orbitals and anti-binding σ* and π* orbitals. All binding orbitals are fully occupied, so the lowest optical excitation can be found from π to π*.*
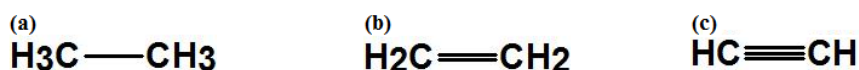

Figure 2.5.5: *Chemical structure of (a) ethane, (b) ethylene and (c) acetylene.*

them can be found . A single and a double bond has to alternate, which gives two isomeric structures shown in figure 2.5.6 (a) and (b) with different places for the π-bonds.

Both of these isomeric structures have no energetic preferable configuration. X-ray diffraction measurements confirm the same bonding distance for all carbon-carbon bonds in benzene with a distance that is in between the distance for a single and a double bond [75], [78]. As indicated by these observations, the π-electrons in benzene are delocalised over the whole molecule and form a conjugated π-electron system.

In figure 2.5.6 (c) this is indicated by a ring inside the benzene hexagon instead of double bonds. These conjugated electron systems are not limited to structures like benzene, but larger molecules like polycyclic aromatic hydro-carbons can be found as well as conjugated polymers like polyacetylene that is shown in figure 2.5.7.
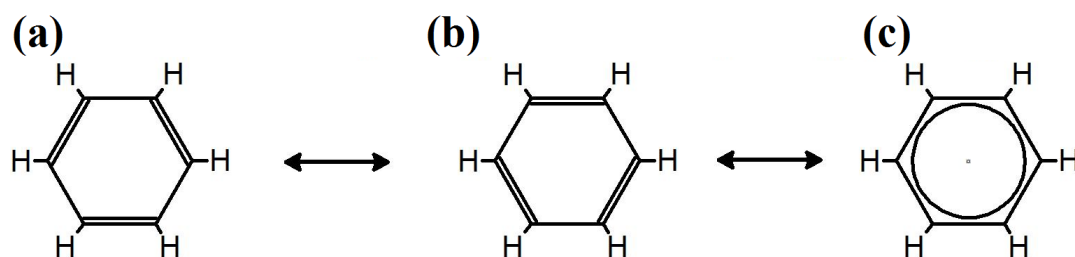
Figure 2.5.6: *Chemical structure of benzene. In (a) and (b) two different isomers of benzene are shown, (c) shows benzene with delocalised electrons.*
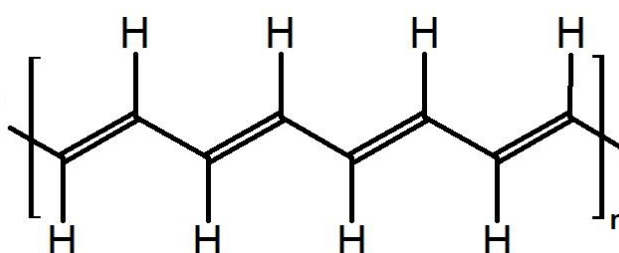

Figure 2.5.7: *Chemical structure of the conjugated polymer polyacetylene with n repeating units and alternating single and double bonds between carbon atoms.*

Starting from this point one would expect the semi-filled band of perfectly crystalline π-conjugated polymer to show metallic behaviour. In contrast to this experiments suggest a semiconducting behaviour. This can be understood by considering the Peierl's transition [79]. In a one-dimensional system with incompletely filled bands and a periodic structure, a distortion periodically decreasing and increasing the distance between next neighbours leads to a doubling of the elementary cell of the system. Such distortions can be introduced by the alternating single and double bonds. Similar to the band gaps in the Kronig-Penney-model for classical semiconductors [76], a energy gap E_G is created between the bonding π- and anti-bonding π^* orbitals. This explains the semiconducting character instead of a metallic one. The analogy to the valence and conduction band in a classical semiconductor are the HOMO and LUMO for π-conjugated materials. The value of the energy gap E_G depends on the length of delocalisation and gives a parameter to engineer band gaps and other properties to the desired functions.

2.5.2 Optical properties of π-conjugated molecules

We have shown above that an energy gap between the HOMO and LUMO of π-conjugated materials exists. In this section we will define the ground state S_0 and the exited states S_n with n being an integer. The energy difference between the ground state S_0 and the first excited state S_1 typically is of the order of 1-3 eV [77], which allows the absorption of visible light and makes optical spectroscopy an ideal tool to investigate the electronic structure of these materials. With the absorption of a photon the molecule undergoes a transition from the ground state to an excited state and has different paths for the relaxation, either through radiative or non-radiative emission of the absorbed energy.

Figure 2.5.8 (a) shows a potential energy curve plotted against the configuration coordinate Q. From the ground state S_0 the molecule can be excited to different vibrational modes ν_1 in the excited state S_1. The transition from S_0
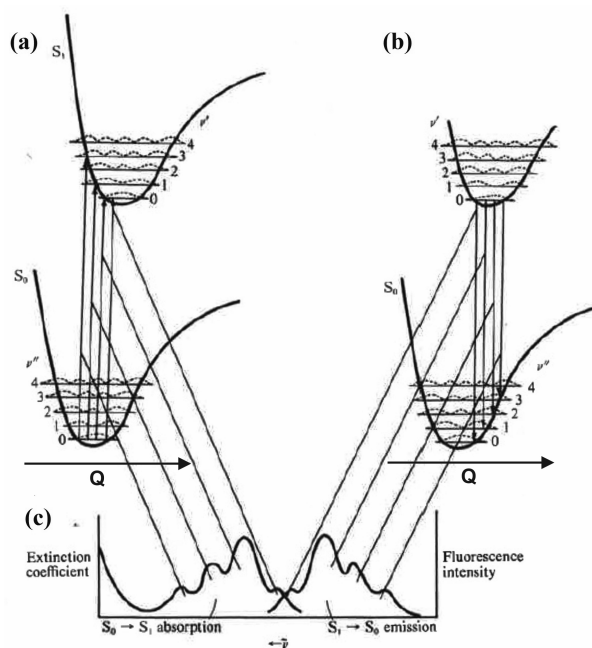

Figure 2.5.8: *Simplified potential energy curves with the x-axis being the configuration coordinate Q. (a) shows the absorption from the ground state S_0 to S_1 with vibrational states ν_n, (b) shows the radiative emission for the same system and (c) the combined absorption and emission spectrum [80].*

to S_1 changes the electronic structure and therefore the position of the nuclei, which ultimately means that the electronic potential is shifted along the Q-axis with respect to the ground state. In the Born-Oppenheimer approximation, that separates the motion of electrons and nuclei because of the small mass of electrons compared to the nuclei, the electronic transition does not affect the nuclei on the excitation time scale. This description is known as the Franck-Condon principle [81], [82]. In the picture used this means that the excitations can be drawn as vertical lines in the scheme. At room temperature and for most molecules only the lowest vibrational mode of the ground state, $S_{0,0}$, is populated and therefore the absorption processes start from the $S_{0,0}$ state. For the possible excited states different vibrational modes ν_n are available, depending on the exciting photon energy:

$$S_{0,0} \mapsto S_{1,n}$$
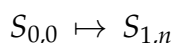
In figure 2.5.8 (b) the radiative relaxation can be seen as vertical down pointing arrows. Usually photon emission is only observed from the lowest vibrational state. Immediately after the photo-excitation non-radiative processes lead to a relaxation of the higher vibrational states to the lowest, $S_{1,n} \mapsto S_{1,0}$, happening on the time scale of 10^{-13} s [83] before the slower process of the photo-emission will return the system to the ground state. The system can return into different vibrational levels of the ground state

$$S_{1,0} \mapsto S_{0,n}$$
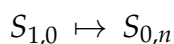
from where non-radiative processes will return it to the lowest vibrational state. Figure 2.5.8 (c) shows the absorption and emission spectrum of the two phenomena involving light. The absorption to the lowest vibrational state gives the lowest absorption energy, with additional peaks according to the vibrational levels at higher energies. The same pattern can be observed for the emission of photons with a mirror symmetry as the emission to the lowest vibrational state reflects the highest photon energy while the lowest vibrational state reflects the lowest transition energy. Both spectra are characterised by

an onset due to the energy gap. Comparing the absorption and emission for the first maxima , a spectral shift can be observed that is called Stokes shift. The main reason for this shift is energy loss due to non-radiative emission during the relaxation process, but also solvent effects in solution or neighbour molecules in a crystal are affecting the shift.

So far only a two level system was considered without incorporating any spin-effects. To present a more complete picture both spins and higher level excitations have to be integrated. Taking spin into consideration, we can differentiate two possibilities: singlet states have a total spin of zero, formed by electrons with opposite spins, while the triplet states have a spin of one with electrons with parallel spin in different orbitals. The ground state is a singlet state and possible transitions are dictated by the spin conservation rule. Therefore, optical transitions between a singlet and triplet state are forbidden and only singlet states are excited from the ground state. However, spin-orbit coupling can make the transition from a singlet state to a triplet state weakly allowed.

A method to display the complete process is a Jablonski-diagram as shown in figure 2.5.9 which displays all the important transitions for an organic molecule [84]. It shows the ground state S_0 together with the higher singlet states S_1, S_2 on the left side and the triplet states T_1 and T_2 on the right. Radiative transitions are indicated by solid lines, while the non-radiative transitions are indicated by dashed/dotted lines. Each level can be further divided into different vibronic sublevels. When an excited state is created from the ground state by photon absorption, fast internal conversion leads to a relaxation to the lowest excited state S_1. Only from this state efficient photo-fluorescence can occur according to Kasha's rule [85], [86]. The reason is the much shorter time-scale of the internal conversion . In addition due to spin-orbit coupling a weak inter-system crossing to the triplet state is allowed. In the triplet state two electrons have the same spin which means they have to be in different orbitals according to the *Pauli*-principle. This means a larger spatial separation and less repulsion which finally lowers the triplet state energetically in comparison to the singlet state. From the triplet state a photon can be emitted by phosphorescence to the ground state. These transitions
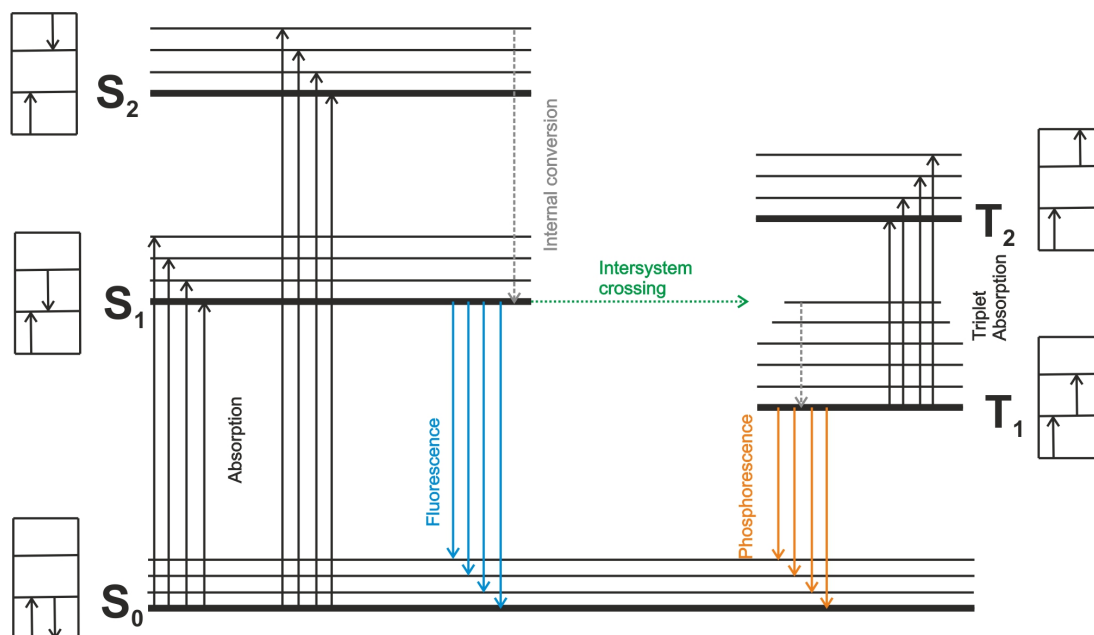
Figure 2.5.9: *Jablonski diagram for the optical transition of an organic molecule. On the left side singlet (S_n) energy levels are shown, on the right side triplet (T_n) levels. Absorption is illustrated in black, fluorescence in blue, phosphorescence in orange, internal conversion in grey dashed lines and inter-system crossing in green dotted lines. The disposition of electrons for the respective energy level is shown in boxes.*

are only weakly allowed and therefore much longer lifetimes (>1 µs) for the phosphorescence in comparison to the fluorescence are observed.

2.5.3 Excitons in organic solids

Photo-excitations for isolated molecules have been discussed in the previous section. More specifically in π-conjugated polymers and molecules an excited electron remains bound to the hole. This bound state is called exciton [83]. An exciton is a neutral quasi-particle consisting of an electron and a hole that are bound together by the Coulomb interaction. Excitons are not limited to organic semiconductors, but show differing properties in organic and inorganic semiconductors. Two main properties of excitons are the binding energy E_b and their spatial extent. The binding energy is mainly determined by the effective Coulomb attraction, that can be influenced by electron-electron and
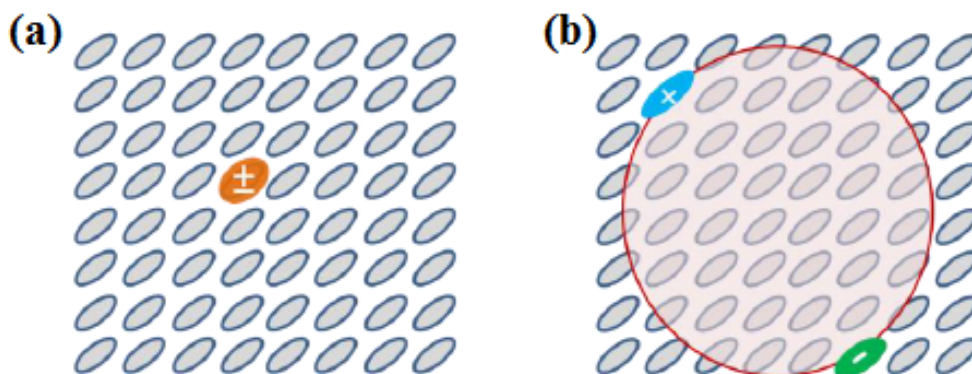
Figure 2.5.10: *Clarification of excitons: (a) Frenkel excitons with a strong localisation and high binding energy and (b) Wannier excitons with low binding energy and large spatial delocalisation [83]*

electron-lattice interactions. Overcoming the binding energy will lead to the formation of free charges. Inorganic semiconductors have high dielectric constants, silicon for example has a dielectric constant of $\epsilon \approx 11$, while organic semiconductors typically show dielectric constants in the range of $\epsilon \approx 3 - 4$.

This highly affects the Coulomb interaction, as inorganic semiconductors show a much stronger screening effect, that means excited electrons experience less Coulomb attraction from the positive hole. In contrast organic semiconductors have a much lower screening effect leading to a stronger binding of the electron-hole pair. Different types of excitons can be distinguished: the Frenkel and the Wannier excitons are depicted in figure 2.5.10 (a) and (b) respectively.

Inorganic semiconductors show Wannier excitons due to the high screening. As the attracting Coulomb-force is reduced by the screening electrons, the electron and hole can move further apart from each other with a diameter of up to 5 nm. The binding energy for silicon for example is of the order of 15 meV [87], which means that they can already be dissociated by the thermal energy $k_B T \approx 25$ meV at room temperature. For organic semiconductors, however, the binding energy is of the order of 0.3 - 0.5 eV [88], [89], which manifests in a strongly bound electron-hole pair, that is typically localised on one molecule. This type of exciton is called Frenkel exciton and illustrated in figure 2.5.10 (a).

2.5.4 Polarons in organic solids

After discussing the uncharged excited electron-hole pairs above, we are considering the creation of a charge-carrier by addition or removal of an electron to the ground state. Because of the weaker screening effect in an organic semiconductor the Coulomb force of the injected charge-carrier will interact with molecules in its vicinity. As visualised in figure 2.5.11 the central charge will lead to a deformation of the surrounding lattice and in this way introduce a polarisation. Similar to the quasi-particle of the exciton discussed above, a polaron is the quasi-particle describing a charged particle [90], [91].
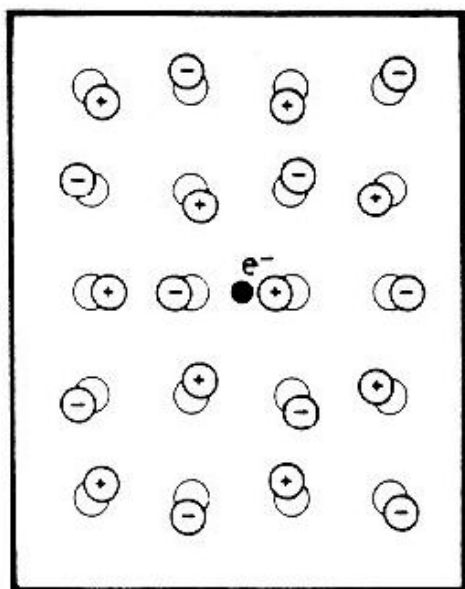
Figure 2.5.11: Schematic of a polaron [92] : A negative particle in the middle attracts positive and repels negative surrounding particles. A polarisation is induced due to the displacement from the equilibrium position.

Lev Landau has proposed the concept of a polaron the first time to describe an electron propagating through a crystal lattice with a lattice deformation following its propagation [93].

For organic semiconductors a strong coupling between charges and molecular vibrations is observed, leading to a short ranged interaction in the close vicinity of the charge. The induced polarisation changes the geometrical order, for conjugated polymers that means a change of the bond-lengths along the polymer backbone. In this way a new equilibrium state is formed together with new polaron energy levels. These new energy levels are positioned between the HOMO and LUMO of an organic semiconductor. Being in the band gap of the organic semiconductors, polarons open up new optical transitions. Depending on the injected charge, the polaron energy level can be found below the LUMO or above the HOMO. Transitions can be found between these different, charge-dependent

polaron levels as well as between the polaron level and the HOMO/LUMO, making them accessible by spectroscopic measuring methods in the NIR or MIR.

2.5.5 Nonlinear optical effects in organic crystals

In chapter 2.3.4 NLO effects have been discussed that play an important role for optical fibres. The origin of nonlinear effects can be seen in equation 2.37, defining the polarisation P of a dielectric medium as a function of the electric field E.

$$\mathbf{P} = \mathbf{P}^{(1)} + \mathbf{P}^{(2)} + \mathbf{P}^{(3)} + \ldots = \epsilon_0 \left(\chi^{(1)} \cdot \mathbf{E} + \chi^{(2)} \cdot \mathbf{E}^2 + \chi^{(3)} \cdot \mathbf{E}^3 + \ldots \right) \quad (2.37)$$

$\mathbf{P}^{(n)}$ describes the n-th order of polarisation with the corresponding optical susceptibility $\chi^{(n)}$. While $\chi^{(1)}$ describes linear material properties, higher orders describe NLO effect. For these the material response is not anymore linearly following the electric field E of incident light. As the efficiency strongly decreases with the order n of the polarisation, NLO effects can be only observed at high light intensities. Only through the invention of the laser, these effects were accessible and short laser pulses with high peak powers are favourable to study NLO effects.
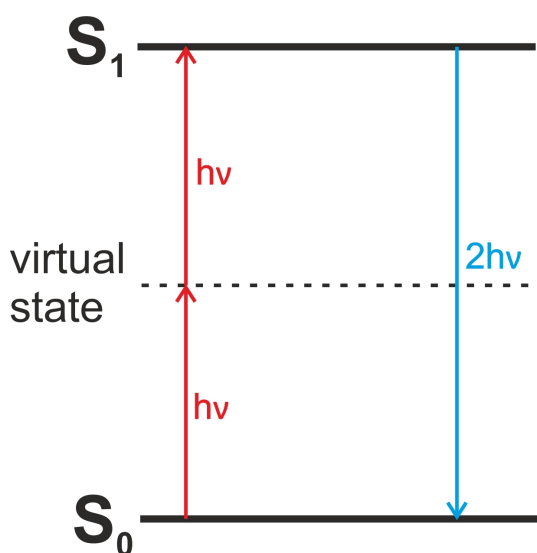
The second order term is describing effects like second-harmonic generation, sum frequency generation, parametric amplification or the electro-optical effect. The nonlinear refraction originating in the third order term has been discussed more detailed in chapter 2.3.4, but also effects like stimulated Raman and Brillouin scattering, four wave mixing, third-harmonic generation and two photon absorption (TPA) are ascribed to $\chi^{(3)}$. Because of symmetry reasons, second order effects (and higher even-order effects) are only unequal from zero for materials without an inversion centre.

Nonlinearity has different origins for organic and inorganic materials. The polarisability of a crystal is influenced by contributions of each single atom or molecule in the crystal lattice as well as by their interaction. Inorganic materials

show only weak polarisability of the atoms, while lattice interactions dominate. Organic crystals on the other hand only show a weak intermolecular bonding and can be described by an oriented gas model, and therefore are dominated by the contributions of the molecules rather than their interaction [94]. Finally this connects the nonlinearity of an organic crystal to the polarisability of its electrons, with the main contribution coming from the conjugated π-electrons.

Different possibilities arise from the origin of the nonlinearity to influence the nonlinear properties of organic materials. For second order effects different models have been used to describe the structural dependence [95], [96]. The introduction of substituents is strongly influencing the distribution of delocalised electrons. Donor and acceptor substituents in para configuration generate an asymmetry and can increase the nonlinearity substantially [97]. Besides of donor and acceptor structures, the length of the conjugated system increases the nonlinearity as the delocalisation length of electrons increases [98], [99].

Unlike for the second order polarisability, third order effects are not yet as well understood and the same models cannot be applied here [100]. However, an increasing conjugation length can still be found to increase the third order nonlinearity [101] being in accordance with calculations using a simple free electron gas model [102].

In the process of TPA two photons are simultaneously absorbed, raising a molecule or material into an excited state. The two photons can either have the same energy (degenerate TPA), typically excited by one laser source, or different energies from two laser sources, allowing more spectroscopic techniques to be used. We concentrate on the degenerate case, but information about non-degenerate studies can be found for example in [103], [104].

The energy schematic in figure 2.42 is visualising the TPA effect: two photons with the energy $E_{p1} = E_{p2} =$

Figure 2.42.: Schematic of TPA: photon absorption (red) from the ground state S_0 to the excited state S_1 and emission (blue).

$h \cdot \nu = \frac{1}{2} \left(E_{S_1} - E_{S_2} \right)$ being half of the energy difference between the ground sate S_0 and the excited state S_1 are absorbed simultaneously. The simultaneous absorption is important for the TPA and different from a two-step excited state absorption. In the case illustrated one photon can create a virtual state, but no real state exists at this energy that can be populated. Especially this allows two photons to overcome a band gap, where one-photon absorption is not possible [105]. With the path of excitation being unrelated to relaxation processes, the relaxation process is not distinguishable from one-photon excited relaxation processes. One way of observing TPA is through consecutive two photon excited fluorescence as indicated in figure 2.5.12 with the blue arrow.

Different theoretical approaches can be used to calculate the the transition rate for two photon absorption. In [106] a microscopic approach is used to calculate the transition rate Γ_{gf} for a electric dipolar transition by

$$n_0 \Gamma_{gf} = \frac{32\pi^2}{c^2 \hbar} I_1 I_2 \tilde{\chi}^{(3)} = \frac{1}{2\hbar} |E_1|^2 |E_2|^2 \tilde{\chi}^{(3)} \tag{2.38}$$

with Γ_{gf} being the transition rate per species from a ground state $|g\rangle$ to a final state $|f\rangle$, n_0 the density of species, I_1 and I_2 the light intensities and $\tilde{\chi}^{(3)}$ is defined by $\chi^{(3)} = \hat{\chi}^{(3)} + i\tilde{\chi}^{(3)}$. An important result from this equation is the TPA being a third order NLO effect and for that reason TPA can be also found for materials with an inversion centre. The TPA is proportional to the product of the intensities I_1 and I_2 or for degenerate TPA to I^2, which can be easily understood qualitatively by the interaction of two photons in one process.

3 Experiental Techniques

This chapter gives details about experimental techniques used for the work of this thesis. In section 3.1 different techniques are presented for optical characterisation methods, followed by a short overview of materials and preparation methods used in section 3.2.

3.1 Optical Characterisation

3.1.1 Cross polarised microscope

One of the most basic methods to characterise a sample is the optical microscope. Light microscopes give the possibility to create magnified images of small samples, with a resolution comparable to the wavelength of light. Briefly, a set of lenses creates a magnified virtual image that can either be seen by eyes or detected with a camera. A typical microscope uses an objective close to the sample and a second lens (or set of lenses) in the eye piece, with the total magnification given by the product of the magnification of the eyepiece and the objective. Many different configurations of the light microscope are available, adapted for different uses and samples in order to give better quality pictures [107].

In this work the optical microscope was used to characterise the filling of hollow core fibres with organic crystals. With the crystal being inside the core of the hollow fibre, optical characterisation is often more difficult due to focusing, reflections and a low contrast. To improve the contrast cross-polarised microscopy was used exploiting the birefringent properties of the organic crystals. The principle is illustrated in figure 3.1.1.
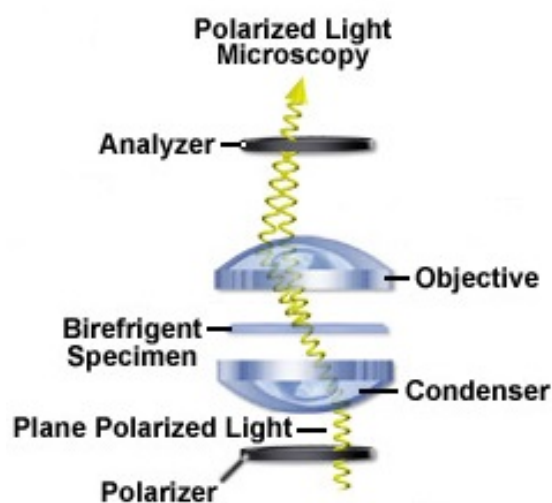
Figure 3.1.1: *Schematic of the important components for cross-polarised microscopy [108]*

Light from the bottom light source is passed through a polariser creating linear polarised light. Without a sample the light passes through the objective and is send through a second polariser called the analyser. By rotating the polarisation plane by 90° with respect to the first polariser no light is transmitted due to the orthogonal polarisation. With a birefringent sample in the light-path, that shows optical activity, the polarisation plane of light transmitted through the sample is rotated. Solely this light will be able to pass through the analyser, which gives a highly increased contrast between the organic crystal and the hollow core fibre.

A *Nikon LABOPHOT-2* was used for this work with both top and bottom illumination and objectives between $5x$ and $60x$ magnification. For the cross-polarised microscopy only the bottom illumination was used with a rotating linear polariser added directly after the light source and a fixed polariser in the beam-path before the eyepiece.

3.1.2 Absorption spectroscopy

Optical transitions and especially the band gap of a material can be studied using absorption spectroscopy. Measuring the intensity of monochromatic

light before and after the sample can determine the absorbance A of a sample. The absorbance is given by

$$A(\lambda) = -\log_{10}\left(\frac{I(\lambda)}{I_0(\lambda)}\right) \tag{3.1}$$

with I the light intensity after the sample and I_0 the light intensity of the source before the sample. Absorption measurements in this work were done using a *Cary*5000 absorption spectrometer. The basic layout of the spectrometer is shown in figure 3.1.2.

The *Cary*5000 can perform absorption measurements in the range of 200 nm up to 3300 nm using a deuterium light source for the UV and a halogen light source for the visible and NIR. Both light sources generate a broad spectrum, that is passed through a grating and slits constituting the monochromator.
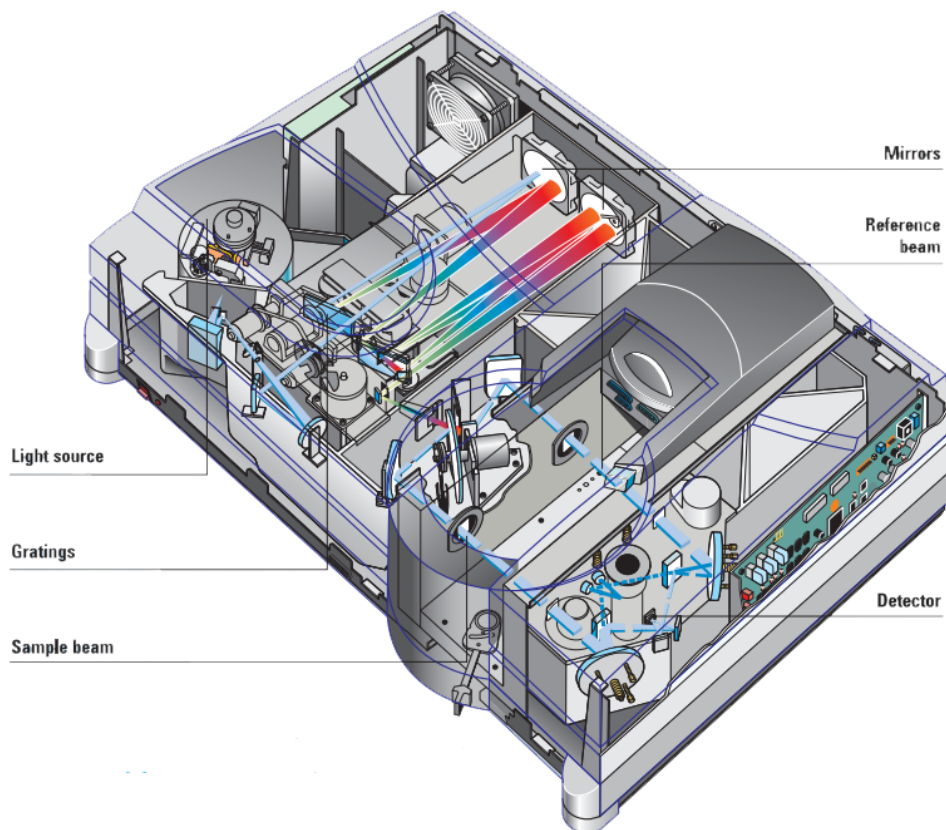

Figure 3.1.2: Schematic of the Cary5000 absorption spectrometer [109]

The monochromatic beam is split into two beams, one is sent through the sample and afterwards detected , measuring $I(\lambda)$. The second beam is called the reference beam and is used to measure $I_0(\lambda)$, simultaneously correcting also for fluctuations in the source intensity. Measurements can be carried out in solution or a transparent substrates. Absorption of the solvent or the substrate/cuvette are corrected by a baseline measurement of the blank substrate/cuvette that is automatically subtracted by the software.

3.1.3 Optical dispersion interferometer

To measure the dispersion of optical fibres an interferometer setup was used. The setup can be seen schematically in figure 3.1.3. A broadband light source is used consisting of a photonic crystal fibre (PCF) pumped by a microchip laser at 1064 nm with sub-nanosecond pulses. A beam splitter (BS1) divides the light source into two beams, one is focused into the fibre to be measured, while the second reference beam is passed through the same optics in order to minimise differences in dispersion for both beams. The second beam is passed through a delay line to compensate the difference in optical bath length for both beams. After the reference beam is passed through a linear translation stage, both beams are sent through another beam splitter BS2 to be combined again. Bandpass filters (BP) with different centre wavelengths are used to selected the wavelengths of the light to be measured. Finally the light is
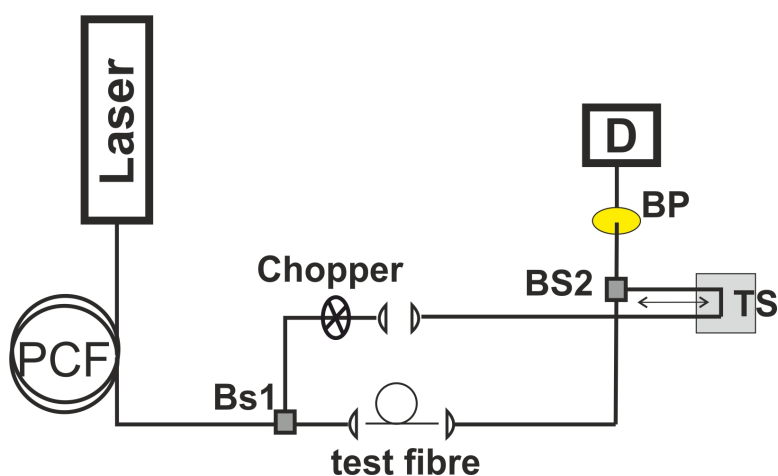
focused to a photo-diode. To increase the signal-to-noise ratio, an optical chopper is integrated into the reference beam beam and used as a reference for an lock-in amplifier that analyses the signal from the photo-diode. The light intensity is recorded while the translation stage changes the delay of the reference beam with respect to the test beam until a fringe originated in the interference of both beams is detected. At this point the position of the interference can be recorded in dependence of the wavelength.

Knowing the length of fibre l, the shift of the position Δl and the shift in wavelength $\Delta\lambda$ per measurement point the GVD can be calculated according to equation 2.18. Here we use the dispersion parameter D from chapter 2.3.2, given in shift in time per wavelength and length of the medium ($\frac{ps}{nm \cdot km}$).

3.1.4 Ellipsometer

Ellipsometry offers a method to study optical properties of thin films that is non-invasive. Figure 3.1.3 describes the typical setup. A broadband light source shines polarised light on on a substrate with a thin film on top and elliptically polarised light is reflected. Through the analyser the light is detected in dependence of its polarisation. While light with a polarisation parallel to the plane of incidence is referred as p-polarised, a polarisation perpendicular to the plane of incidence is called s-polarised. The measured quantity is ρ, which gives the ratio of p-polarised to s-polarised of the reflected beam and is defined by
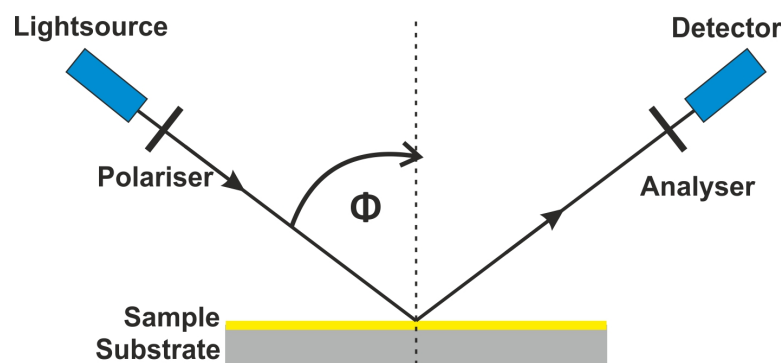

Figure 3.1.3: *Schematic of an ellipsometry setup*

$$\rho = \frac{r_p}{r_s} = \tan(\psi)\exp(i\Delta) \tag{3.2}$$

ρ is a complex number with the amplitude $\tan(\psi)$ and the phase Δ. With one measurement point containing both parameters ψ and Δ as a function of the wavelength λ more information is gained in comparison to a simple reflection measurement. Measuring the ratio of two reflection components make the measurement independent of the light intensity. From the measured data parameters have to be extracted by fitting an optical model to the measured data [110].

In this work the alpha-SE ellipsometer was used, covering a wavelength range from 380 nm to 900 nm. The data fitting can be directly executed in the controlling software *CompleteEASE* using different models and parameters. Both the film thickness and the refractive index of the film can be extracted from the fitting model.

3.1.5 Raman spectroscopy

Raman spectroscopy investigates the inelastic scattering of photons due to energy transfer to or from vibrational modes. The energy of different vibrational modes is a specific value for different bonds or lattices in matter. Measuring these energy levels gives a "finger print" of the material as well as giving indications of impurities. To measure the Raman shift the sample is excited by a laser beam and the scattered light is collected. To inspect the inelastically scattered light only and detect the weaker Raman signal with the strong background of the elastically scattered laser light, a notch filter or an edge filter is used to cut out the elastically scattered laser light. The light is then send to a spectrometer to record the spectrum as a shift relative to the excitation wavelength measured in cm^{-1}.

For all the experiments of this work a *RenishawinVia* Raman microscope was used. A picture of the Raman microscope together with a scheme of the light path is shown in figure 3.1.4.
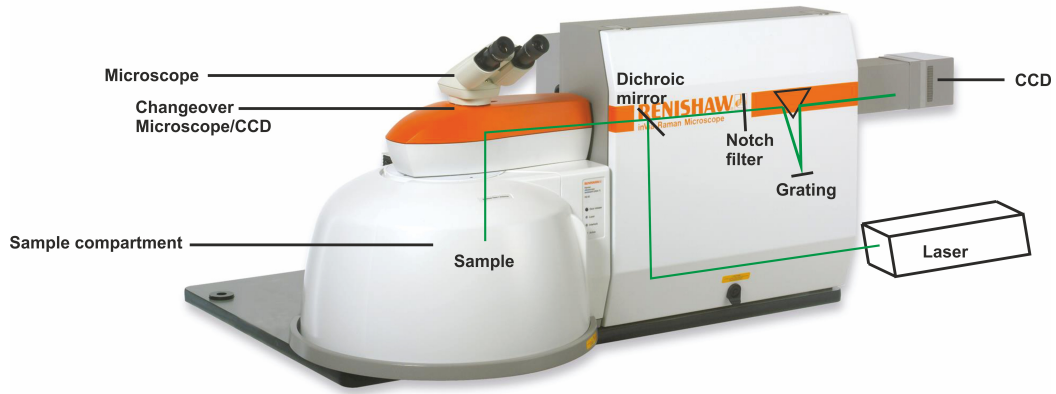
Figure 3.1.4: *Renishaw inVia Raman microscope*

For the light source three different lasers are available, a UV-laser with 325 nm and two visible laser at 532 nm and 685 nm. The excitation light is sent through an optical microscope with variable objectives which allows to conduct experiments on small samples as well as varying the size of the measurement volume. For alignment the sample can be observed directly through the microscope or via camera. For measuring the Raman intensity the light is sent through a notch filter and a monochromator to a CCD camera to record a spectrum.

3.1.6 Ultrafast laser system

The laser system of from *Coherent* consists of 6 different components in total, which are schematically shown in figure 3.1.5. Two diode-pumped solid state (DPSS) frequency-doubled $Nd : YVO_4$-laser of the Type Verdi V-5 and V-10 are used as pump lasers at 532 nm. The V-10 optically pumps a regenerative amplifier (RegA), while the V-5 pumps a Titanium:Sapphire(Ti:Sa)-oscillator (MIRA) which generates the femtosecond-pulses with a pulse-length of about 120 fs. The pulses from the oscillator are used as seed-pulses and are amplified in the RegA. Finally the amplified pulses feed one of the two optical parametric
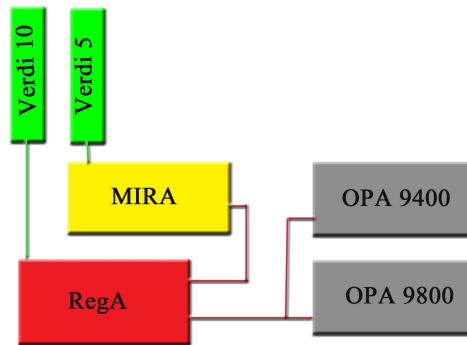
Figure 3.1.5: *The Laser-System with the two Verdi pump laser, the Titan:Sapphire oscillator MIRA, the regenerative amplifier (RegA) and two optical parametric amplifiers (OPA)*

amplifiers (OPA), where the beam can be split into the needed pump and probe-beam with a tunable photon energy (wavelength).

Regenerative Amplifier

The Ti:Sa amplifier has the potential for high repetition rates up to 250 kHz with a high average power of ultrafast pulses. The average power is determined by the available pump power and the repetition rate of the system. The CW-pumped laser power is limited by the laser storage time of the gain medium (T_2), which is in this case about 2,5 μs [111]. The maximum energy per pulse is given by $E_p = P_{CW} \cdot T_2$. For repetition rates higher than $\frac{1}{3}T_2$ the pulsed energy is reduced because of the storage time. We were running the system at a repetition rate of 125 Â´250 kHz which is a compromise between pulse energy and the average power. This gives an average power of over 1 Watt which corresponds to an energy of 4 μJ.

The central part of the amplifier is a Ti:Sa crystal that is optically pumped by the Verdi-10 Laser. Next to the crystal, the Q-switch, the cavity dumper and the Faraday-isolator are important parts inside the amplifier followed by a pulse compressor at the end of the amplifying process. The amplifier cavity has a similar length as the oscillator cavity of the MIRA, which allows to use the 76 MHz drive signal from the MIRA to synchronize the electronics of the
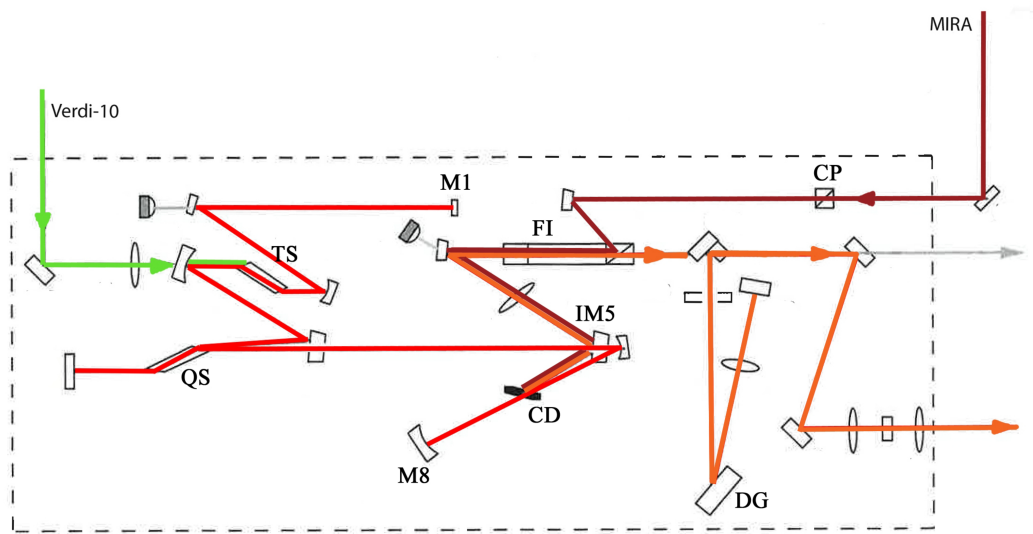
Figure 3.1.6: *Scheme of the RegA with the Ti:Sa-crystal (TS), the Q-Switch (QS), the Cavity Dumper (CD), the Faraday Isolator (FI), the Cubic Polariser (CB) and the Differential Grating (DG)*

amplifier to the incoming pulses from the MIRA. In figure 3.1.6 a scheme of the RegA is shown.

The Verdi-10 (green) pumps the Ti:Sa-crystal (TS) inside the cavity (red) which is built between the mirrors M1 and M8. The Q-switch (QS) is used inside the cavity to keep the energy below the lasing-limit for most of the time in order to store energy in the Ti:Sa-crystal for the amplification process. The QS is an acousto optic modulator (AOM using a TeO_2-crystal controlled by 80 MHz radio frequency (RF)-excitation. The QS diffracts a part of the beam out of the cavity to prevent lasing until a pulse from the MIRA is injected through the cavity dumper (CD). At this point the QS is turned off and the gain in the cavity increases. In about 20 - 30 cavity round trips the pulse is amplified and after the ejection of a single pulse the QS will be turned back on. The second function of the QS is to spread the seeding pulse from the MIRA out in time during the round trips for amplification. This is needed for a safe operation of the system without damaging optics because of the increasing pulse energy per round trip. After optimal pulse amplification the

pulse length is about 40 ps and needs to be compressed in time to a temporal length of about 120-140 fs in order to generate the desired short laser pulses with high peak powers.

To inject a pulse from the MIRA (dark red in figure 3.1.6) into the cavity and to eject an amplified pulse from the cavity (orange in figure 3.1.6) the CD is used. This is a high speed AOM. It is a TeO_2-crystal which is driven by a 380 MHz RF excitation, which allows to create a short acoustic pulse that only diffracts one single pulse from the 76 MHz pulse train coming from the MIRA into the RegA cavity. As soon as the QS is turned off the CD will inject a single pulse from the MIRA and close to the saturation energy the CD will eject the amplified pulse over the pick-off mirror IM5.

A Faraday-Isolator will separate the incoming MIRA-pulses from the outgoing amplified pulses. For separating the beams the Faraday-rotation is used, which allows to have a rotation of the polarisation only in one direction of transmission while the other direction stays unaffected. Combined with two polarisers at both ends it is possible to select only one direction to be let through depending on the polarisation. In this case only the horizontally polarised output beam will be let through while the MIRA input beam is vertically polarised before the injection, so any outgoing beam from the MIRA will be extinguished.

As mentioned above the injected MIRA pulse is stretched during the amplification process to about 40 ps. The MIRA generates fs pulses with a bandwidth of 10 nm and the spectral components are not changed by the amplification, only a chirp is introduced in the group velocity dispersion. The pulse length of the MIRA can be recovered by reversing the chirp. To achieve this a single grating 4-pass pulse compressor (DG) is used. In fig. 3.1.6 only one beam is shown between the grating (DG) and the mirror, but 4 passes through the grating are used. These passes allow an introduction of different lengths of travel for different wavelengths and in this way reverse the gained chirp. After the compression we measured pulse lengths of 140 fs (full width at half maximum) by using an autocorrelation technique.

Optical Parametric Amplifier

The Optical Parametric Amplifier (OPA) is used to generate femtosecond pulses using the output of the RegA with the possibility of a tunable wavelength-range. For an extended wavelength-range two different OPAs from *Coherent* are used, the *OPA 9400* for the visible and the *OPA 9800* for the NIR range. Inside the OPA the beam is split into two beams, to generate a white light spectrum with one beam while the second one is used as the pump-beam, which is either the 800 nm-beam from the RegA or a frequency doubled beam at 400 nm. Optical parametric generation is used between the pump and a specific part of the white light, which results in the amplified signal at the derived wavelength and additionally the idler [18]. Table 3.1.1 shows the available wavelengths for both OPAs. Overall according to company specifications both OPAs give a tunable wavelength-range from 480 nm up to 2400 nm with a gap between 700 nm and 930 nm close to the fundamental 800 nm.

For a more detailed discussion about the OPA only the OPA 9400 will be shown here as the differences between the two models are only a few. In figure 3.1.7 the schematic design of the OPA 9400 is reported. From the left side the 800 nm beam from the RegA (red) enters the OPA and a beam splitter divides it into two beams. One beam with 25% of the energy is used to generate a white light (WL) spectrum. The high pulse energy of the focused beam leads to a further self-focusing effect. This will decrease the spot-size even more and increase the laser intensity to a region where SPM effects become important. These lead to a conversion of the wavelength from the RegA-pulse to a continuum from the UV to the NIR (450-1200 nm). To achieve this the beam is focused into a 3 mm sapphire plate. The generated white-light (light grey in figure 3.1.7) is split for the parametric amplification (80%) and is coupled out of the OPA for direct external use (20%).

	Pump	Signal	Idler
OPA 9400	400 nm	480-700 nm	930-2300 nm
OPA 9800	800 nm	1100-1600 nm	1600-2400 nm

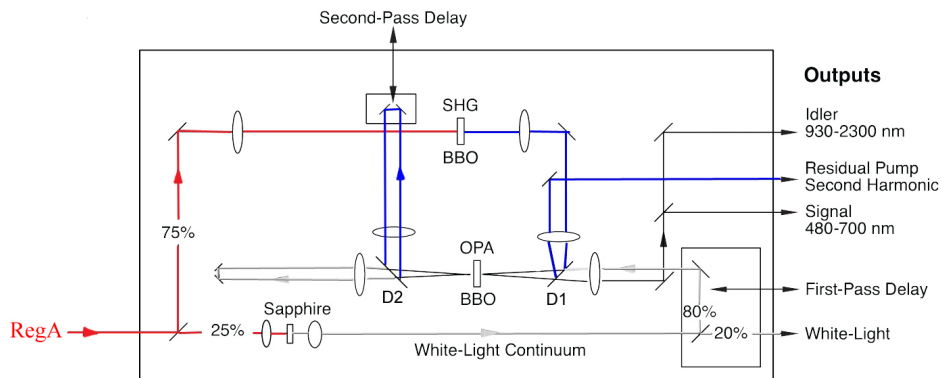***Table 3.1.1:*** *Wavelength range for both OPAs*

Figure 3.1.7: *Schematic design of the OPA 9400*

The second part (75%) of the RegA-beam is used for the second harmonic generation (SHG). For the second harmonic generation two photons will converge in a nonlinear crystal into one photon with doubled frequency $\omega_{SHG} = \omega_1 + \omega_1$. This can be also seen as a special case of the frequency-sum generation. This leads to half the wavelength $\lambda_{SHG} = \frac{1}{2}\lambda_1$ (400 nm). A type I BBO (beta-Barium Borate) crystal is used which has to be out of the focus of the collimating lens before the crystal, or self-focusing inside the crystal would distort the output-beam of the SHG. For an optimal second harmonic generation the crystal can be turned by a micrometre-screw.

The optical parametric generation and amplification is a specific nonlinear process. There are two input beams, the pump (SHG), which is at the lowest frequency and has a high power, and the signal (WL), which is amplified. In this process the pump-photons can be converted to signal-photons. To maintain energy and momentum conservation both incoming waves phases have to be locked together and a third beam, the idler, will be generated. That means the incoming pump-photon is split into a signal and an idler-photon with the energy conservation $E(\lambda_{pump}) = E(\lambda_{signal}) + E(\lambda_{idler})$. While the beams travel through the crystal the pump is constantly decaying and both signal and idler are constantly growing in intensity.

To achieve the phase-matching conditions in the setup the SHG and the white light are combined through the dichroic mirror-path. D1 and the time delay

between both beams can be adjusted by a micrometre-screw which changes the first pass delay for the optical white light . Both beams travel through the crystal with phase-matching conditions. For the conversion the angle of the crystal has to be adjusted by a micrometre screw, as the rotation of the crystal by a few degrees allows to tune the signal and the idler wavelength. After passing the BBO crystal both beams are separated again by D2 and undergo a second pass through the crystal for maximum efficiency of conversion.

After this the beams are separated by dichroic mirrors and the SHG, the signal and the idler are available as the output of the OPA. All OPA outputs are synchronised in the time domain and can be used for time-resolved differential transmission spectroscopy.

3.1.7 Pump-probe spectroscopy

In our experiments a non-degenerate pump-probe setup is used and we have discussed the different outputs of the OPA in figure 3.1.7, that can be used as tunable laser sources for both the pump and the probe-beam. A pump pulse generates a charge-carrier distribution different from the equilibrium in the sample as charge-carriers are excited from the ground state. The excited charge-carrier distribution is probed with a second, temporally shifted, pulse with a comparatively lower photon energy. The decreased charge-carrier population of the ground state leads to a decrease of the absorption as less probe photons resonant with the absorption profile of the material are absorbed. This leads to an increased transmission (bleaching), but excitation from an excited state can be probed as well by choosing a matching photon energy. The differential transmission signal normalised with respect to the transmission in the ground-state is given by

$$\frac{\Delta T}{T_0} = \frac{\Delta T_{exc} - T_0}{T_0} \tag{3.3}$$

with T_{exc} being the probe transmission with pump excitation and T_0 without pump.The transmission spectrum $\frac{\Delta T(\lambda)}{T_0}$ can be either obtained by changing the

probe wavelength and reconstructing a spectrum point by point or by using a broadband source for the probe with subsequent spectral filtering.

Figure 3.1.8 illustrates a generic pump probe setup with the pump- and probe-beam overlapping on the sample, while the intensity of the probe beam is measured with the detector. The temporal shift between both pulses is created by the translation of two mirrors in the probe path. In this work a high-precision linear translation stage from Physik Instrumente (M-521DD) is used to generate the temporal delay together with a hollow retroreflector ensuring to reflect the beam parallel to the incident beam without distortion and minimal change in position and shape of the beam. To verify the beam position and shape during the movement of the translation stage, a beam profiling camera (WinCamD-UCD12-1310) from DataRay Inc. is used giving an accuracy of $1\,\mu m$. For detecting the intensity of the probe beam balanced photo diodes are used. A silicon photo-diode (Newport 2307) is used covering the visible light from 400-1050 nm while a Germanium photo-diode (Newport 2317NF) is used for longer wavelengths covering 800-1700 nm with a bandwidth of 1 MHz and 150 KHz respectively. For typical pump-probe measurements changes in the transmission of the order of 10^{-4} have often to be detected with a noise that is often of the same order of magnitude. To be able to detect such small signal changes the signal-to-noise ratio (SNR) has to be strongly increased. We use a lock-in amplifier together with a periodically modulation of the pump beam. For the modulation either an optical phase-locked chopper (Newport
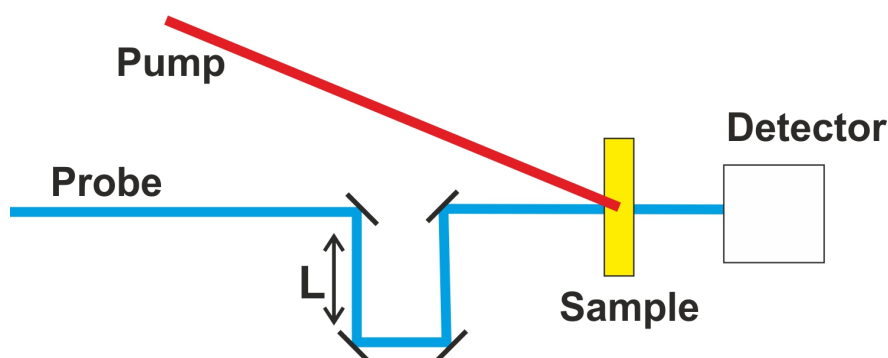

***Figure 3.1.8:** Principle of pump-probe measurements*

3501) or an AOM is used. For the optical chopper the maximal phase-locked chopping frequency is 10.65 KHz and the RegA reference output is used as a sub-harmonic trigger signal. This leads for a repetition rate of 250 KHz to a train of 25 pulses that are blocked or transmitted alternating. A second approach to modulate the signal is by using an (AOM), driven by half of the RegA reference signal to block every second incoming laser pulse. Two different AOMs from Brimrose are used (TEM-110-18-400 and TEM-110-18-800) for the 400 nm and 800 nm pump beam. Either the chopper or the AOM signal is used as a reference signal for a lock-in amplifier, that is only detecting the signal at the reference frequency band. A HF2LI digital lock-in amplifier from Zurich Instruments was used, consisting of two physical, allowing detecting both at the repetition frequency as well as the modulating frequency with just one device.

3.2 Materials and preparation

3.2.1 Organic crystals

All solvents used have been supplied by *Sigma-Aldrich* with a purity of 99 % or higher. For the preparation of conjugated polymer films following materials are used:

- **PCDTBT** (Poly[N-9′-heptadecanyl-2,7-carbazole-alt-5,5-(4′,7′-di-2-thienyl-2′,1′,3′-benzothiadiazole)], Poly[[9-(1-octylnonyl)-9H-carbazole-2,7-diyl]-2,5-thiophenediyl-2,1,3-benzothiadiazole-4,7-diyl-2,5-thiophenediyl]) was supplied by *Sigma-Aldrich*. Th structural formula of the repeating unit is illustrated in figure 3.2.1 (a).

- **PCBM[60]** ([6,6]-phenyl-C61 butyric acid methyl ester) was supplied by *Solenne BV* with a purity of >99.5 %. The structural formula is illustrated in figure 3.2.1 (b).

The fullerene derivate PCBM[60] is a widely used standard acceptor material for organic photovoltaics, while PCDTBT is used as a donor material for the same applications.
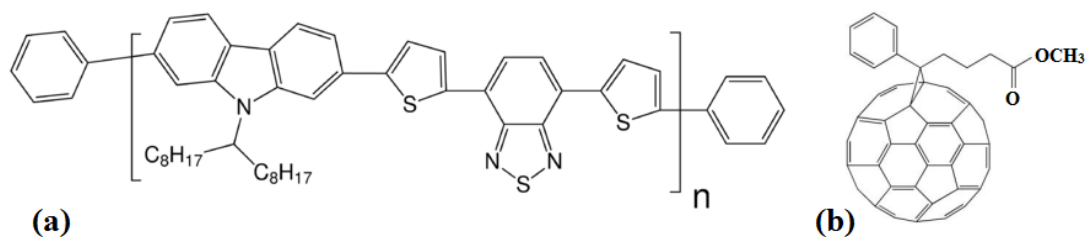
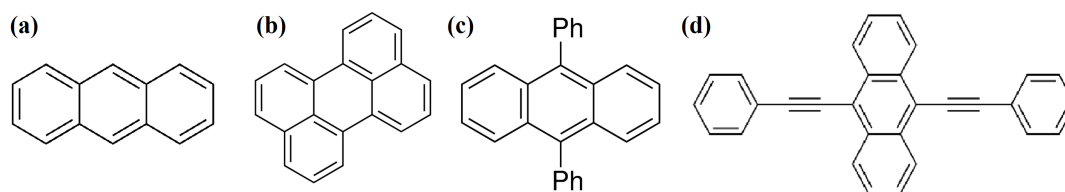***Figure 3.2.1:*** *Structural formula of (a) PCDTBT [112] and (b) PCBM[60] [113]*

Figure 3.2.2: *Structural formula of (a) Anthracene, (b) Perylene, (c) DPA and (d) BPA*

For experiments on the hybrid fibre growth different materials have been explored, that all purely consist of carbon and hydrogen and are based on the structure of benzene rings. Starting with Anthracene consisting of three benzene-rings, the size and molecular weight increases to Perylene, 9,10-Diphenyl-anthracene (DPA) and 9,10-Bis(phenylethynyl)anthracene (BPA) is the biggest used molecule. All materials have been supplied by Sigma-Aldrich and the structural formulas can be seen in figure 3.2.2. Together with the size also the delocalisation of π-electrons is increased and changes important optical properties. Table 3.2.1 gives an overview of the used materials together with some important physical properties for our experiments.

3.2.2 Glove box

To protect oxygen or water sensitive materials from degradation a glove box is used for storing as well as for preparing materials. It is build by *Glove Box Technology Ltd.* and is used with oxygen-free nitrogen cylinders to create an inert atmosphere. A carbon trap is used to filter solvents out of the atmosphere inside the glove box together with molecular sieves to keep both the oxygen and moisture level below 3 ppm. To transfer materials into or out

	Anthracene	Perylene	DPA	BPA
Sum formula	$C_{14}H_{10}$	$C_{20}H_{12}$	$C_{26}H_{18}$	$C_{30}H_{18}$
Purity	99 %	99 %	97 %	97 %
Molecular weight	178.23	252.31	330.42	378.46
Melting point	210-215 °C	276-279 °C	245-248 °C	248-250 °C
Boiling point	340 °C	443 °C	485 °C	-
Vapour pressure	$2 \cdot 10^{-8}$	0.0001	$2 \cdot 10^{-8}$	-
Refractive index (at 700 nm)	1.59	1.7	1.65	-

of the glove box an ante-chamber is used with a programme that does three cycles of evacuating the ante-chamber followed by a nitrogen purge. Pressure inside the glove box is automatically regulated to stay within the limits by applying pressure from the nitrogen cylinder or vacuum from a rotary pump continuously running.

The glove box is equipped with a Laurell WS-400B-6NPP-LITE spin-coater that allows to produce thin-films in inert atmosphere with a high accuracy in layer thickness.

3.2.3 Fibre drawing tower

For the fabrication of the optical fibres the microscopic structure is first created in a macroscopic preform. In a fibre drawing tower these are drawn to the desired microscopic dimensions while keeping the macroscopically created structure. In figure 3.2.3 the whole process of stacking and drawing is illustrated. In the first step silica glass tubes are drawn into capillaries (a) that can be stacked in a second step. During the stacking process the microscopic structure is created by inserting the desired structures like the core into the stack of capillaries. The stack is inserted into a glass tube (jacketed stack (b)).
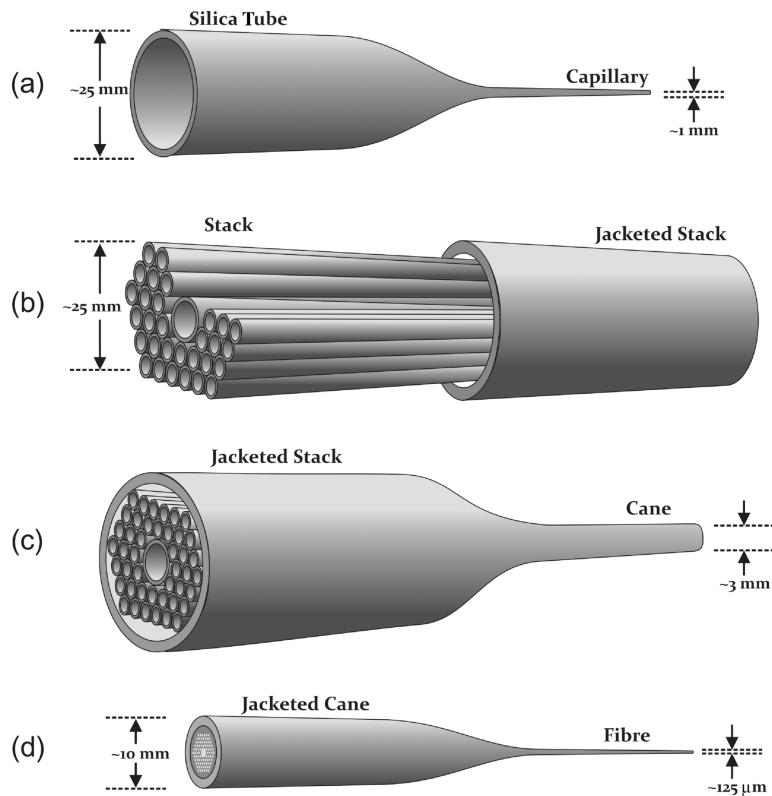
Figure 3.2.3: *Overview of the stack-and-draw technique: (a) drawing of capillaries, (b) stack of capillaries, (c) jacketed stack is drawn to canes and (d) canes are drawn into fibres [114]*

The jacketed stack is drawn down to the cane or preform (c) in the drawing tower and in a final step drawn into the fibre (d). Pressurising holes during the last drawing step allows holes to be inflated or collapsed and gives another possibility of controlling the fibre structure, that is especially needed for the fabrication of the used hollow core fibres.

3.2.4 Hybrid fibre growth and preparation

For the crystal growth inside hollow core fibres silica fibres have been used with different diameters of the hollow core. The smallest diameter of the core was below 1 µm, while larger core diameters were used at 9 µm, 13.5 µm and 16 µm. The overall cladding diameter was kept constant at 125 µm for all fibres

used. The structure of an exemplary fibre can be seen in figure 3.2.4 with the hollow core in the middle surrounded by the concentric, uniform cladding.
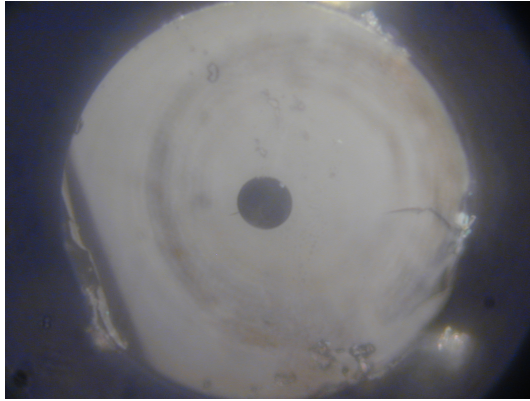

Figure 3.2.4: Microscope picture of the cross-section of a 16 µm core fibre.

For the preparation the fibre coating has been stripped using a razor blade and fibres have been cut to a length of 20 cm using a *Thorlabs Fiber Scribe*. The glass reservoir is cleaned in a ultrasonic bath using deionised water, 2-propanol and acetone to avoid unwanted charges on the glass. a The prepared fibres are attached to the glass reservoir by using either high temperature sealant or fire cement. The high temperature sealant *Silcoset 158 Black Silicone Sealant Paste for Bonding* from *Acc Silicones* is temperature resistant up to 300 °C and shows good physical and chemical stability. For higher temperatures *VITCAS Premium Fire Cement* was used, being stable for temperatures up to 1250 °C. Being smoke and gas tight, the fire cement matches all requirements, but has shown to be harder to be processed than the sealant.

The glass reservoirs have been produced by a glass blower to our desired specifications from borosilicate glass tubes. A detailed explanation follows in chapter 5.1.
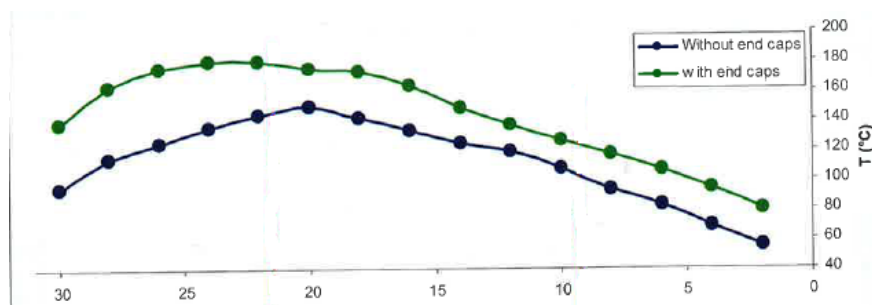
Figure 3.2.5: Measured temperature profile of the furnace for 170 °C and 110 °C with and without sealing of the tube

The furnace used for the fibre filling and growth is a tube furnace from *Lenton*. The model *LTF12-38-250* has a maximal temperature of 1200 °C, an inside tube diameter of 38 mm and a heated tube length of 250 mm. We have used a two-zone furnace, consisting of two independent temperature controls and heating elements. A typical measured temperature profile for the settings of 170 °C and 110 °C is shown in figure 3.2.5. Because of the strong influence of sealing the ends of tube, especially for a vertical setup, all experiments have been carried out with sealed ends.

4 Development of an ultrafast spectroscopy setup utilizing ZBLAN fibre

In this chapter first the planning and building of a setup for ultrafast pump probe spectroscopy will be covered in section 4.1. Subsequent the data acquisition in analysis for the newly built setup is explained in section 4.2. After the conventional setup has been introduced we show the generation and characterisation of a supercontinuum in a ZBLAN fibre in section 4.3.2 and 4.3 to finally use the generated SC as a broadband probe source for the pump probe setup in section 4.4.

4.1 Design of the pump-probe setup

In section 3.1.6 and 3.1.7 the used laser system in our laboratory and the principle of a transient absorption setup have been discussed. Part of this work was to plan, realise and optimise such a setup. The temporal pulse shape is the ultimate limiting factor for the temporal resolution, for this reason one of the goals was to maintain a short pulse as possible. Another important point is to increase the SNR to make small signal changes possible to be detected. Finally simplifying the handling of the setup and allowing to decrease time needed for alignment of the setup was considered.

The conventional layout for the setup uses the the residual pump beam of the OPA as the pump, either at 400 nm or at 800 nm for the visible and infrared OPA. The tunable signal output of the OPA is used for probing the sample. In
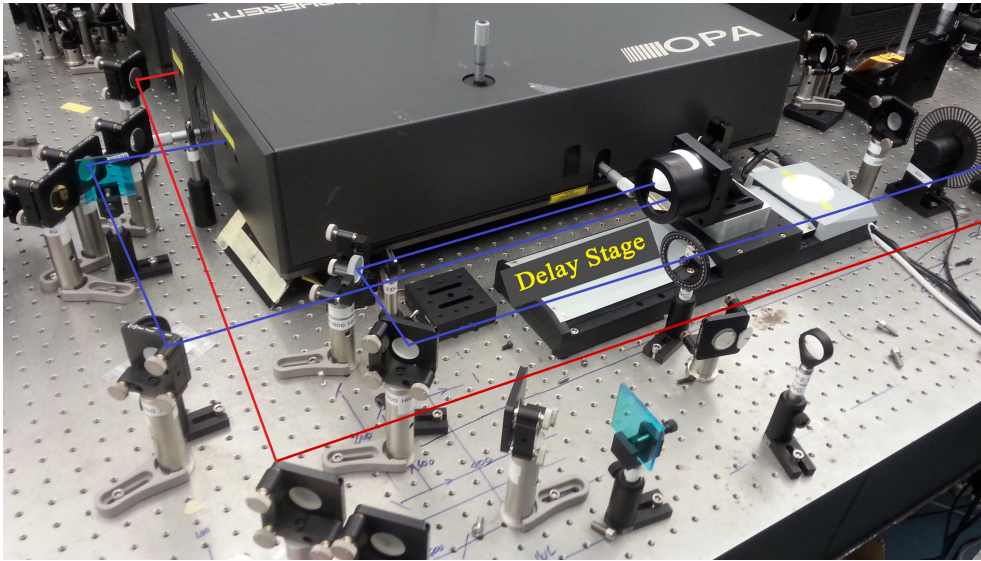
Figure 4.1.1: *OPA outputs and translation stage used for the pump-probe setup. The pump beam is illustrated in blue, the probe beam in red.*

all experiments speciality dual band 400 nm and 800 nm dielectric mirrors are used for the probe beam, while for the visible experiments silver mirrors and for infrared experiments golds mirrors are used in order to have low losses and distortion. The optical path-lengths are kept short and the amount of mirrors and especially lenses has to be kept low.

Figure 4.1.1 shows a picture of the laser outputs used in the visible pump-probe setup. The probe beam (red) is directly reflected to the sample area on the right side, while the 400 nm pump beam (blue) is send to the retroreflector mounted on the translation stage. The pump beam is send through the translation stage, as it is less sensitive to small perturbations in comparison the probe beam.

The pump beam can be less focused less tightly on the sample, illuminating a bigger sample area than the area probed, guaranteeing the probe beam to be a homogeneously pumped area even with small beam shifts during the move of the translation stage. The beam profiler is used to characterise both pump and probe beam. Figure 4.1.2 shows an example of the intensity profile of the probe beam. The focus is used to align the spot diameter of the probe to about 45 μm, while the pump beam diameter is set to about 200 μm. The beam
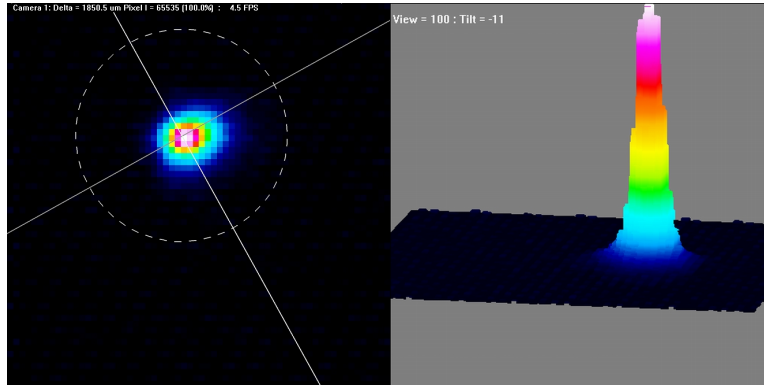
*Figure 4.1.2:* Beam Profile of the probe beam in 2d and 3d visualisation

profiler is used to align the pump beam passing through the translation stage. It is crucial for the accuracy of the measurements that during the movement of the translation stage the pump laser position on the sample does not change because of a change in the pump beam [18]. With the beam profiler it is possible to optimise the alignment and guarantee the invariance of the beam shape and position.

The translation stage is used to create and control the temporal delay between pump and probe pulse. The used translation stage has a total travel range of 204 mm, giving a maximal temporal delay between pump and probe pulse of

$$\Delta t = \frac{x}{c} = \frac{2 \cdot 204\,\text{mm}}{2.99 \cdot 10^8\,\frac{\text{m}}{\text{s}}} = 1365\,\text{ps}$$

The demands for the translation stage are high, as the accuracy of the movement can decrease the temporal resolution, and any deflection of the beam while the stage is moving will create errors in the measurement. The first important point is a high flatness of the stage which is given by 1 µm per 100 mm with a low pitch/yaw.

For high travel accuracy linear guides with recirculating ball bearings are used. The stage is driven by a DC motor with integrated active-drive amplifiers which allow also high velocities up to 50 mm/s. A directly measuring linear encoder is used for accurate positioning and repeatability and gives
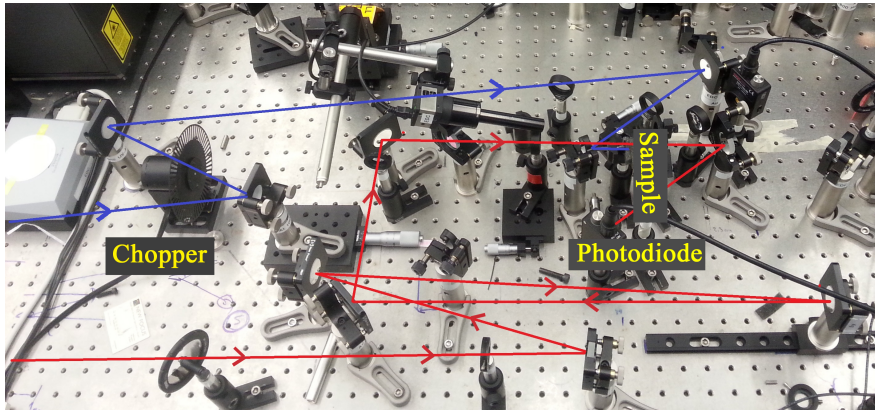
Figure 4.1.3: *Sample area of the pump-probe setup with pump beam in blue and probe beam in red*

the possibility to read the exact position at every time of the measurement. Overall this gives us a sensor resolution of 0.02 µm which corresponds to a temporal accuracy of 0.07 fs, which is far below the temporal length of the used laser pulses. The repeatability is given with 0.1 mm which corresponds 0.33 ps, and can still be decreased by lowering the movement velocity, as from the beginning of a measurement only relative steps are made in one direction. The controller for the stage is a PCI card which allows direct access to the translation stage through the computer.

For the parallel beam reflection on the delay stage a retroreflector from Edmund Optics is used. It consists of three flat mirrors assembled in a corner cube and reflects the beam parallel to the incoming beam, mostly insensitive to the position and angle of the incoming beam. By using mirrors instead of a prism based corner cube, chromatical aberration is eliminated and distortion of the beam's temporal profile is minimized. The accuracy of the parallelism of the reflected beam is given by 2 arcsec.

Figure 4.1.3 shows the sample area of the pump-probe setup. The probe beam is modulated by the optical chopper, using UV-enhanced concave aluminium mirrors to create a focused beam to pass the chopper. The probe beam is undergoing a more complicated beam path to compensate the optical path length difference to the pump beam. Both beams are focused onto the sample in a nearly collinear configuration by using a D-shaped mirror. To obtain a

coarse spatial overlap a CCD-camera is used that allows to view and resolution of both beams on the sample. The working distance with the used objective is at 94 mm and the field of view is 6 mm, which gives a good view of both beams for overlapping them on the sample. Before performing an experiment a temporal overlap of the two pulses needs to be achieved while the beams are spatially overlapped with the help of the camera. Temporal and spatial overlap corresponds to a signal detected on the lock-in amplifier. The detected signal intensity is used to do a fine alignment of the spatial overlap of both beams.

With the optical chopper the maximum modulation frequency for the pump beam is 10 KHz. With a laser repetition rate of 250 KHz a train of 25 pulses will be transmitted and blocked alternating. To benefit from the high repetition rate of the laser by working at high frequency and thus low noise, another modification was used. Instead of the optical chopper an acousto-optic modulator is used that allows to diffract the laser beam by the use of acoustic sound waves inside a crystal. The main laser beam is blocked by an iris while only the beam diffracted at the modulation frequency passes through. It is driven with half the laser repetition rate, transmitting every second laser pulse.

The experimental setup discussed so far uses the tunable signal output of the OPA as a probe beam. To record a full spectrum, the OPA has to be tuned to different signal-wavelengths for every measuring point. This leads to a lot of alignment work both for the OPA and for the overlap of the pump and probe beams for every single measurement point.

A faster method utilises a broadband light source for the probe beam together with spectral filtering. The simplest way used was by transmitting the probe beam through a bandpass filters of the wanted wavelength in front of the detector. This gives a fast way to execute, as the bandpass filter is simply inserted into the beam path. The downside is the selectable wavelengths being limited by the amount of available bandpass filters. A more flexible setup was explored using linear variable filters with an example shown in figure 4.1.4. A combination of a high-pass and low-pass filters creates a bandpass filter with the width being tunable by translating both filters with respect to each other and the centre wavelength being selected by a translation of both

filters together. In this case a calibration is needed for accurate measurements, but great flexibility is offered for the selection of wavelengths. Finally a grating based monochromator was used for spectral filtering, gaining good monochromating properties, but typically lower light throughput.

4.2 Data Analysis with the HF2LI Lock-in Amplifier

As mentioned above, often differential signals have to be detected that are of the order of 10^{-4} - 10^{-5}. This makes it important to increase the SNR as far as possible, but experimentally the pump/probe power cannot be increased without limits due to damages of the sample and different induced effects at higher intensities. For that reason the data analysis and the signal processing becomes an important part of the experiment. A lock-in amplifier is used to filter the differential signal ΔI out of the intensity signal detected by the photo diode including background and noise. The decision for a lock-in amplifier fell on the *HF2LI* from *ZurichInstruments* because of several advantages. It is a digital lock-in amplifier, completely controlled through a computer, removing all the buttons and controls from the device itself. This allows a much easier integration of the data analysis through a *LabVIEW* program as well as the possibility to control the whole lock-in amplifier through the software on the computer instead of having to change properties on the device itself.
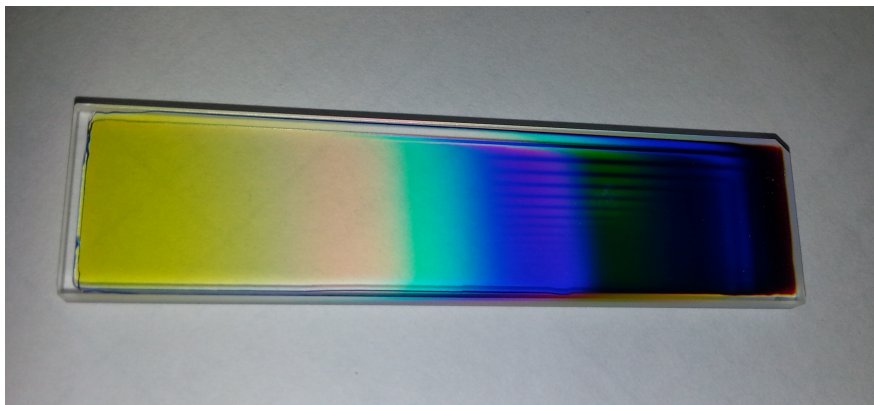

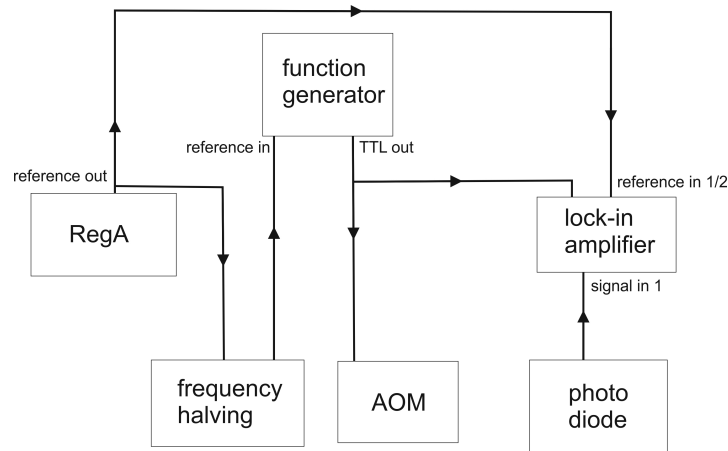*Figure 4.1.4: A linear variable edge filter*

Figure 4.2.1: Diagram of the wiring for signal processing

Another problem arises from the fact that the lock-in amplifier has to detect the signal at two different frequencies for this setup, at the laser repetition rate to detect T_0 and at the modulating frequency ΔT. The *HF2LI* with the multi-frequency option offers the possibility to detect two separate input signals at different reference frequencies each at the same time with only one device instead of using two lock-in amplifier in tandem configuration. Consisting of two physical lock-in units, the signal from the photo diode can be detected at both frequencies using only one lock-in amplifier.

Figure 4.2.1 shows a diagram of the wiring used for the pump-probe setup and data analysis using the AOM for modulation. As a basic reference signal the *reference out* of the RegA is used. This is directly sent to the lock-in amplifier as *reference 1*, allowing to detect the ground state transmittance T_0. Further the RegA *reference out* is used to drive the AOM. For that the signal is first send to a house-build frequency halving device. This signal, now containing only every second pulse is used again as a reference for a function generator. A TTL signal synchronised to every second laser pulse, is generated to drive the AOM with an appropriate voltage as well as being send to the lock-in amplifier as *reference 2*, allowing to detect the pump induced transmission change ΔT at the AOM modulation frequency.

Considering the signal modulation from the frequency domain, we can think of the RegA repetition frequency ω_{RegA} as the carrier frequency with a
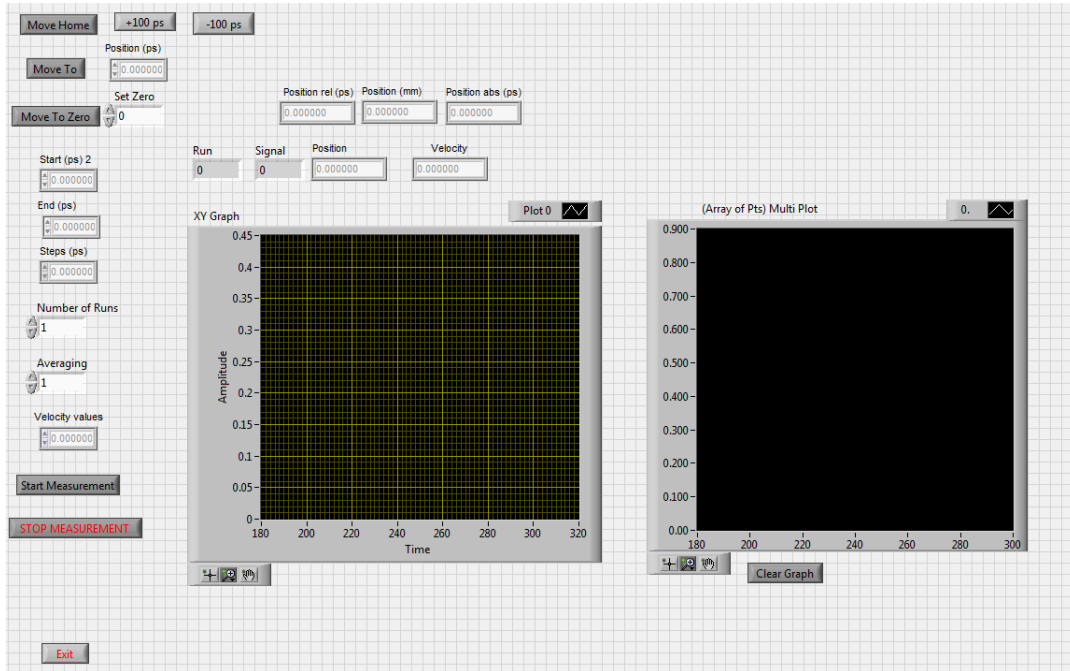
Figure 4.2.2: LabVIEW programme controlling the pump-probe setup

modulation frequency ω_{mod} coming from the AOM. In this case sidebands will be created at new frequencies $\omega_{+,-} = \omega_{RegA} \pm \omega_{mod}$. The *HF2LI* is used in this work with the multi-frequency and and the AM/FM modulation add-ons. This allows a direct demodulation of both sidebands rather then detecting just at the modulation frequency. With both sidebands being demodulated independently also asymmetries are taken into account. In comparison to a tandem demodulation by using ω_+ and ω_- the SNR can be improved by a factor of $\sqrt{2}$ [115], while still keeping the phase information.

Finally the *HF2LI* offers good implementation possibilities, offering various application programming interfaces. For controlling the pump-probe setup a *LabVIEW* programme has been written, with *LabVIEW* offering good possibilities to create visual interfaces. The aim was to include all needed functionalities and control as much as possible through the computer, simplifying the use of the setup. The programme is controlling both the translation stage and the lock-in amplifier. The buttons at the top move the translation stage to the absolute zero position (Move home), to a selected point on a ps scale

(Move to), to the chosen zero point (Move to zero), that can be used to shift the rise point of the signal, and in relative steps of 100 ps ($\pm$ 100 ps).

For each measurement the starting and ending point can be set in ps together with the distance between measuring points (steps). Increasing the number let the software do a whole measurement from start to end point and repeat the measurement according to the number of runs. Averaging on the other hand will do all measurements at one time delay before moving the translation stage to the next point. Averaging gives a better SNR while increasing the number of runs helps to see stability problems of the sample. Finally the velocity of the translation stage can be changed, if a higher accuracy is needed for small steps.

The left graphical interface shows the current measurement in a real time view, while the right one plots all finished graphs together, giving an overview and comparison of different measurements or samples. During the measurement different indicators show current values for the signal, position, velocity and number of run. After finishing a measurement the programme asks automatically to save the averaged data in a file with comma separated values (.csv).

4.3 ZBLAN fibre for generating the infrared supercontinuum source as a probe

In chapter 4.1 we have discussed the possibility to use a broadband light source in combination with spectral filtering for the probe beam. For wavelengths in the region of visible light this can be realised in a simple way, as many supercontinuum sources are available for this spectral regime [116]. In our case the white light output from the OPA generated in a sapphire plate can be used. Conducting experiments at longer wavelength one will find the problem of a lack of supercontinuum sources in bulk media, unless high power laser systems are used [117]. For this reason many experiments are carried out using nonlinear optical conversion which has to be tuned for every probe wavelength.

In this work a new approach was realised for a system using a supercontinuum light source with possibilities for extension to longer wavelength [118].

In order to efficiently use a generated supercontinuum for pump probe spectroscopy a series of properties have to be considered that affect the spectroscopic measurements.

Pump intensity In order to avoid using only high power laser systems which typically offer lower repetition rates and are more expansive, generating a SC with lower pump intensities is preferable.

Spectral range The needed spectral range for pump probe measurements mainly depends on the phenomena to be investigated. To make the maximum possible flexibility available to investigate different physical effects and materials a very broad SC is favourable, that can extend both further into the UV and/or the IR.

Pulse length The pulse length of the probe pulse is one of the ultimate limiting factors for the temporal resolution of a pump probe measurement. In the first place the pulse length is limited by the pulsed laser source, which often is not the broadband source itself. During the SC generation process the pulse should be broadened as little as possible in the temporal regime, so temporal resolution is not lost by using a broadband source.

Ouput intensity For a good SNR a higher amount of photons is desirable. For that reason a high SC output power helps to measure a stronger signal. A more efficient SC generation process is therefore increasing the available output power.

Chirp A chirp in the broadband probe pulse will lead to light at different wavelengths arriving at different points in time. Without any extra compensation this introduces artefacts in the measurements, showing wrong time dynamics between different spectral components.

Flat spectrum The ideal probe spectrum shows a very flat spectrum over most of the wavelength range. This will provide comparable probing

over the whole available spectrum without the need to readjust the probe power.

Pulse-to-pulse stability A broadband source with little intensity changes from pulse to pulse is important to avoid intensity fluctuations over time during a measurement, increasing both the accuracy and reproducibility.

Simple alignment process While before mentioned technical properties limit the possible applications, for working with such a setup, one is interested in finding an easy and fast alignment process, making it unnecessary to spend a lot of time on aligning the broad band source each day.

It is possible to generate a supercontinuum in many different materials, as long as one can achieve a pump power high enough to access the nonlinear properties of the specific material. But at the same time the material has to withstand the high light intensities to be efficiently used. In practical use a couple of methods and materials are widely used to generate supercontinua. One way is to use a bulk solid material like fused silica, sapphire or yttrium aluminium garnet (YAG). For these materials usually a laser with short pulses and high peak power is strongly focused into the material, to achieve high light intensities. We have seen in section 2.3.4 that the product of the intensity and the interaction length gives a measure for the nonlinear efficiency. For a bulk material this efficiency cannot be increased by increasing the focus as it leads to a reduction of the interaction length at the same time. On the other hand when using optical fibres the interaction length is given by the fibre length, while the light intensity is proportional to the fibre core size, which gives the opportunity to change the nonlinear efficiency by choosing the fibre geometry.

As a result we can see that optical fibres offer a efficient possibility to generate supercontinua with low pulse powers in comparison to bulk materials. Following from this it is obvious that optical fibres can be a great choice if only a limited pump power is available as the length of the fibre can easily be increased. On the other hand this means as a downside that the length over which a light pulse experiences dispersion in the fibre is increased at the

same time. If a short pulse length and with that the temporal resolution of pump probe measurements is of big interest, limitations to the fibre lengths are imposed.

Depending on the processes to be investigated it is important to have the matching pump and probe spectrum available to observe the processes of interest. As the according needed wavelengths are dictated by the physics of the studied material, the right supercontinuum and material for generating the supercontinuum has to be chosen. In the first place the pump laser wavelength is important, as this gives the origin where the spectral broadening starts. For an efficient spectral broadening to happen, we must be in a regime where the used material offers a very high transmittance and low losses. This gives limitations to the material according to the specific transmission window together with scattering effects in the transmission window. Besides of this limitation the available nonlinear efficiency will strongly affect the output spectrum, as a higher efficiency leads to a wider spectrum.

For investigating a wide range of organic conjugated materials, many interesting optical transitions can be found in the NIR to MIR region. From the so far discussed points and the aim for extending the output spectrum to the NIR to MIR our choice falls onto the optical fibres for the reason of the lower needed pump power. Besides of needing less pump power, offering a wider output spectrum at a comparable pump power, also the output intensity increases. Optical fibres can be made out of various different glasses. We have discussed the transmittance of silica glass in section 2.2, which limits applications for wavelength extending to the MIR [119]. ZBLAN is a good material from the group of the halide glasses to draw fibres because of its stability for fibre drawing and applications. The nonlinear coefficient of ZBLAN allows to generate a supercontinuum without microstructuring of the fibre [30] and the transmittance can reach up to wavelengths higher than 8000 nm, if the right parameters are chosen [120]. Recently there has been a lot of interest in the research of supercontinuum generation in ZBLAN fibres in the MIR with a focus on high power laser sources [121], [33]. Typically these high power lasers have low repetition rates but for pump-probe experiments high repetition rates are desirable to increase the SNR.

In order to keep the temporal output pulse length in an acceptable range, it is important to keep the used ZBLAN fibre short, while maintaining a balance with the generated spectral broadening. In general two different regimes can be observed for the supercontinuum generation in the optical fibre, a SPM dominated regime and a soliton dominated regime. While the SPM dominated regime exhibits a stronger pulse widening in comparison, the soliton regime can keep the pulses much shorter. On the other hand due to the soliton fission, fundamental solitons are ejected at different times and therefore experiencing various optical effects over varying timescales. Ultimately this leads to a chirp that will be introduced into the pulse according to solitons being ejected from a higher order soliton at different times. Although this introduces an additional chirp on the long wavelength side in the soltion regime, this chirp can be compensated through data manipulation, if the chirp is known from simulations of the supercontinuum. It should further be mentioned here that the generation in the soliton regime comes with the cost of a higher pulse-to-pulse instability [122].

A different approach instead of using a broadband light source is using a tunable light source. Instead of creating a supercontinuum, nonlinear processes like parametric amplification and sum and difference frequency generation can be used to generate laser pulses with the exactly wanted wavelength. Although
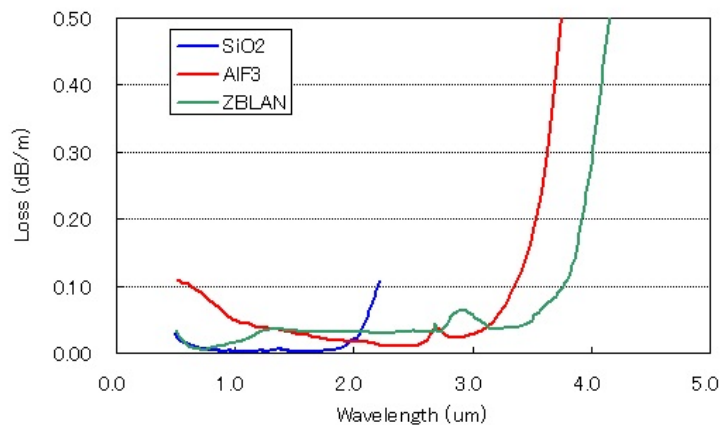
Figure 4.3.1: *Loss spectra for of ZBLAN fibre in comparison to other fibres from the ZBLAN fibre supplier [123]*

the quality of laser pulses generated in this way is good, much more time has to be spend on alignment procedures, as phase matching has to be achieved for these nonlinear processes. To record a full spectrum for one measurement the alignment has to be changed to generate every single wanted wavelength of light.

Considering all disadvantages and advantages we have decided to use a ZBLAN fibre to be optical pumped because of the nonlinear efficiency, the potential for the spectral range with the big transmission window of ZBLAN glass together with the possibility to compensate for the introduced chirp by simulations and data processing. Figure 4.3.1 shows the typical transmission window for a ZBLAN fibre as it was used in the following experiments.

In this chapter we explore the possibility to utilise a commercially available ZBLAN step-index fibre to create a probe supercontinuum. First the type of fibre and the pumping wavelength are explored, the generated supercontinuum will be characterised and at the end of this chapter we demonstrate NIR pump-probe spectroscopy using the ZBLAN fibre.

4.3.1 Dispersion of the ZBLAN fibre for supercontinuum generation

The ZBLAN fibres used for these experiments have been bought from *FiberLabs Inc.*. Two different models have been used and studied, the $ZSF - 6/125 - N - 0.20$ and $ZSF - 9/125 - N - 0.20$. Both fibres are step-index with a cladding diameter of 123 µm and a core diameter of 6 µm and 9 µm respectively.

As a first investigation the dispersion of the fibres has to be understood. For that we are measuring the GVD parameter D experimentally. In figure 4.3.2 the experimentally determined D is plotted for the $ZSF - 6/125 - N - 0.20$ fibre with red dots. The wavelength range experimentally available was limited by the detector and bandpass filters at the long wavelength side at 1750 nm. We can see from the plot that all measurement points are clearly in the normal dispersion regime showing negative values for D. For efficient supercontinuum generation we are interested in the zero dispersion point (see section 2.3.4, that was not inside the experimentally available range.
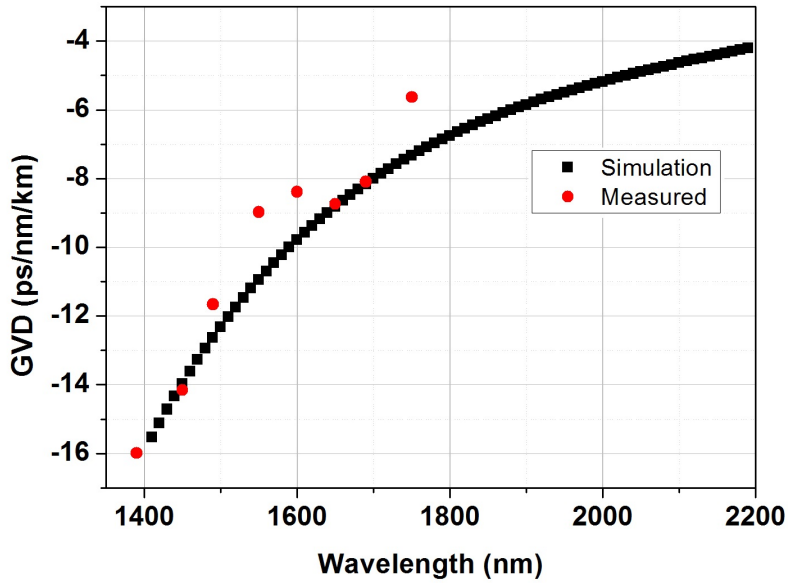
Figure 4.3.2: *Measured (red) and calculated(black) GVD parameter D for a 6 μm diameter core ZBLAN fibre.*

To gain a better estimation we have used the Sellmeier equation (equation 2.20) to calculate the ZBLAN material dispersion. The numerical solution of equation 2.21 gives the propagation parameter β and the dispersion can be calculated by differentiation of β. The overall fibre dispersion can be simulated using both equation 2.20 and 2.21 and is compared to the experimental results. For the calculation the fibre parameters provided by *FiberLabs Inc.* are used (refractive index, numerical aperture, core diameter) together with typical literature values [31].

In figure 4.3.2 the calculated dispersion is shown in black, and reveals a good fit to the experimental data. Small deviations can be understood by considering that ZBLAN is a composite glass and can vary in its composition and for that reason coefficients may have small variations. Another reason for small uncertainties is being in the multi-mode regime as λ_{cutoff} is given with 2600 nm. Keeping in mind the potential output wavelengths of the used OPA shown in table 3.1.1 the dispersion is only plotted up to 2200 nm. The calculated value of D is still -4 at this wavelength, not making the zero dispersion available for output photon energies of the OPA.
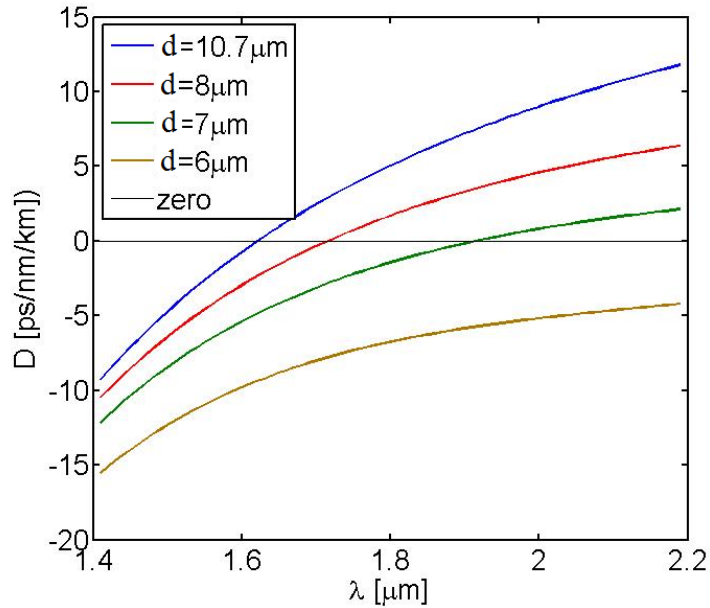
Figure 4.3.3: *Calculated dispersion for different core diameters d of the ZBLAN fibre*

Using the calculation results from the 6 μm core fibre, by gradually increasing the core diameter d a comparison over different fibre geometries was simulated. Figure 4.3.3 shows the computed values for D, and indicates a strong shift of the zero dispersion wavelength of the fibre to shorter wavelengths for increasing core diameter. For the $ZSF - 6/125 - N - 0.20$ fibre the calculated zero dispersion was around 2800 nm, while for larger cores it can be shifted down to 1600 nm.

According to this calculations a second fibre was chosen with a 9 μ core diameter. All other parameters are kept the same and the analysis of the fibre is carried out in the same way. Figure 4.3.4 shows the experimental and theoretical values for the GVD parameter for this fibre. The experimental data confirms the zero dispersion wavelength being between 1600 nm and 1700 nm as predicted. The calculated values match the experimental data well and give a value for λ_o of 1650 nm.

In figure 4.3.5 the output power/energy of an OPA of the same configuration is plotted. The RegA pumping the OPA for this figure has shorter pulses and a higher output power, leading to higher powers in this figure compared to
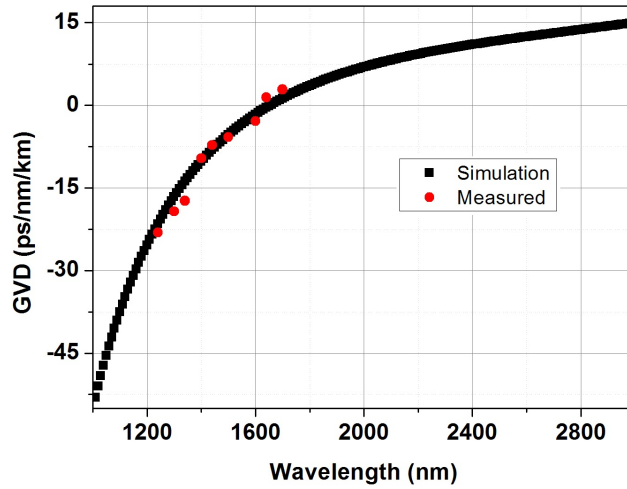
Figure 4.3.4: *Measured (red) and calculation (black) GVD parameter D for a 9 μm diameter core ZBLAN fibre.*
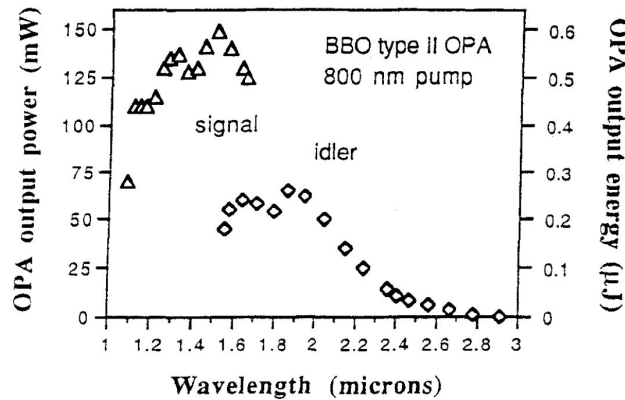

Figure 4.3.5: *Energy outputs of a Coherent OPA 9800 pumped by a 100fs RegA [124]*

the OPA used for our experiments, but qualitatively the output is similar. In general the signal output has a higher average power than the idler output, with decreasing power at both ends of the tunable spectrum. Comparing the energy output of the OPA with the dispersion of our fibre suggests to pump the fibre below the zero dispersion, to use the higher power output of the OPA. Empirically we found that the best compromise between the power spectrum of the OPA and the dispersion of the fibre is at 1550 nm in order to generate a broad supercontinuum.
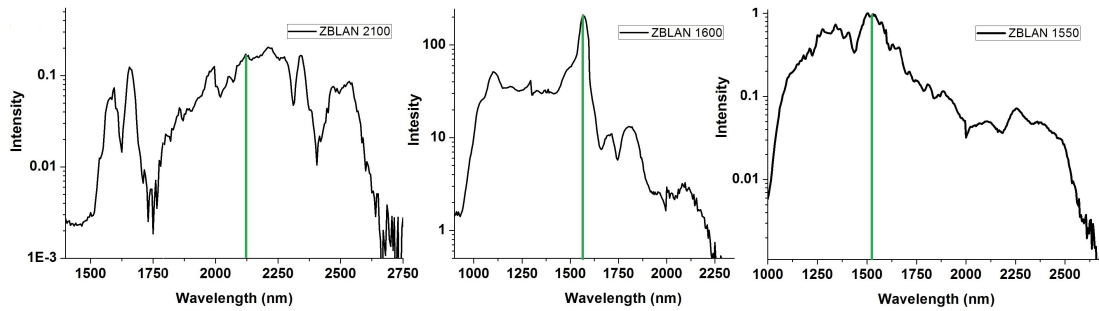
Figure 4.3.6: *Supercontinuum generated in a 3.5 cm long piece of ZBLAN fibre with 9 μm core diameter pumped at different wavelength and plotted with a logarithmic scale. The pump wavelength is indicated with a green vertical line at (a) 2100 nm, (b) 1600 nm and (c) 1550 nm.*

4.3.2 Analysis of the supercontinuum

The experiments for generating a supercontinuum with the ZBLAN fibre were carried out using either the signal or idler output of the IR OPA. For coupling into the ZBLAN fibre 3 axis flexure stages with differential adjusters were used. For the efficient supercontinuum generation with respect to extend the longer wavelength side different pumping wavelengths have been explored. From figure 4.3.5 one can notice that the power output of the OPA peaks at around 1500 nm. As the peak power is high and the wavelength is relatively close to the zero dispersion, a broad supercontinuum can be expected. To shift the continuum to longer wavelengths also longer pump wavelength using the idler output have been explored.

Efficient supercontinuum generation has been shown from pieces of ZBLAN fibre with a length of a couple of centimetres [32]. A supercontinuum extending supercontinuum into the MIR has been shown with the reduced fibre length due to a reduction of the confinement loss for longer wavelengths with the reduced travelling length [32]. For this work a fibre length of 3.5 cm has been chosen in order to keep the temporal widening of the pulse low due to dispersion effects dependent on the fibre length.

Figure 4.3.6 shows three output spectra of pump light guided through a 9 μm core ZBLAN fibre. The fibre has been pumped at different wavelength, using the OPA idler for figure 4.3.6 (a) and the OPA signal for figure 4.3.6 (b) and (c). In figure 4.3.6 (a) the fibre is pumped at 2100 nm. For this

experiment the fibre is pumped in the anomalous dispersion regime, shifted nearly 500 nm away from the zero dispersion. The continuum extends from 1500 nm up to nearly 2700 nm. Starting at the pump wavelength and looking at shorter wavelength the intensity is continuously decreasing until the zero dispersion point is reached. After crossing the zero dispersion an intense peak is observed at 1600 nm before vanishing at shorter wavelengths. This can be explained by considering the anomalous dispersion regime first that is used for pumping the fibre. Energy is transferred to photons with shorter wavelengths by SPM or Raman-scattering. At the same time higher order solitons can be generated in this regime. As the soliton experiences small perturbations, fundamental soltions will be ejected due to the soliton fission. With the solitons experiencing intrapulse Raman scattering in the temporal short laser pulses used, the shorter wavelength part of a pulse can pump the longer wavelengths part of the pulse and therefore shifts the energy in the recorded spectrum back to longer wavelengths, explaining the decrease of intensity with decreasing wavelengths. Below the zero dispersion no solitons can be formed and we observe the intensity increase at around 1600 nm [118].

Figure 4.3.6 (b) and (c) show qualitatively similar spectra as both are pumped below the zero dispersion point. In (b) the fibre is pumped at 1600 nm while for (c) a wavelength of 1550 nm was chosen. This lets us investigate the influence of pumping intensity against distance from the zero dispersion point. (b) is closer to the zero dispersion point while we can see from figure 4.3.5 that (c) has the higher output power from the OPA. In (b) the SC extends from 900 nm up to 2200 nm while in (c) the limits are 1000 nm and 2600 nm, giving a supercontinuum with a spectral width of 1600 nm, nearly two octaves. Comparing the three pumping wavelengths, panel (c) also shows the flattest spectrum, with less wavelength dependent variations of the intensity compared to (a) and (b). It should also be mentioned here, that the average output power of (a) is more than an order of magnitude lower due to the use of the idler.

We found the spectral widest continuum with the pump wavelength at 1550 nm in our experiments. A more detailed analysis of figure 4.3.6 (c) can divide the spectrum into 3 regimes as indicated in figure 4.3.7. Area I shows a high intensity with a mostly flat profile from 1100 nm up to 1650 nm with

the intensity decreasing at lower wavelengths. This can be accounted to SPM. From 1650 nm to 2000 nm we observe an exponential decrease in intensity, as energy is shifted to longer wavelengths due to soliton fission and Raman scattering while still affected from the SPM of the pump pulse. Finally in III a flat plateau can be found up to 2600 nm. Area III is mainly dominated by soliton dynamics as will be demonstrated below.

To gain a better understanding of the supercontinuum generation in the ZBLAN fibre, the nonlinear pulse propagation is simulated considering the NLSE (equation 2.33). For the calculations the third order dispersion was assumed to be small and the effect of self-steepening neglected for pulse propagation [125] and equation 2.33 was simplified in that way. The Raman gain is fitted with a sum of two Gaussian functions using the following parameters [126]:

a_1	a_2	μ_1	μ_2	ω_1	ω_2
$0.54 \cdot 10^{-13}$ m/W	$0.25 \cdot 10^{-13}$ m/W	17.4 THz	12.4 THz	0.68 THz	13.5 THz

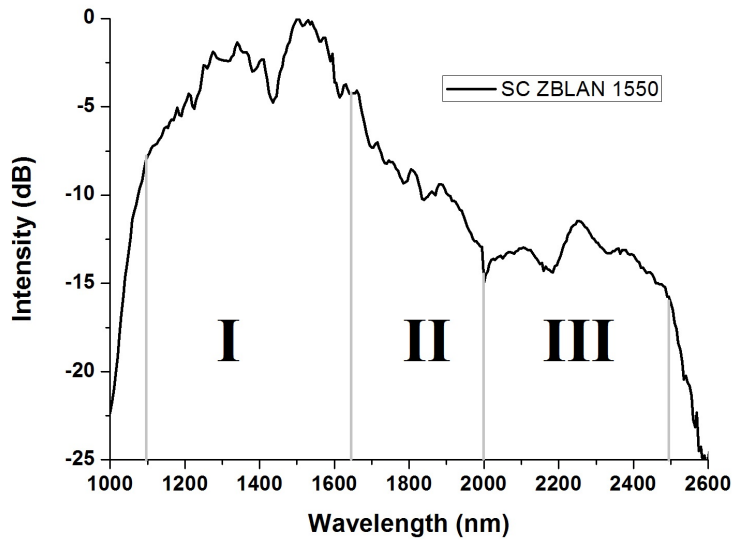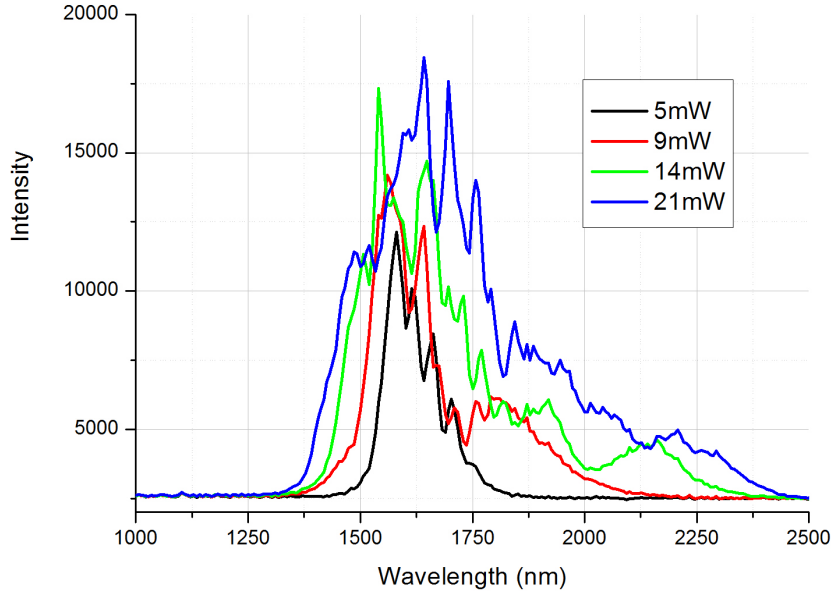*Table 4.3.1: Raman gain parameters used for ZBLAN SC simulations*

Figure 4.3.7: *Supercontinuum generated with a 1550 nm pump pulse in a dB scale. The spectrum can be divided into the three regimes I, II and II.*

Figure 4.3.8: *Evolution of the ZBLAN SC with increasing average pump power*

The nonlinear coefficient γ is an important parameter for determining the supercontinuum in the ZBLAN fibre. As γ is a material parameter, in this case of the ZBLAN fibre, a literature value can be used for this. To obtain a better value representing variations in the ZBLAN glass composition γ can be used as a fitting parameter for a set of measurements. With γ being constant either different SCs can be measured over different fibre lengths, and therefore over different interactions lengths, with a fixed pumping power or over a fixed length with varying pumping power. For the ease of carrying out the measurements, we have chosen to vary the optical pumping power to create a set of measurements. Figure 4.3.8 shows the evolution of the supercontinuum with increasing pumping power in such a set of measurements. Beginning with a literature value used for γ we have varied its value to find the best fit for all recorded SCs for one global value of γ. From this we have obtained a value of $\gamma = 1.1 \cdot 10^{-3}\,\text{W}^{-1}\text{m}^{-1}$, that we have used for following simulations.
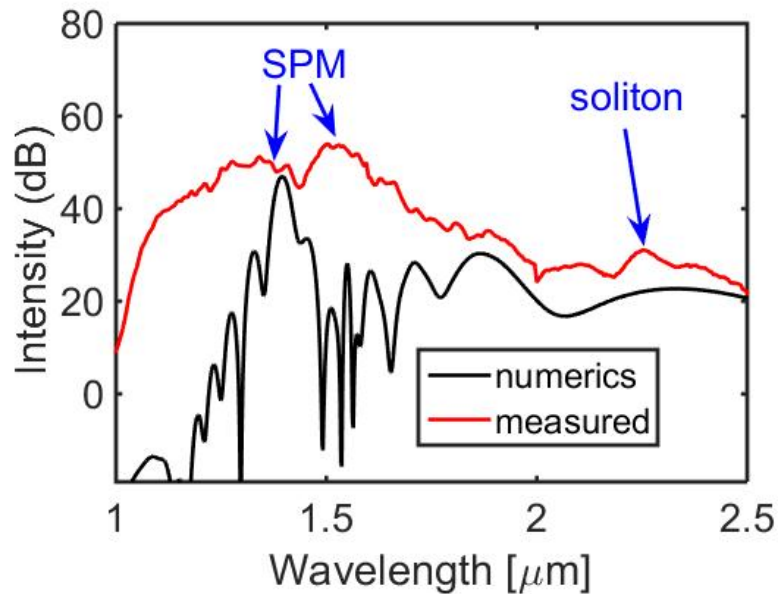
Figure 4.3.9: *Calculated output spectra (black) for 3.5 cm of ZBLAN fibre pumped at 1550 nm together with the experimental measured data (red).*

As the initial pulse a 100 fs sech-pulse (FWHM) was used with a variable peak power. The variable peak power was used to fit the experimental data, as the coupling into the fibre was uncertain during experiments.

In figure 4.3.9 both experimental and theoretical data is shown. While a perfect quantitative match between experimental and numerical data could not be achieved, important spectral characteristics for fibre generated supercontinua can be clearly detected [118]. Starting from the initial pump pulse, SPM creates a symmetrical pulse broadening. As soon as enough light intensity crosses the zero dispersion point at 1650 nm the formation of solitons dominates the sharp asymmetric broadening on the long wavelength side. Blue arrows in figure 4.3.9 clarify the origin of SPM- and soliton peaks in the spectrum.

The difference between numerical and experimental data on supercontinuum generation can be explained by the uncertainty of ZBLAN parameters due to variations of the glass composition as well as uncertainty on spectral characteristics of the input pulse . Inside the OPA a dichroic mirror is used to separate the signal pulse from the idler pulse, but some leftover intensity from
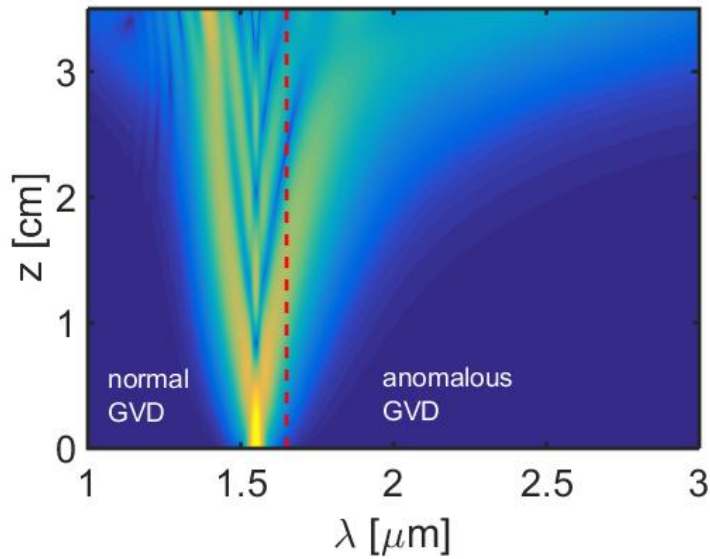
Figure 4.3.10: *Spectral evolution of an initial 100 fs pulse at 1550 nm travelling through a 3.5 cm long ZBLAN fibre. The red dashed line shows the zero dispersion.*

the idler is mixed into the signal pulse. Further during the parametric amplification process in the BBO crystal inside the OPA a chirp can be generated for the laser pulse. This potential chirp gives another degree of uncertainty on the temporal profile.

A more clear interpretation of the pulse evolution can be created by simulating the spectral evolution of the pulse as a function of the distance travelled through the fibre. In figure 4.3.10 the simulation of the spectral evolution can be seen, calculated for typical values of the pumping pulse. Starting with the initial pulse entering the fibre at the bottom of the figure only the symmetric broadening due to SPM can be observed. At a travelled distance inside the fibre of around 2 cm enough light intensity has crossed the zero dispersion (red dashed line) so that the formation of solitons gains importance in the anomalous dispersion regime. At 2.5 cm the soliton dynamics clearly dominate the broadening on the long wavelength side as an asymmetric tail starts to extend to the longer wavelengths. At the same time the intensity of the light created due to SPM in the anomalous regime is more and more reduced as energy is continuously transferred to longer wavelengths.
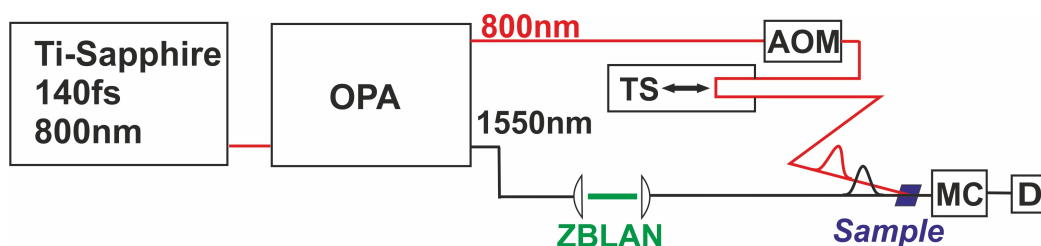
Figure 4.4.1: *Schematic of the layout for pump-probe measurements on P:P films using the ZBLAN supercontinuum*

We have demonstrated the supercontinuum generation in a ZBLAN fibre using our laser system. Alignment of the fibre coupling and the laser beam is simplified as green light in a third-harmonic process is created that can be observed by the human eye. In the next chapter we discuss the application of the ZBLAN supercontinuum and the advantages for the ultrafast spectroscopy setup.

4.4 Proof of principle measurements on conjugated polymer films

To test the performance of the setup with the ZBLAN SC pump-probe experiments are conducted on a thin film of a PCPDTBT:PCBM[60] (P:P) film on glass (BK7) substrates. We have chosen these films as they show a good signal and are well known from literature [127], and therefore offer a good possibility to compare the performance of the setup. PCPDTBT and PCBM[60] act as donor and acceptor respectively and form a charge-transfer system that is used for organic photo-voltaic experiments and applications. This system offers strong optical resonances that we have chosen to be probed by the newly designed setup.

Figure 4.4.1 shows a schematic of the layout that was used for the measurements on the P:P films using the ZBLAN supercontinuum. The residual 800 nm fundamental output of the OPA is used as the pump. All measurements were done using the AOM for modulation at half the repetition rate of the RegA. The supercontinuum is generated in a piece of ZBLAN fibre as discussed in

chapter 4.3.2, a monochromator from Optpometrics (DMC1-06) is used for spectral selectivity. The P:P films were prepared from solutions with a ratio of 1:2 of both material in chloroform by spin coating at 1500 rpm for 30 s.

The first pump-probe measurements on the P:P films showed a decreasing signal intensity during longer laser illumination, and repeating measurements proofed the instability of the blend under illumination in oxygen atmosphere as can be seen in figure 4.4.2 (a). After 5 directly repeated measurements nearly the signal has ceased completely, while translating the sample and illuminating a different spot on the sample brings the signal back to the original strength. To avoid the degradation process following films were prepared and sealed inside the glovebox. First the P:P film is spin-coated in the normal way. On the prepared substrate a layer of the air-tight *TorrSeal* is applied around the edge of the substrate and a second glass substrate is put on top (figure 4.4.2 (b) insert) to avoid any oxygen contact. Repeating measurements on films prepared in this way showed strongly enhanced stability. In figure figure 4.4.2 (b) consecutive measurements on the same sample spot are shown over the time of one hour under laser illumination without any signs of degradation.

To demonstrate the capabilities of the created setup, pump-probe measurements have been executed with steps of 40 nm for the probe wavelength between each measurement. After recording the data for all wavelengths we
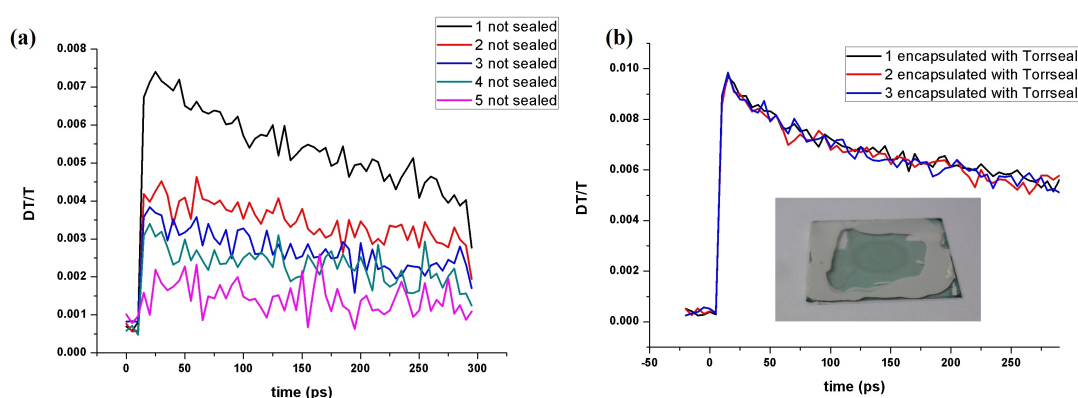
Figure 4.4.2: *Pump-probe measurement at 1200 nm of P:P film in air (a) and sealed under nitrogen atmosphere (b). The insert shows the sealed film.*
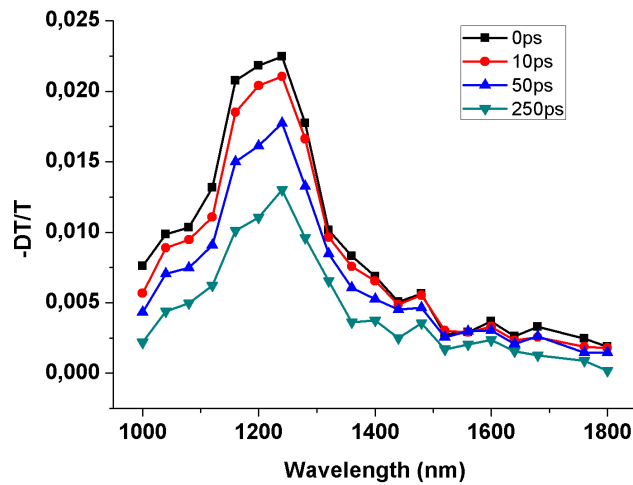
Figure 4.4.3: *Differential transmission (DT/T) spectra obtained from a PCPDTBT:PCBM film at different time delays after the pump excitation.*

plot the data at a fixed delay versus the probe wavelength to create a spectrum of the sample.

The complete measured spectrum of the film can be seen in figure 4.4.3 for a delay of 0, 10, 50 and 250 ps. The recorded differential transmission is negative, indicating an increased absorption of the blend due to the pump beam. The strongest signal can be seen at around 1250 nm with a continuous decay to the longer wavelength side. This prominent feature of the P:P blend has
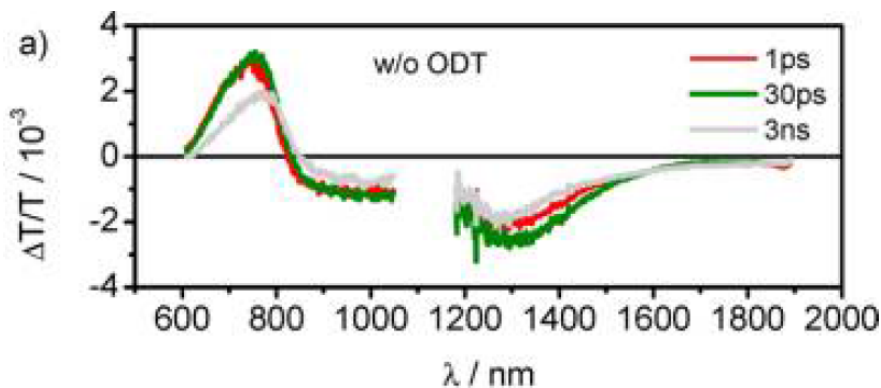
Figure 4.4.4: *4.4.3 from [127]*

been previously ascribed to positive polarons and triplet excitons [128], [129]. Upon the excitation through the pump beam excitons are created that can dissociate into charged particles if they are in direct vicinity of an acceptor-donor interface. Both excitons and polarons open up new - pump-induced - optical transitions increasing the absorption as seen in figure 4.4.3.

For comparison we have shown a similar spectrum in figure 4.4.4 taken from literature [127] using a blend of the same materials with a comparable ratio of the blend. We observe the reproducibility of the spectrum, showing the same strong feature at around 1300 nm. At the same time our recorded life times are in comparison on a much shorter time-scale, showing a decay of the signal by approximately 50 % after 250 ps. This difference can be explained by a much stronger pumping in our experiments, whereby additional recombination channels are provided because of the higher charge carrier density created by the pump. Further can a methodological advantage be seen as we recorded a continuous spectrum starting at 1000 nm, while the spectrum in figure 4.4.4 was measured with a conventional setup using two separate broadband probe sources for the visible and the NIR, leaving a gap between 1000 nm und around 1150 nm, which was not accessible for the used broadband sources.

A further advantage cannot be seen in the measured data but arises from the much more complicated alignment of the beam overlap for not visible
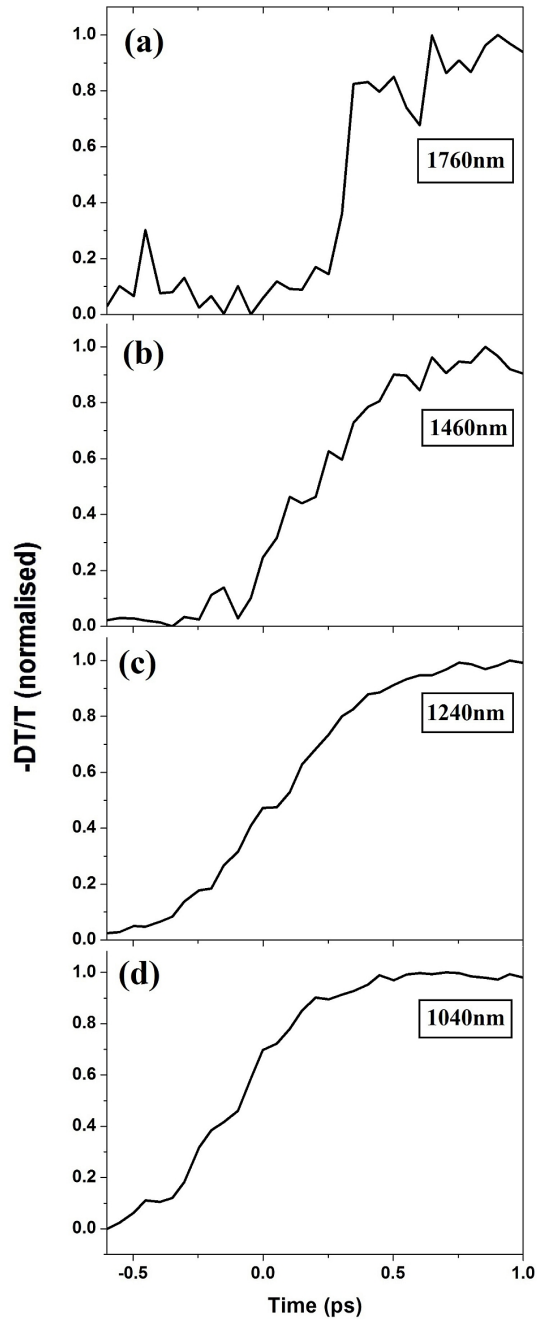

***Figure 4.4.5:** Comparison of rise time in DT/T at different probe wavelengths across the SC.*

light. Due to the generated SC we still can detect light on the short wavelength side of the SC with the used CCD-camera and use it for an easy alignment.

Figure 4.4.5 shows the rise times of the differential transmission signal for different probe wavelengths, for 1040 nm, 1240 nm, 1480 nm and 1760 nm. The rise times are estimated through an exponential fit while we have defined the zero time at the wavelength of the original OPA pump pulse. The shortest rise time was found for 1760 nm in figure 4.4.5 (a) and is estimated to be around 100 fs, while the longest rise time for 1240 nm in figure 4.4.5 (c) is about 1 ps. The rise time can either be attributed to the physical process happening during the excitation of the P:P blend or to the temporal shape of the pump and probe pulse.

From experiments using a white light SC on the same materials we know that the rise time of the DT/T signal in this spectral range should be below 200 fs [128], [130]. Further have experiments using 15 fs pulses shown that the photo-physical processes itself is on a time scale shorter than 200 fs [131]. Therefore we attribute the variation in rise time to the temporal dispersion of the SC pulse generated in the fibre.
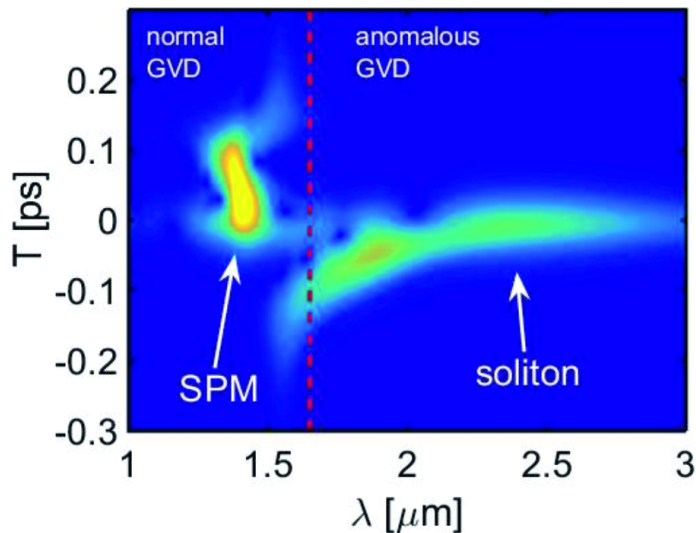
Figure 4.4.6: *Simulated XFROG for the output signal from figure 4.3.9 and a 35 fs sech pulse as a reference. The red dashed line shows the zero dispersion.*

For a better understanding cross-correlation frequency-resolved optical gating (XFROG) simulations of the SC dispersion in time have been carried out using a 35 fs sech pulse as a reference (figure 4.4.6). The XFROG explains the longest rise time at 1480 nm as the strongest temporal modifications occur close to the zero dispersion wavelength. At the longer wavelength side we experience the shortest temporal widths due to the self-compressing soliton dynamics [132], while for the SPM regime a width in between the two can be seen. The XFROG trace can in principle be used to compensate for the instrument's response function at different wavelengths and recover time resolution via a deconvolution algorithm.

# 5 Growth of organic semiconducting crystals inside a capillary optical fibre

For increasing the interaction of light with organic semiconducting materials we have chosen an approach which can strongly increase this interaction. We use hollow core silica fibres to grow single crystals inside the fibre. By confining light into the fibre the interaction length with the organic can be strongly increased while maintaining a small diameter of the light beam. For characterisation of the hybrid fibre optical microscopy is used together with Raman spectroscopy and X-ray diffraction.

5.1 Experimental designs for crystal growth inside the hollow core fibres

For some time interest existed in combining the advantages of using the vast flexibility of properties of organic solids with waveguiding properties, and especially with the strong confinement of light during waveguiding. To achieve this different approaches have been used, like growing single crystal fibres or nanowires [133], that can directly used as waveguides. Other approaches are using hollow core glass capillaries for growing an organic single crystal inside this capillary. While most of the configurations in this case use capillary diameters in the range of 20-50 µm [134], [135], for some crystal materials capillary diameters in the range of under 10 µm have been reported [43], [136]. As we have found that crystal core fibres with geometrical dimensions of

optical fibres could only be found for some specific organic materials, we are investigating a more general approach for growing organic single crystals inside a fibre capillary. The goal is to develop a method which is transferable to different materials, while working with optical fibre dimensions. Because of high refractive indices of many organic materials relative to silica glass, this means that for a potential single mode regime core diameters of below one micron have to be realised.

In this section the methods that have been developed and explored in order to grow single crystals inside a hollow core fibre are discussed. We use approaches based on the crystal growth from the melt, more specifically the Bridgman technique that was explained in section 2.1. First a hollow core fibre has to be filled with the molten material. This is achieved by creating a reservoir of material powder. The hollow core fibres are attached to the reservoir and by placing both inside a furnace the material can melt and fill the capillary fibre. In a second step a controlled cooling process leads to the solidification of the material in order to create single crystals inside the fibre. Instead of using translation to change the temperature gradient relative to the position of the fibre as explained in section 2.1, we are changing the temperature settings of the two-zone furnace in order to move the temperature gradient while the fibre is in a fixed position.
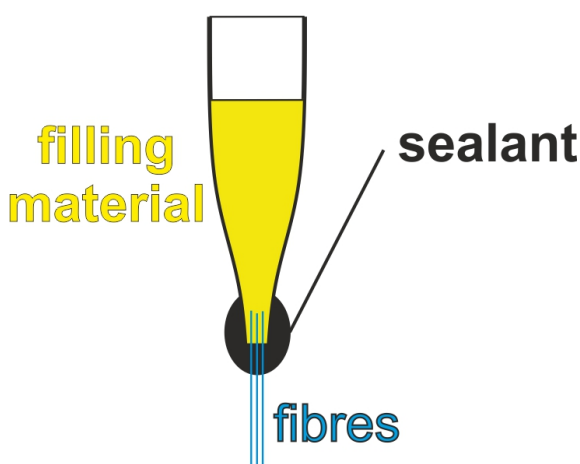
Figure 5.1.1: Reservoir with material powder (yellow), attached fibres (blue) and sealant (black).

For the first step a reservoir is filled with the organic material as powder. We have optimised a design to attach the hollow core fibres to the reservoir. The reservoir is made from a borosilicate glass tube with an inner diameter of 5 mm and a length of 4 cm. For attaching the fibres into the reservoir one end of the glass tube is tapered, reducing the inner diameter and for that the space between the fibre and the reservoir wall. The prepared fibres

are inserted 2-3 mm into the tapered end. For a typical growth process we attach about 10 fibres, reducing the gap between fibre and the glass wall as well as increasing the efficiency by increasing the amount of filled fibres produced per growth.

For fixing the fibres and sealing the reservoir, both high-temperature sealant and fire cement mentioned in section 3.2.4 have been used, according to the demands of the experiment. Figure 5.1.1 illustrates this structure with a schematic. The high temperature sealant is the preferred material used for attaching the fibres as it is easier to handle and shows better air sealing properties than the fire cement. With the temperatures being limited to below 300 °C, the fire cement is used for higher melting point materials. The material is loaded into the reservoir inside the glovebox to reduce oxygen and water contamination. To protect the attached fibres a glass tube is attached to the reservoir from the bottom side,completely covering the exposed fibres.

To create a nitrogen atmosphere inside the filled reservoir, an airtight sealing has to be created at both ends while being inside the glovebox. Two different approaches have been used to achieve this: The first approach is illustrated in figure 5.1.2 (a), showing the filled reservoir as before. Either a glass or a metal piston is used that just fits inside the cylindrical cavity at the top of the reservoir in order to minimise the empty part of the reservoir. Subsequently the gap between the reservoir and the piston at the top is sealed with the same sealant as used for attaching the fibres while still being inside the glovebox.

For the second sealing method, a neck in the glass wall of the reservoir is produced in the fabrication process. It is in the top part of the glass cylinder as can be seen in figure 5.1.2. In a first step after loading the material into the prepared reservoir a piston is used to seal the whole reservoir above the neck in order to generate a reservoir with nitrogen atmosphere inside, that can be handled outside the glovebox. By heating with a propane-oxygen blowtorch the glass at the neck is heated up, so that the neck will collapse and the top part including the piston can be removed from the reservoir leaving it closed at the collapsed neck. Because of the high temperature of the used flame, the distance between the filling material and the neck in the glass has to be
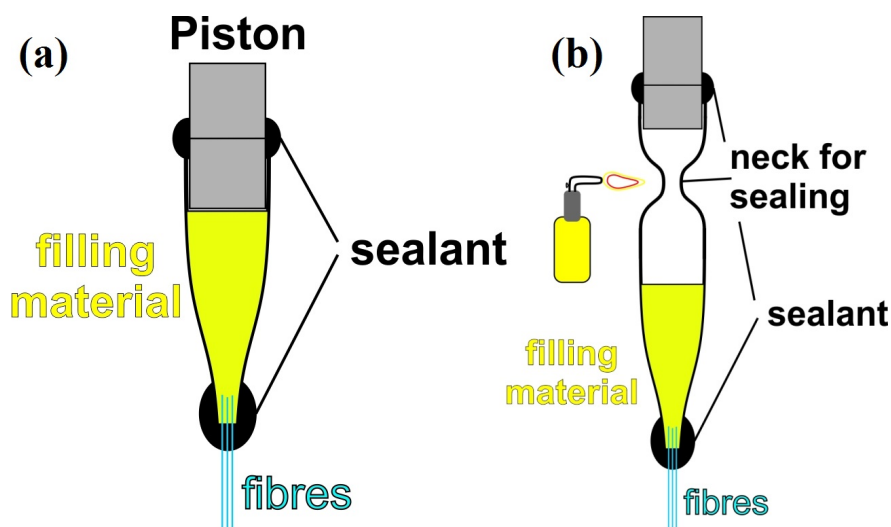
Figure 5.1.2: *Sealing methods for the fibre growth reservoir using a flame to seal off at a neck of the glass (a) or using a piston with sealant (b).*

large enough to not influence the filling material during the heating process by flame.

Both sealing methods have been successfully used with different advantages. The general improvement by adding the neck for sealing is creating an airtight closure at the top of the reservoir that works for the whole temperature range of the furnace. Further by only using a glass seal the probability of contamination is strongly decreased in comparison to using a sealant at the top together with the piston. As a first filling material Anthracene has been successfully used with this configuration.

When using Perylene as a second filling material the disadvantages of this method could be observed: Because of its high vapour pressure Perylene sublimates at atmospheric pressure instead of melting. This leads to the formation of small crystals at the top of the sealed reservoir as it re-sublimates. Fibre filling experiments for this combination of the method and material were showing poor fills, without continuous filling and just sporadic crystal growth. Using the piston method, we can strongly decrease the gas volume inside the reservoir after filling it with the organic material. By compressing the filling powder with the piston before the top sealing process, the Nitrogen volume inside the reservoir is minimised. During the heating process the small gas

volume leads to an increase of the pressure as more of the Perylene transfers into the gas phase. The increase of the pressure compensates for the vapour pressure and finally an equilibrium is created between Perylene sublimating and melting.

In figure 5.1.3 we can see a schematic of the reservoir with attached fibres in a protective glass tube inside the furnace on the left side. Next to it on the right the temperature profile of a growth process with Anthracene is shown with respect to the spatial position inside the furnace. The reservoir hangs from the top inside the furnace, while both ends of the furnace are sealed with insulating material to keep a stable temperature profile. The temperature $\Delta T = T_{Furnace} - T_{Melt}$ is plotted relative to the melting point of the material. This means that material with a positive value on the X-axis in its position is in the liquid phase and crystallises when crossing the Y-axis. The
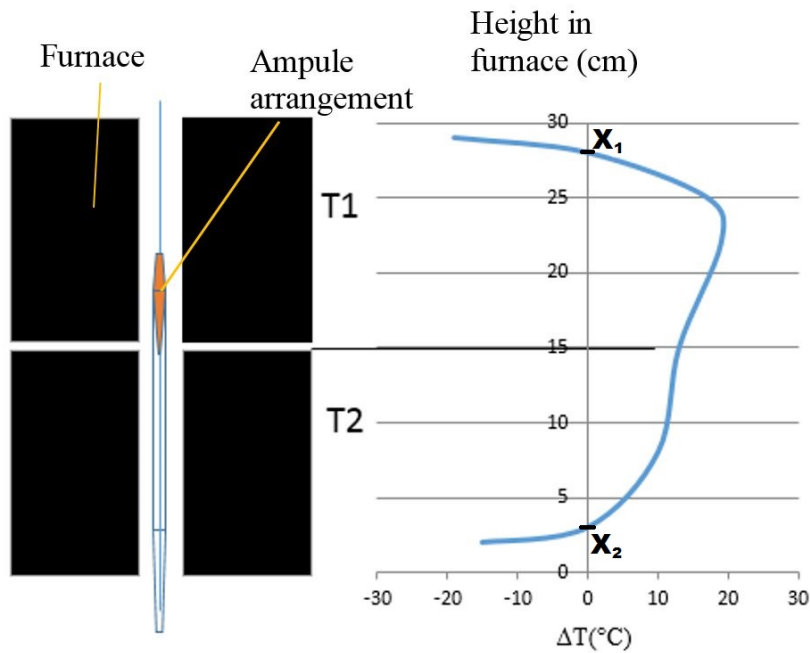
Figure 5.1.3: *Schematic of the two-zone furnace during a fibre filling process with the furnace temperature profile shown on the right side. Here T_1 and T_2 depict the two controllable temperature zones. The Y-axis shows the distance from the bottom of the furnace while the X-axis gives the temperature relative to the melting point of the used material: $\Delta T = T_{Furnace} - T_{Melt}$. We call the crystallisation points X_1 and X_2*

two temperature zones T_1 and T_2 are chosen to create a temperature profile with the hotter zone at the reservoir and an negative temperature gradient approaching the bottom side of the furnace. In this way a combined decrease of both temperature zones leads to a shift of the temperature profile in figure 5.1.3 to the left. With decreasing overall temperature the bottom crystallising point x_2 shifts to higher positions, allowing the growth to begin from the bottom.

The length of the attached fibres has been chosen to be long enough to reach into the colder temperature zone at the end of the furnace. In this way the molten material flowing into the fibre will automatically create a seal of the hollow core as it crystallises at the cold end. For the furnace used this gives a fibre length of about 18 cm. The furnace is set up vertical with the higher temperature zone at the top. Because of the unknown viscosity of the melt at the given temperature we decided to use the vertical setup. In this way not only the capillary force leads to a filling process with the melt, but also the gravitational force increases the speed of the process as discussed in chapter 2.4. Further the vertical setup creates a symmetric crystal shape inside the fibre instead of a D-shape for horizontal setups with a typical gap between the top of the glass wall and the crystal [51]. As a third advantage convection perpendicular to the growth process is avoided and a convection parallel to the growth direction is preferred. This helps to avoid supercooling of the liquid phase close to the liquid-solid interface, resulting in better quality crystals [50].

5.2 Optimisation of the design and parameters for growing crystals

The filling process of the fibre can be considered in a sequence of steps. First the preparation of the reservoir and fibres as described above. The next steps is melting the material in the reservoir and the filling of the hollow core of the fibre with the material in the liquid phase. After a homogeneous liquid fill has been achieved the crystallisation process is initiated by consecutively lowering the temperature. This allows us to create and shift the needed temperature

profile. The final step is if needed an annealing step after crystallisation and then cooling to room temperature. After this the crystals can be examined and the highest quality pieces selected to be cut out of the whole fibre. Most of the optimisation has been carried out empirically.

For the filling with the melt a higher temperature is favourable as the materials viscosity decreases with an increase of the temperature T_1. On the other hand the probability of degradation also increases with temperature. At this step we use a constant temperature for both zones. The experiments have shown that for all used materials a temperature ΔT of $+20\,°C$ is sufficient to fill the capillary within $1\,h$ to a length of about $15\,cm$ where the filling process stops at X_2. Longer filling times have been explored, but did not show any advantage with respect to the crystal or fill quality.

The crystal growth process is started by lowering the value of T_2 with a rate of $5\,°C/h$ until a temperature difference between T_1 and T_2 of $15\,°C$ is reached. This value has shown to give a good stability of the temperature gradient, while the gradient is big enough to initiate the crystal growth from the bottom while the reservoir at the top stays in the liquid phase, supplying enough material to grow the crystal without gaps. Increasing the temperature gradient leads to small temperature fluctuations in the middle of the furnace, lowering the crystal quality. Higher temperature gradients would be preferable, but are not feasible without adding a baffle to the setup. From this point both T_1 and T_2 are lowered together with the same cooling rate as before until both zones are below the melting point of the material and the whole reservoir is crystallised.

The last step is cooling the fibre down to room temperature. This can we done with an additional annealing step or without. A cooling rate of about $30\,°C/h$ has been slow enough to not create tension inside the crystal during the cooling that will lead to lots of cracks. Switching the furnace off directly after the crystallisation creates this kind of cracks, while continuing with a cooling rate of $5\,°C/h$ until room temperature did not show any enhancement and is not used for that reason.

5.3 Structural characterization of filled fibres

The fastest way to evaluate the filling process of the hollow core fibres is by optical microscopy. Standard optical microscopy has proven to make the determination of the filling quality difficult, as the side view of the hollow core fibre strongly depends on the focusing plane. In this way determining the contrast between empty and filled parts can be difficult as can be seen in figure 5.3.1 (a). The birefringent properties of the filling materials let us strongly increase the contrast by using cross-polarising filters with a bottom illumination in the microscope. Figure 5.3.1 (a) and (b) show exactly the same fibre with and without the polarising filters in place. We can see in figure 5.3.1 (b) that only the core of the fibre is lighting up. This gives us an excellent way of determining and evaluating the quality of the crystal fill inside the fibre.

For a good quality a homogeneous fill is needed, not leaving gaps between the crystal and the fibre, as well as having a long piece of fibre (longer than 1 cm) without cracks in it. Optical microscopy shows the advantage of a fast possibility to scan the 15 cm long pieces of fibre in order to find the longest homogeneous fills. Figure 5.3.2 shows an example of problems of the fill. The right arrow points at a region without any filling material, potentially caused by a gas bubble caught inside the fibre while the left arrow points at a gap between the wall of the fibre and the crystal.
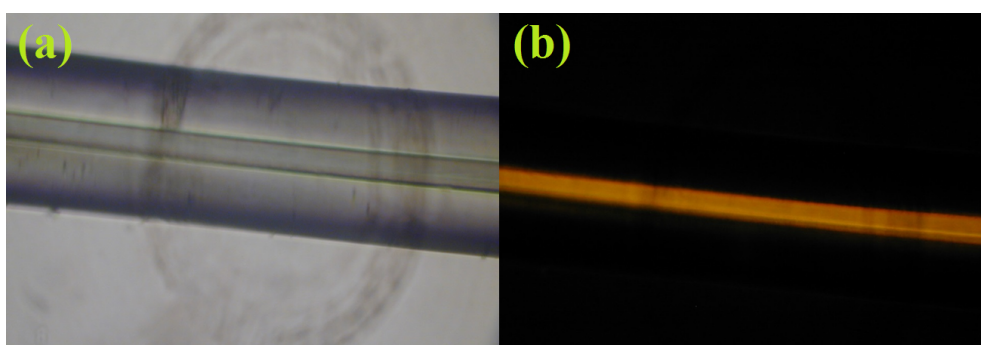
Figure 5.3.1: *Optical microscope picture of an Anthracene filled hollow core fibre with 13.5 μm core diameter in normal microscopy configuration (a) and using cross-polarising microscopy (b)*

In a fibre growth process we can distinguish different qualities of the crystal growth along the length of the fibre. For visualisation purposes the fibre is shown next to the furnace in figure 5.3.3, to connect the areas of growth with the temperature profile of the furnace. We have distinguished three different zones called **A**, **B** and **C** and shown a typical cross-polarised picture for each zone. The highest quality of the crystal can be found in zone **B**, situated in the middle of the lower temperature zone of the furnace. We can see a
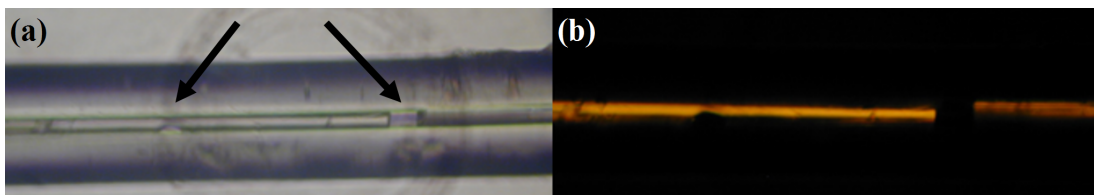
Figure 5.3.2: *Example of a fill with gaps and air bubbles inside the core without and with cross polarised filter*
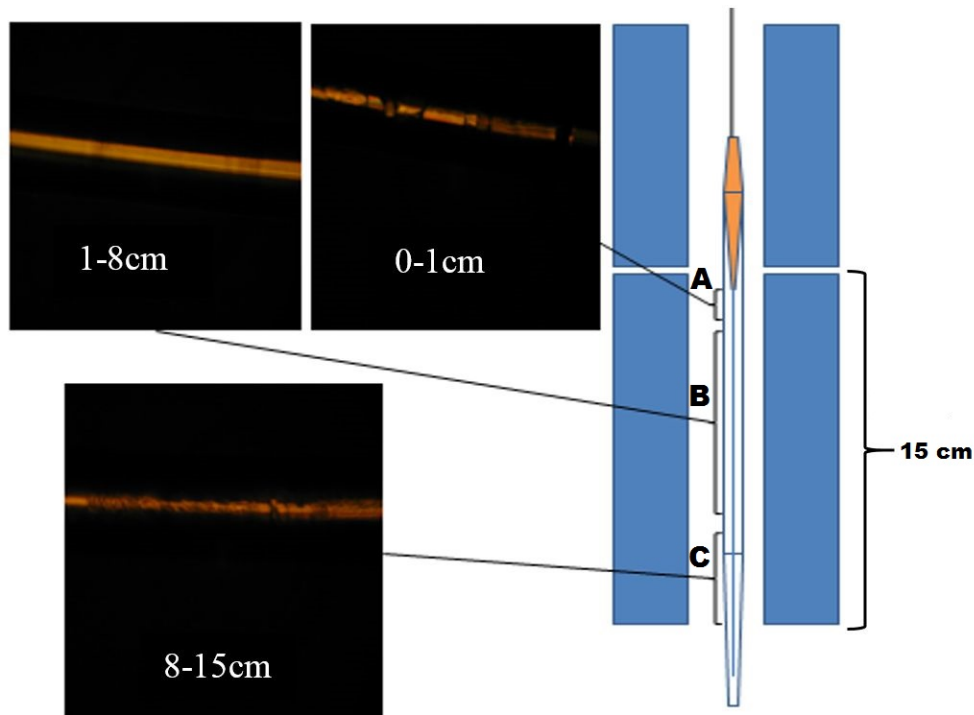
Figure 5.3.3: *Exemplary crystal growth inside a 13 μm hollow core fibre using Anthracene. Different areas of growth can be distinguished along the length of the fibre.*

homogeneous crystal without any cracks in the middle picture. Typically this area is about 7 cm long, but can fluctuate from growth to growth. All fibres for following experiments are cut out of this latter zone.

Above we find a relatively short area **A** with a high amount of cracks as well as gaps in between crystals. We attribute this to the proximity to the reservoir. When the solid-liquid interface during the crystallisation process reaches this area, the temperature difference between the interface and the reservoir is already too small to keep a continuous liquid reservoir upright from above, showing polycrystalline growth as well as gaps that cannot be filled with melt.

The third zone **C** is found at the bottom end and is relatively long. We can see here an area without many gaps, but with a lack of uniformity of the crystal. Polycrystalline growth is observed, possibly being explained by temperature fluctuations at the bottom end of the furnace. Another reason might be multiple seeds being created during the sealing process with the melt as crystallisation can start at multiple spots.

5.4 Structural Analysis of hybrid fibres

After investigating the filled fibres by microscopy and selecting the fibre parts to be used for later experiments, structural analysis of these pieces has been carried out. The first method of choice is Raman-spectroscopy as it offers, with micro-Raman, the possibility to do spatial defined measurements on the scale of micrometres and is not invasive, i.e. does not damage the sample or does need for specific preparation procedures.

We have carried out Raman spectroscopy on a dropcast film made from the powder material used for filling processes as well as on a film of the material on a glass substrate and compared these spectra with the Raman spectrum of the filled hollow core fibres. In figure 5.4.1 we can see the spectra of a drop-cast DPA-film on a glass substrate together with the spectrum of a DPA filled fibre. Both spectra have been recorded using a 785 nm laser and are base-lined and normalised and for comparability shifted on the Y-axis. We observe sharp and distinctive peaks and can localise the main peaks at $390\,\mathrm{cm}^{-1}$, $420\,\mathrm{cm}^{-1}$,

$890\,\mathrm{cm}^{-1}$, $1000\,\mathrm{cm}^{-1}$, $1030\,\mathrm{cm}^{-1}$, $1220\,\mathrm{cm}^{-1}$, $1280\,\mathrm{cm}^{-1}$, $1420\,\mathrm{cm}^{-1}$, $1530\,\mathrm{cm}^{-1}$, $1560\,\mathrm{cm}^{-1}$ and $1610\,\mathrm{cm}^{-1}$. The recorded Raman spectrum for DPA shows a very good resemblance to literature reports for DPA [137]. When comparing the spectrum recorded from the dropcast film with the spectrum recorded of the crystal of the fibre core nearly all the peak locations are reproduced. At the same time the relative intensities of some peaks have changed. The strongest deviations are at $420\,\mathrm{cm}^{-1}$, $1000\,\mathrm{cm}^{-1}$ and $1600\,\mathrm{cm}^{-1}$. In the range of $200\text{-}250\,\mathrm{cm}^{-1}$ a series of peaks is showing up that were not distinct for the DPA film. Overall the trend can be recognised that the deviations are stronger for low wavenumbers, while the match is better for higher wavenumbers.

The differences in the recorded spectra can be understood when considering different origins of the peaks in the Raman spectrum. These can be split into intra-molecular and inter-molecular vibrations and rotations. Because our
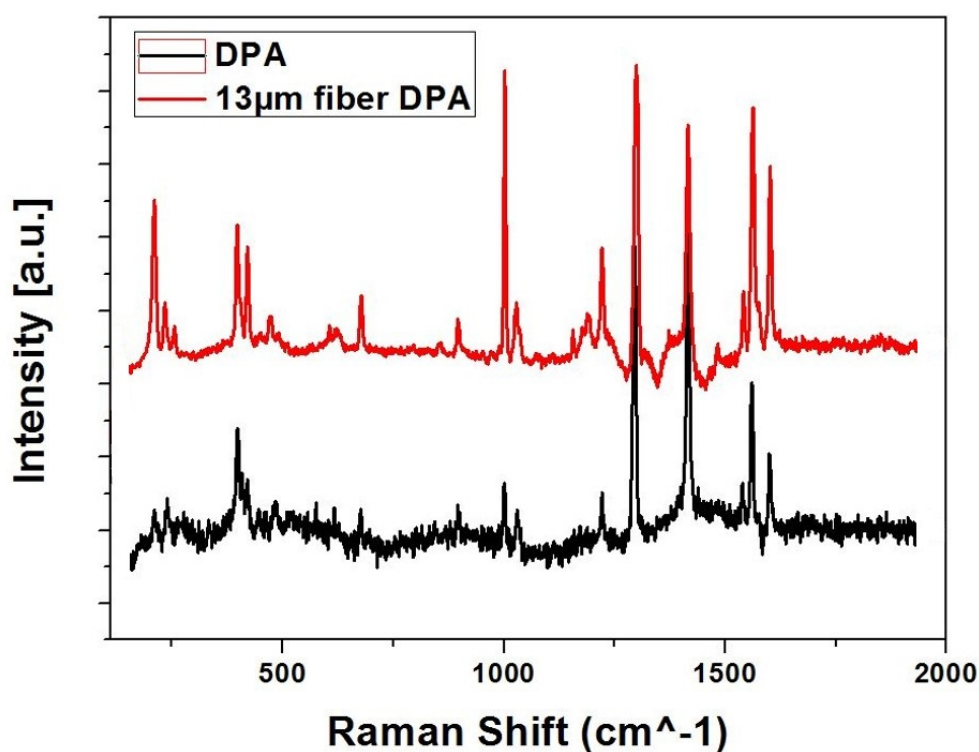
Figure 5.4.1: Normalised Raman spectrum of a drop-cast DPA film (black) together with the spectrum of a DPA filled fibre (red).

crystal is grown inside a capillary and therefore is in direct contact with the surrounding glass, we expect different kinds of vibrations to be differently affected by this circumstance. While intra-molecular vibrations are hardly affected, inter-molecular vibrations are expected to be stronger affected by the limiting glass structure around the crystal. As lattice vibrations like phonons are much more delocalised, an overlap with the glass structure is much more likely to be found. Similarly is out of plane bending expected to be more affected then in plane bending. As a general rule can inter-molecular vibrations be found at lower wavenumbers in the Raman spectrum as well as can out of plane bending be found at lower wavenumbers compared to in plane bendings [83], [138]. For that reason we attribute the differences in relativ intensities from figure 5.4.1 to be originating in the confinement in the glass structure. We conclude from the overall match that no chemical transition has taken place during the fibre filling process and that there is a DPA crystal inside the hollow core fibre having a good level of purity [139].

For analysis of not only the material composition but also the crystal structure single crystal X-ray diffraction has been carried on an *Agilent Supernova Dual*. The measurements could be done with the crystal inside the silica glass fibre, as the amorphous glass adds only a background signal without distinctive peaks. Figure 5.4.2 shows the diffraction pattern of a DPA filled fibre. The diffraction pattern consists of a series of very sharp, distinctive peaks. These
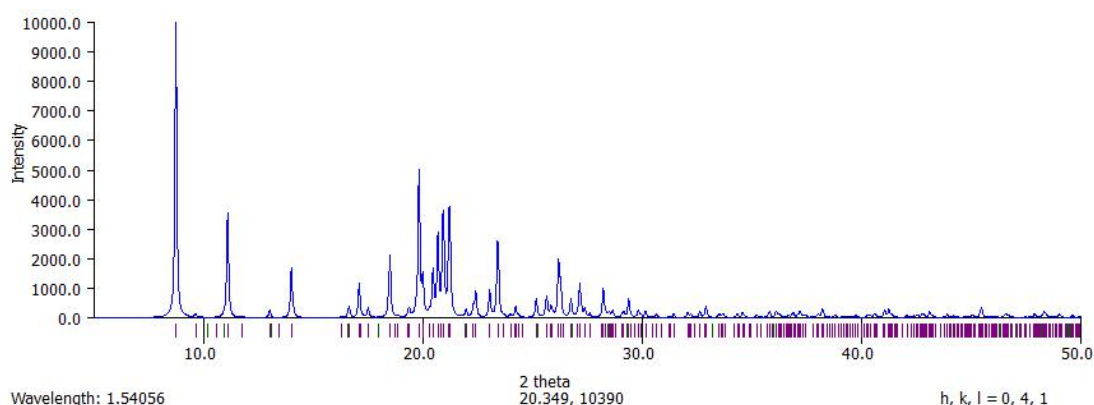
Figure 5.4.2: *Single crystal X-ray diffraction pattern of a DPA filled fibre*

confirm us the crystallinity of our sample. Further single crystal diffraction has been carried out, proofing that the sample consists of one single crystal instead of a polycrystalline material growing inside the capillary.

The more detailed analysis of the diffraction pattern confirms the molecules inside the unit cell being DPA with a molecular weight of 330.40 and the chemical formula $C_{26}H_{18}$. We have found a monoclinic crystal system with the space group $P2_1/c$. The unit cell dimensions are: a=9.9836 Å, b=20.2568 Å and c=9.4359 Å with the angles α=90 °, β=113.092 °, and γ=90 ° which are a good match to measured literature values [140].

Figure 5.4.3 shows the unit cell of the DPA crystal in the fibre core. We find one body-centred, two face-centred molecules and four molecules on the edges and eight on the corners of the unit cell, giving an overall of four molecules per unit cell.
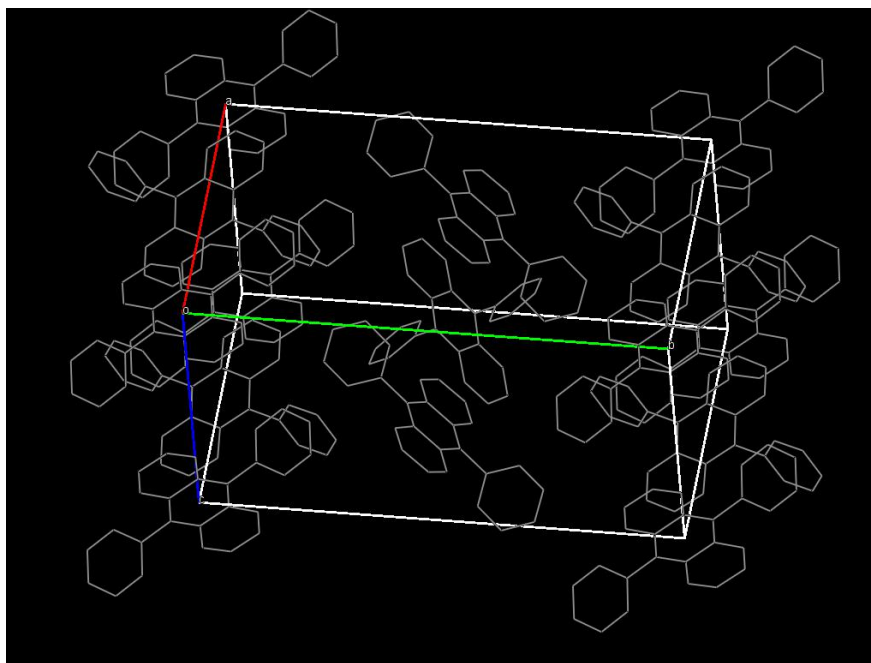
Figure 5.4.3: *Unit cell of a DPA filled fibre determined by single crystal X-ray diffraction*

6 Optical Characterization of filled fibres

We have discussed in chapter 5 the preparation of hollow core fibres with organic single crystals and the analysis of the quality of the grown crystal. In this chapter we are investigating the optical properties of the prepared fibres and have a closer look at light guided through these. The highest nonlinear responses are expected from DPA and BPA. As we were unably to melt BPA without chemical decomposition even in the absence of oxygen, this chapter will cover DPA as a filling material.

6.1 Sample preparation
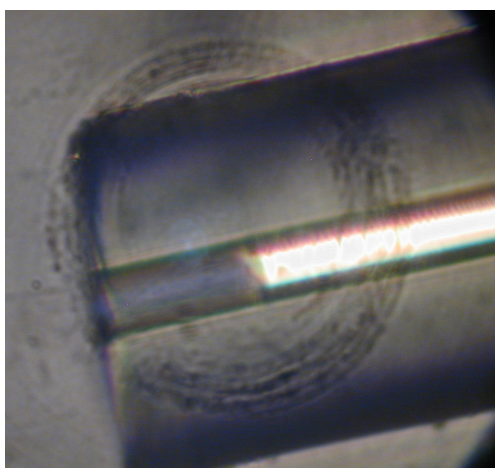
Figure 6.1.1: Picture of an Anthracene filled fibre after the cleaving. The concentric rings are artefacts originated in scratched optics of the microscope and are present in all pictures.

After a piece of filled fibre has been selected, we have cut that piece out of the 15 cm long fibre. The typical length used for optical experiments is in the range of 5-15 mm. For cutting the *Thorlabs Fiber Scribe* has been used, utilising a 30°, single bevel, ruby blade. The scribe is used to score the fibre perpendicular to the ruby edge, creating a light score without breaking the fibre. Upon applying a light stress to the fibre, the scored edge acts as a stress point and a clean cleave is created.
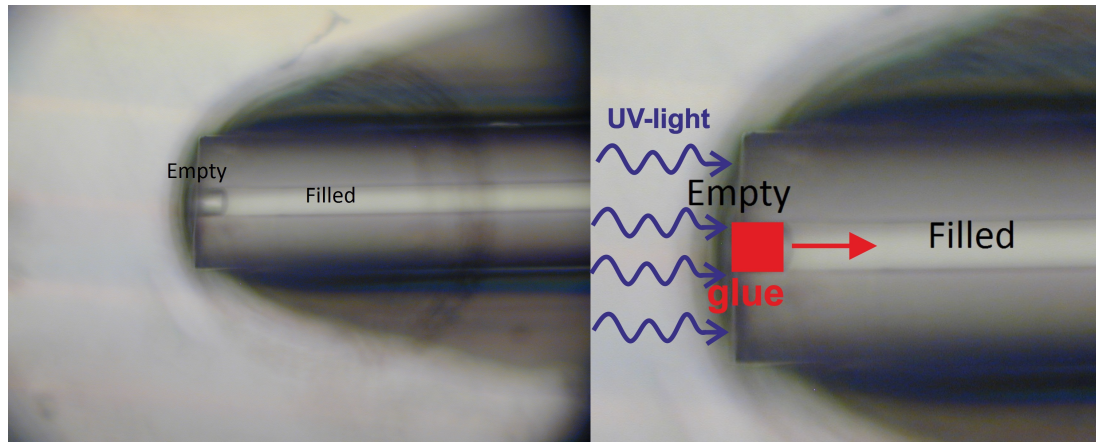
Figure 6.1.2: *Microscope picture of a filled fibre after cleaving. On the left side we have labelled the filled core and the empty core at the end. The right side illustrates the sealing of the end with UV-curing glue.*

The quality of the cleaving sets a limit to the light coupling into the fibre. With the crystal grown in the hollow core the situation of cleaving the fibre is more complicated as the scoring of the fibre creates a nice cleaving of the silica glass, but the crack does not extend into the crystal in the middle. Instead of the cleaving, the crystal inside breaks as the surrounding glass wall snaps off. Figure 6.1.1 is an example of a filled fibre after the cleaving process. In this example an Anthracene filled fibre was cleaved and one can see the end of the fibre in a cross-polarised picture. In this case the last $50\,\mu m$ of the fibre show an empty core with the fibre filling being removed during the cleaving process.

In order to overcome this problem we have used a UV-curing optical adhesive in order to fill the gap. The *NOA61* glue from *Norland Optic Adhesives* o the needed properties. A refractive index *n* of 1.56 gives a higher refractive index than the cladding, allowing light to guided. A low viscosity of $300\,CPS$ guarantees that the glue can easily flow into the gap by capillary force and fill it. Figure 6.1.2 illustrates the process: On the left side we can see a picture of a filled fibre with a gap at the end after cutting. The right side schematically explains the process. Because of the viscosity of the glue bringing the end of
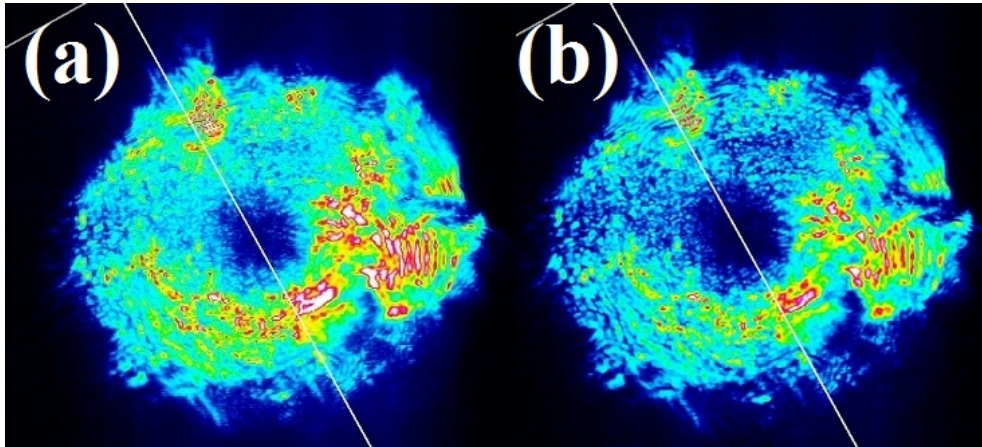
***Figure 6.1.3:** Beam profile taken of a HeNe-laser coupled into a 13 μm Anthracene filled fibre without sealing of the fibre end (a). The profile of the same experiment with a linear polarisation can be seen in (b)*

the fibre in contact with the glue allows the gap to be filled (red). A mercury lamp emitts UV-light (purple in figure 6.1.3) to cure the glue.

By doing experiments to couple light into the fibre without using the glue to fill the gap at the end, the beam profile detected after the fibre can be seen in figure 6.1.3 (a). The profile of the beam shows the main intensity in a ring-like distribution with a whole in the middle where the intensity is nearly zero. A similar profile can be created by light guided in a TE_{01}-mode that was mentioned in section 2.3.1. For the TE-mode the output light is polarised. This gives an easy way to verify a TE_{01}-mode by using polarised light. In figure 6.1.3 (b) we can see the beam profile for the same experiment as in (a) with using additionally a linear polariser. As one can notice the profile remains unchanged. For that reason and two further reasons we attribute the beam profile to the guidance in a cladding mode: Using a black, absorbing paint on the outside of the fibre reduces the transmitted light intensity strongly. Further the geometry of the beam profile reveals a ratio of diameter of the dark middle part to the bright intensity part of ≈ 0.13 while the ratio of core to cladding of the fibre is $\frac{r_{core}}{r_{cladding}} = \frac{125}{13.5} \approx 0.11$, which is comparable for both.

6.2 Fibre properties

For optical experiments if not mentioned otherwise all fibres are filled with a DPA crystal. For the experiments two different fibres have been prepared: A 13 µm core diameter fibre and additionally a 1 µm core diameter fibre. The smaller core diameter has been chosen according to calculations described below.

One of the most important optical properties to be determined for the crystal in the core is the refractive index n. Not only to calculate the numerical aperture of the fibre according to equation 2.11 we need to know n, but also for calculating V (equation 2.13) and the number of modes together with the cutoff frequency λ_c (equation 2.15).

To measure the refractive index of DPA we use ellipsometry, allowing a fast measurement and modelling of a DPA thin film. The thin film has been prepared by spin-coating from a chlorobenzene solution at 2000 rpm. The
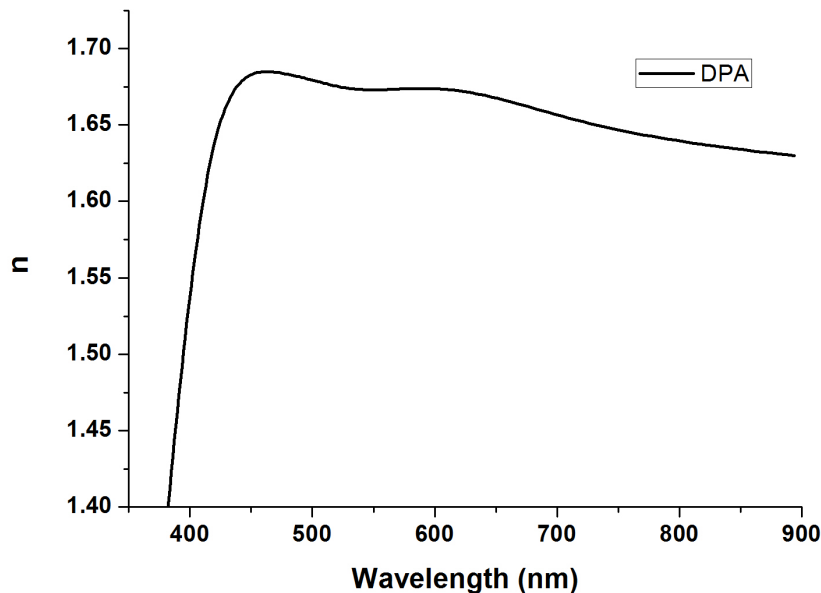
Figure 6.2.1: *Real part of the refractive index fitted by a model from the experimental data of the ellipsometer*

substrate used is a borofloat glass from *EdmundOptics*. To reduce reflection from the back of the substrate a diffusive layer of scotch tape is attached from underneath. The elipsometric measurements have been carried out at three different reflection angles, 65°, 70° and 75°, to increase the overall data used for fitting the data with a theoretical model. The experimental data was directly fitted to a model in the *CompleteEASE* software using the model "Glass substrate with an absorbing film". For this we have used the film thickness fixed with a value of 170 nm for all three reflection angles. With the model both the real part and the imaginary part of the film can be calculated from the data. In figure 6.2.1 the real part of $n(\lambda)$ is plotted against wavelength of light.

Besides the refractive index of the material we also need to know the absorption spectrum. As we could not use the *Cary 5000* in an efficient way to
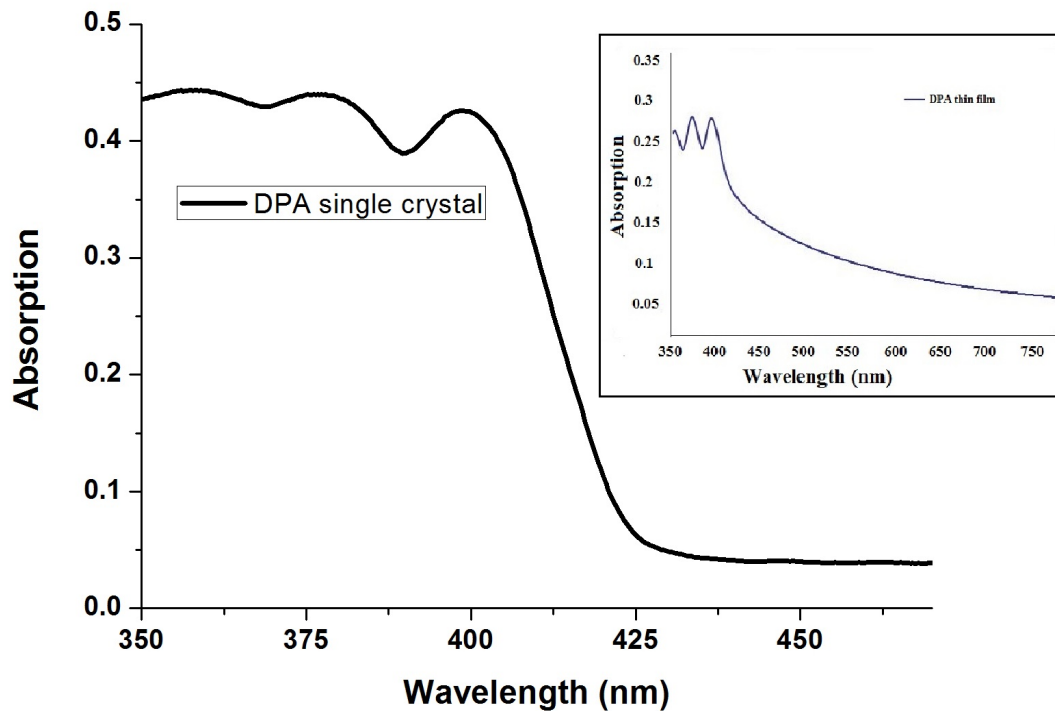
Figure 6.2.2: *UV/Visible absorption spectrum of a DPA single crystal and a DPA thin film (insert)*

measure the light coupled through a fibre, we have measured the absorption spectrum of the DPA thin film that has been used for the ellipsometry measurements, as well as a DPA single crystals grown by sublimation. The single crystal that was used for the absorption measurement was grown in the shape of a thin platelet with a width and length of about 1 cm and an estimated thickness of the magnitude of 100 μm. In figure 6.2.2 we can see a strong resonance in the absorption at around 400 nm originating in the band-edge of DPA and matching literature values [141], [142]. For shorter wavelengths crystal is absorbing, while it is transparent for longer wavelengths. The insert in figure 6.2.2 shows the absorption spectrum of the thin film, matching the structure we have observed from the single crystal. While for the single crystal a sharp drop in the absorption is observed energies lower than the band-edge, a less strong decrease for the thin film suggests strong scattering due to the quality of the film.

We can use the data obtained for the absorption spectroscopy for interpreting the ellipsometric measurement seen in figure 6.2.1. Below 450 nm the absorption is increasing, making ellipsometry difficult as the film is more and more absorbing instead of reflecting the light. For that reason data in this range cannot be used, especially as we see a rise of n with decreasing wavelength.

Knowing $n(\lambda)$ from the fitted data, we can use this to calculate the numerical aperture of the fibre for a given wavelength. We performed the experiments in following sections using the output of the RegA (800 nm), so we calculate NA for this wavelength according to equation 2.11:

$$NA = \sqrt{1.62^2 - 1.45^2} \approx 0.72$$

Further we can estimate the number of guided modes by equation 2.13 and 2.14. With $V(800nm) \approx 76.34$ the number of modes can be estimated with $M_s \approx 2913$, showing that we are in the highly multi-mode regime at 800 nm. In order to create a single-mode fibre we can calculate the core radius r_1 that is needed to create a cutoff frequency λ_c being at 800 nm or below:
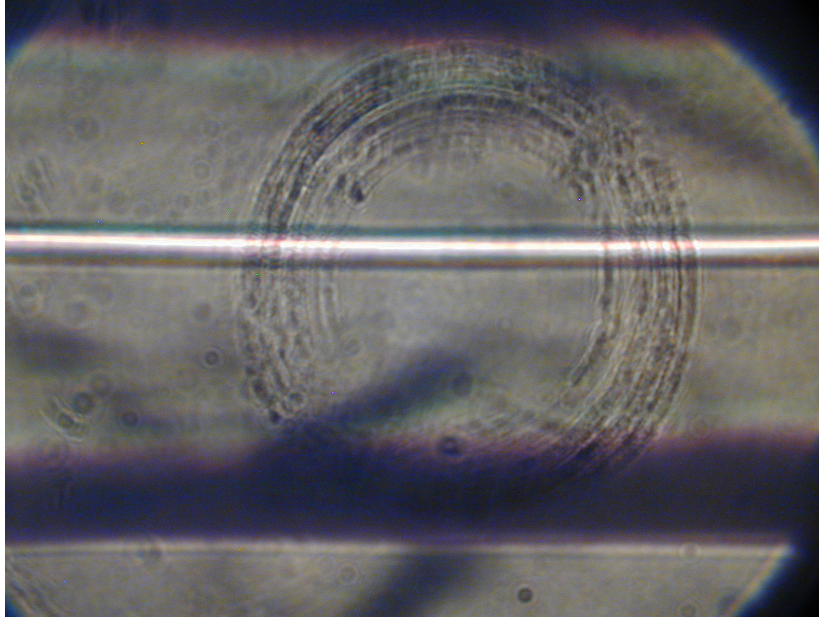
Figure 6.2.3: *Polarised microscopy picture of a 1 μm fibre filled with DPA*

$$r_1 = \frac{\lambda_c \cdot 2.405}{2\pi \cdot NA} = \frac{800nm \cdot 2.405}{2\pi \cdot 0.72} = 0.425 \mu m$$

Single-mode DPA fibre

To create a single-mode DPA fibre a new hollow core fibre capillary was drawn. While the outer diameter of the cladding was kept the same, the inner core diameter has been reduced to below 1 μm to shift the cutoff frequency to below 800 nm. For simplicity we will call these fibre the "1 μm fibre" in the following sections. The process of growing the crystal inside the 1 μm fibre is carried out in the same way as for the larger capillary fibre before. An example of the 1 μm after the filling process can be seen in figure 6.2.3 revealing a good quality also for a smaller core diameter.

6.3 Optical analysis

With the results shown in the section above, the optical properties of the filled fibre could be investigated. Appropriate objectives are used to match the numerical aperture calculated for the DPA-filled fibre above. For the laser light coupled into the fibre we have considered the absorption spectrum of DPA, as photons have to be used that are well below the absorption edge. Additionally high peak powers are desirable to observe nonlinear effects. Because of these two reasons pumping directly with the RegA at 800 nm has been chosen as a good compromise.
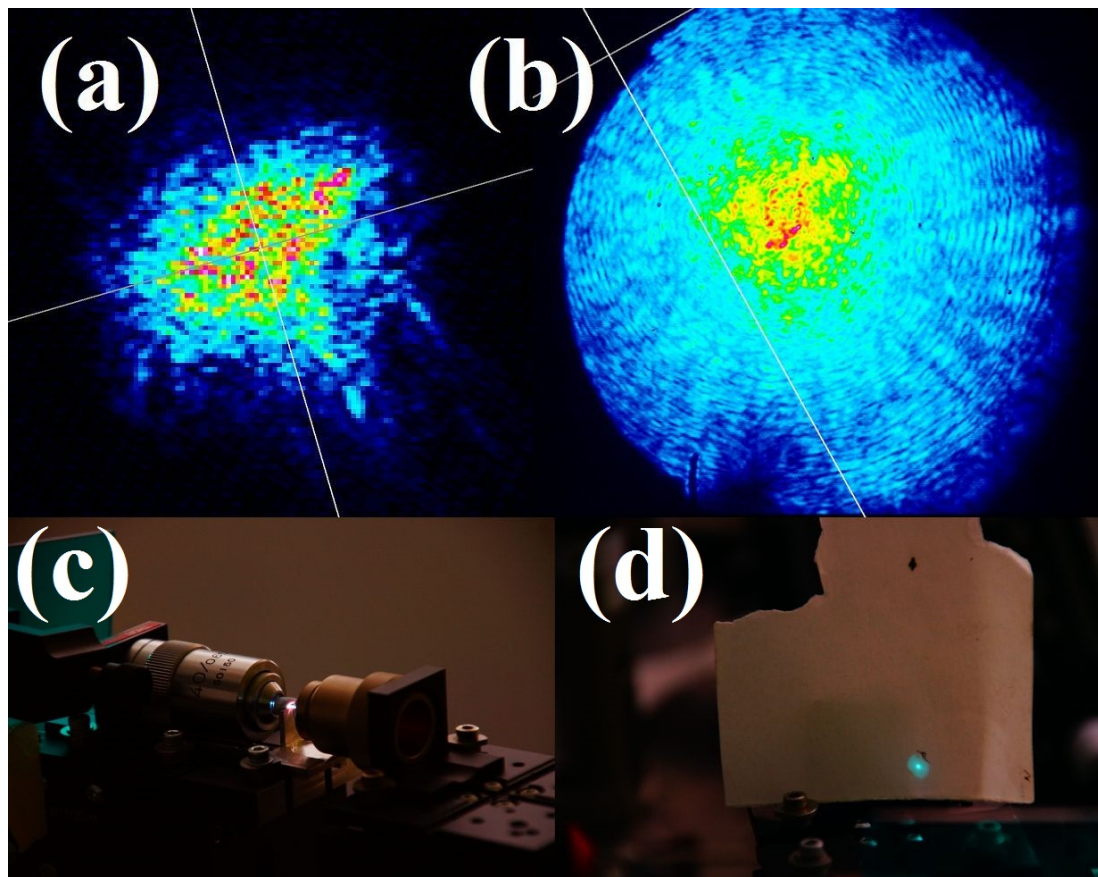
Figure 6.3.1: Beam profile of the RegA beam coupled into a DPA-filled fibre with a 13 μm core diameter in (a) and a 1 μm core diameter (b). (c) shows a photo taken of the fibre with light coupled into it through the right lens and being collimated with the objective on the left side. A photo of the collimated beam using a BG39 filter is shown in (d)

A high-NA objective is used for collimating the beam after the fibre. For investigation of the beam profile the light is focused into the beam profiler. Both the 13 µm and the 1 µm fibre have been used for these experiments and the results can be seen in figure 6.3.1 . For the 13 µm fibre a diffuse pattern is observed with a circular shape that is dominated by scattering processes. For the 1 µm fibre we observe light intensity concentrated close to the middle. A ring of higher intensity surrounds the core of the fibre. We attribute the profile here to scattering processes as well.

With the 800 nm pulse being coupled into the fibre, blue-green light can be observed leaking out of the fibre by human eye. To visualise this a picture has been taken (figure 6.3.1 (c)) with the focusing lens on the right side, the fibre in the middle and the collimating objective on the left side. Because of the high intensity of the 800 nm light we have used a *BG39* colour glass filter to eliminate residual light from the pump pulse. This let us only observe light with a wavelength shorter than ≈ 650 nm. In figure 6.3.1 (d) we can see the collimated beam after the *BG39* filter on a piece of paper. Here one can clearly notice the main intensity of the light located on a small central spot in the middle, with the surrounding showing a much lower light intensity.

As the overall intensity is much lower using the *BG39* filter, a ND filter installed in front of the CCD-detector had to be removed for the weak beam to be detected. The measured beam profile can be seen in figure 6.3.2. A sharp peak can be observed in the middle with a concentric circle of lower intensity around it. For better visualisation we have drawn a ring centred on the peak to see if it is situated exactly in the middle of the transmitted light, i.e. the position of the core.

These results suggest two different mechanisms for light travelling through the fibre. First the pump pulse is not transmitted in a guided mode, but rather in a cladding mode, with an energy leaking out of the fibre. This can result from light being not coupled into the core initially or from scattering effects inside the core. Defects in the crystal structure as well as impurities inside the crystal act as scattering centres, strongly reducing the waveguiding properties of the filled fibre. Especially the interface between the crystal core and the silica cladding might be critical.
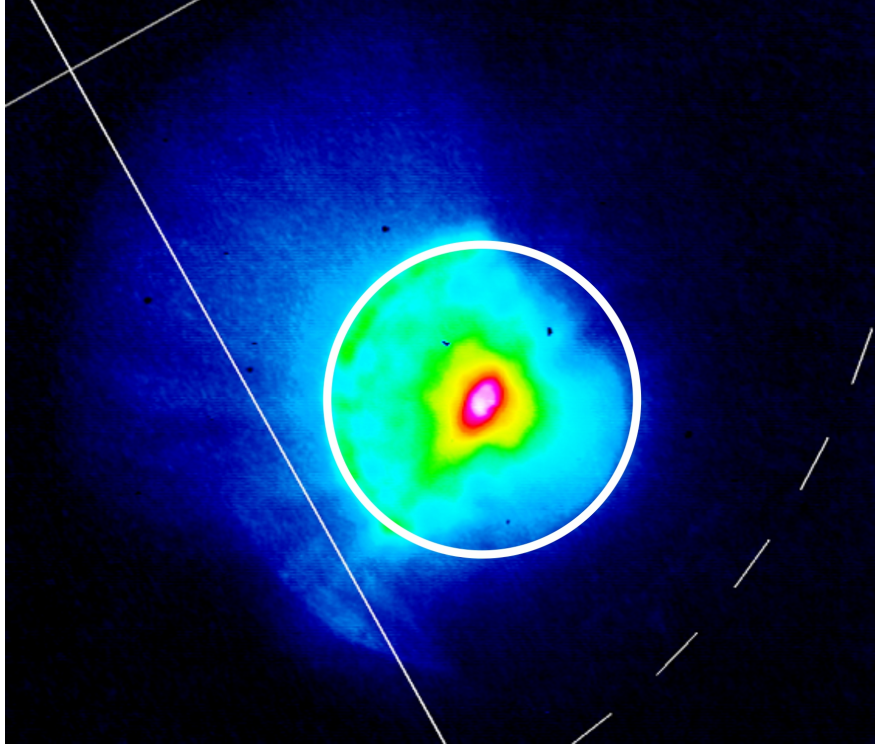
Figure 6.3.2: *Beam profile of the RegA beam coupled into a DPA-filled fibre with a 1 μm core diameter and a BG39 colour glass filter before the beam profiler showing the cross-section. A white ring has been drawn centred on the peak for visualisation.*
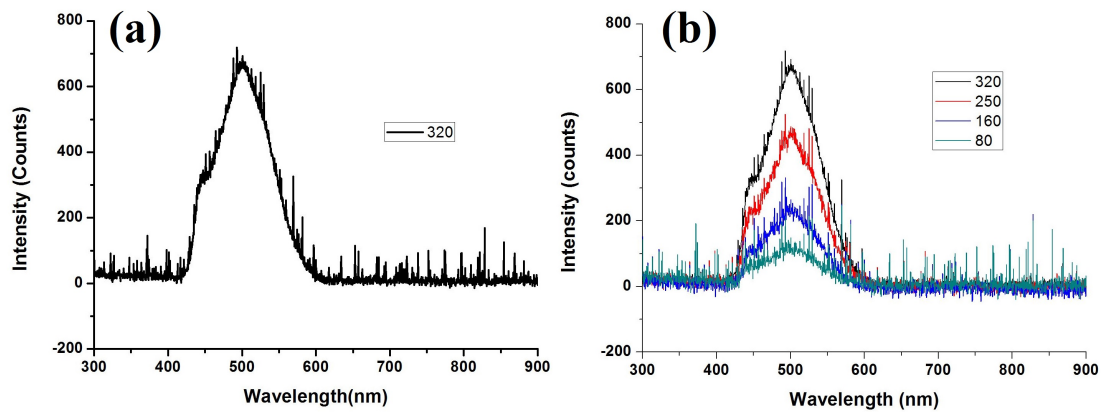
Figure 6.3.3: *Spectrum of the RegA pulse transmitted through a DPA fibre with the BG39 filter in place with an average pumping power of 320 mW (a). In (b) the spectrum is shown for varying pumping power.*

A second mechanism is observed when examining only light at shorter wavelength than the initial pump pulse. Here we have observed the main intensity sharply located in the middle. This suggests guided light inside the core. An explanation can be found in the evanescent field of the initial pump pulse that can be found inside the crystal core, even if light is transmitted in a cladding mode. Due to a nonlinear process the photon energy is changed only for photons inside the core. These photons are transmitted in a guided mode, resulting in the sharply defined beam profile as seen in figure 6.3.2.

To understand the nonlinear process occurring inside the crystal core, we keep the *BG39* filter in place after collimating the beam and send the light into a spectrometer for the visible range. The spectrum can be seen in figure 6.3.3. A strong peak centred around 500 nm can be observed with a shoulder originating of a second peak at 460 nm.

We have further measured spectra at different pump light intensities to investigate the dependence between the incoming light intensity and the spectrum. In figure 6.3.3 (b) the recorded spectrum is plotted for pump powers between 320 mW and 80 mW. We observe the change in the overall intensity of the peak seen in (a), but the shape, spectral position and width are unchanged.

131
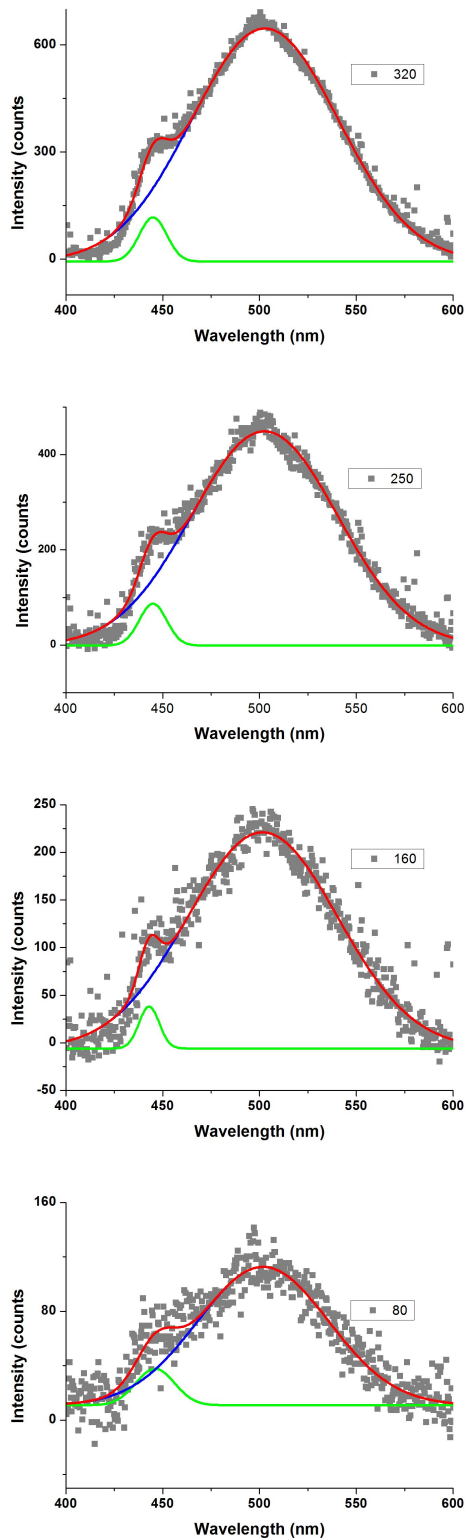
Figure 6.3.1: Recorded DPA spectrum (grey

Pump power	Centre peak 1	Width peak 1	Centre peak 2	Width peak 2
320 mW	445.0 nm	14.2 nm	502.8 nm	76.1 nm
250 mW	445.0 nm	14.1 nm	502.6 nm	75.5 nm
160 mW	443.0 nm	10.5 nm	501.7 nm	77.6 nm
80 mW	446.1 nm	20.1 nm	501.9 nm	67.6 nm

Table 6.3.1: *Values for the fitted peaks of the DPA spectrum*

The origin of these peaks lies in the vibronic, radiative transitions of the organic material, that we have explained in section 2.5.2.

For the further analysis Gaussian pulses are used to fit the experimental data. The data can be well fitted with the sum of two Gaussians as seen in figure 6.3.4 for the different pumping powers. We call the peak at the shorter wavelength peak 1 (green) and at the longer wavelength peak 2 (blue). The sum of both Gaussians (red) fits the experimental data (grey squares) in figure 6.3.4 very well.

We have summarised important values from the fitting functions in table 6.3.1 for different pumping powers. Peak 1 is centred around 445 nm with an average width of 14.7 nm while peak 2 is centred at 502 nm with an average width of 74.2 nm. For both peaks we can see small variations in the value, with the measurements for higher powers revealing a better match.

Discussion

Considering the whole set of data collected about the emission from the DPA-filled fibre, we suggest a two-photon absorption (TPA) of the DPA with a resulting fluorescence. The pump photons at 800 nm are too low in energy to be absorbed because of the band gap seen in the absorption of DPA while a two-photon process overcomes the energy difference. The excited state can relax through photo-emission to the ground state, emitting photons of shorter wavelength than the incident pump photons. Because of the centro-symmetric
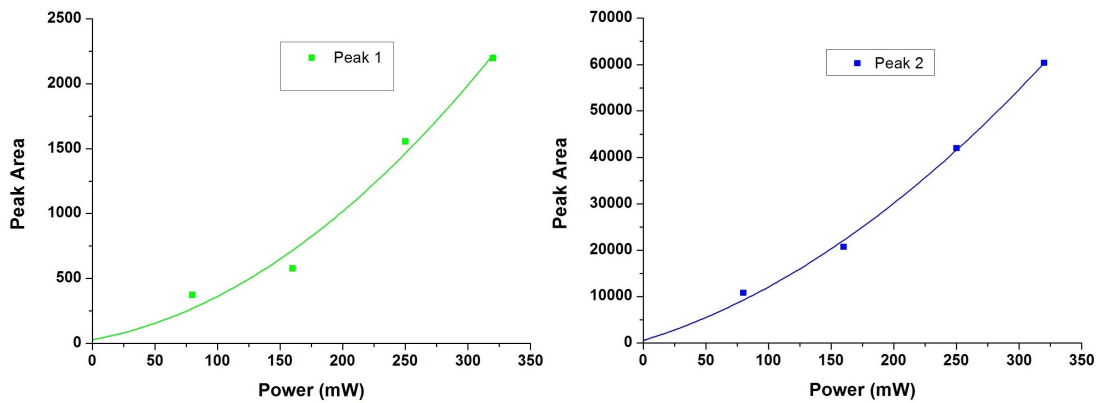
Figure 6.3.5: *Integrated peak area for fits of peak 1 (green) and 2 (blue) in figure 6.3.4 against the pumping power*

structure of the DPA crystal $\chi^{(2)}$ processes are not allowed and SHG can be excluded.

In chapter 2.5.2 we have discussed the optical properties of π-conjugated materials. In figure 2.5.8 (c) we have seen a typical absorption and emission spectrum in relation to its energy diagram. The absorption of DPA in figure 6.2.2 shows the absorption peak related to the lowest energy transition at 410 nm. The photo-emission is shifted to a longer wavelength due to non-radiative loss processes and we observe the highest energetic fluorescence peak at 445 nm. We find a good match of the position of the measured peaks with fluorescence peaks of DPA in literature [143]. In comparison we observe a reduced intensity for the 445 nm peak that we attribute to a re-absorption of photons due to the travel distance through the DPA core together with the existence of defects in the crystal structure.

The two-photon excited fluorescence process matches with the observation of the shape and position of the emission peak being independent of the pump light intensity, as it is an intrinsic material property. To evaluate the dependence on the pumping intensity we have integrated the area under the fitted peaks in figure 6.3.4 and plot the area against the pumping power in figure 6.3.5. We use the same colours as before representing peak 1 and 2.

Fitting the integrated peak area, representing the light intensity, with different functions has given the best match for a quadratic fit. The fitted function

is plotted in figure 6.3.5 as a line, while the experimental data is represented by squares. Showing a quadratic dependence on the incident light intensity confirms the explanation by TPA as we have seen the TPA transition rate to be proportional to the quadratic light intensity in equation 2.38. As can be seen further from figure 6.3.5, the fit is passing through the origin in the range of the uncertainty of the measurement and the fitted data. This shows that the intensity of the two-photon excited fluorescence goes to zero with the number if incident photons going to zero.

In conclusion we attribute the detected peak to a TPA with a consecutive photo-luminescence after non-radiative losses. This is confirmed by the quadratic dependence of the detected intensity on the pump intensity, together with the invariance of its shape in combination with literature values for DPA's strong photo-luminescence.

7 Outlook

In this thesis we have investigated possibilities of optical fibres, made out of unusual materials rather then typical silica fibres.

In chapter 4 we have build an ultrafast spectroscopy setup using an OPA as the laser source for both pumping and probing the sample. Starting from the conventional setup, we have shown that a ZBLAN fibre can be employed to create a supercontinuum that can be used as a broadband probe source instead of tuning the OPA wavelength. We have explored the generation of a SC in ZBLAN fibre and characterised the spectrum. We have then carried out time resolved pump probe measurements using the ZBLAN supercontinuum together with a monochromator for spectral selectivity. Measurements have been carried out of an organic polymer blend, demonstrating the application possibilities of the setup. Unlike silica glass, ZBLAN glass shows a better transmittance in the MIR. This opens up the possibility to create MIR broadband sources for ultrafast spectroscopy. Either by increasing the pulse power of the pump pulse or by shifting the wavelength of the pump pulse to lower energies, a usable SC could be shifted to longer wavelengths.

In the second part we were investigating not only fibres with a special glass like ZBLAN, but also fibres with a single crystal core. The experimental setup to fabricate such a fibre has been discussed in chapter 5. We have used organic semiconducting materials based on anthracene to fill a hollow core fibre with the material molten and grow single crystals inside this capillary. We have characterised the crystal inside the core using Raman-spectroscopy together with X-ray diffraction, finding a good quality single crystal. Upon launching light into the fibre we have observed two different guiding mechanisms for the initial pump light and emission from a TPA inside the crystal. While the

pump light is transmitted in a cladding mode, the light resulting from the TPA was found to be guided in the core only.

For future experiments we suggest a different geometry of the fibre: So far we have used a glass capillary with a single crystal growing in the middle of this capillary, with the idea of the crystal acting as the core and the glass capillary as the cladding. In order to overcome some of the problems we have faced with light being guided in the cladding, we propose the following structure seen in figure 7.0.1 for future work. For this a structure with regions could be used: a capillary in the middle for growing a crystal, surrounded by a glass core with high refractive index, which in turn is surrounded by a lower index glass cladding. This would allow photons to be guided inside the glass core and therefore offering a strongly increased overlap with the single crystal in its middle.

Instead of just having a fibre capillary with the single crystal acting as the core, surrounded by the silica cladding, a hollow core could be generated inside an optical fibre core with a higher refractive index, surrounded by a cladding. This would allow to overcome problems with the guiding mechanism we have found now. Confining the light inside the fibre core, while the single crystal is found in the middle of the core, would allow more efficient interaction of the confined light with the single crystal.
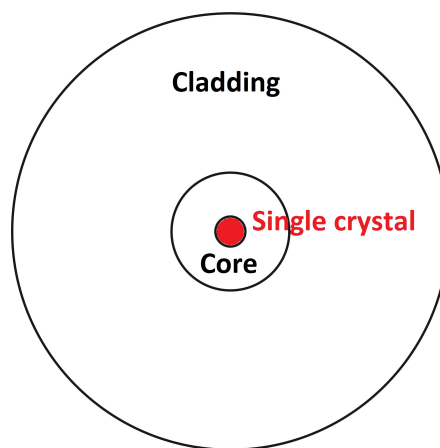
Figure 7.0.1: *Proposed structure for future work*

In conclusion, we have shown how a new optical fibre material like ZBLAN can be used to extend the applications of silica fibres. This work has given the proof of principle, but in the future the technique can be used for making NIR and MIR spectroscopic techniques more available and simplifying their use. This can be utilised to investigate many interesting effects that are found in this specific spectral region, inaccessible with silica fibres. An experimental technique for the growth of a single organic crystal has been developed, opening up possibilities for ongoing research and improvement. The improvements suggested for the geometry of the fibre capillary can further improve the efficiency of the light-matter interaction, while using organic single crystals gives rise to a vast amount of different materials that can be used in a similar experiment, using their optical properties to tailor the single-crystal fibre to the desired properties.

Chapter 7. Outlook

References

[1] Isaac Newton. *Opticks or a treatise of the reflections, refractions, inflections & colours of light*. Dover classics of science and mathematics. Dover Publ, New York, 1979.

[2] C Burgess and K. D Mielenz. *Advances in Standards and Methodology in Spectrophotometry*. Elsevier Science, Burlington, 1987.

[3] J. Michael Hollas. *Modern spectroscopy*. J. Wiley, Chichester ; Hoboken, NJ, 4th ed edition, 2004.

[4] P.U. Jepsen, D.G. Cooke, and M. Koch. Terahertz spectroscopy and imaging - Modern techniques and applications. *Laser & Photonics Reviews*, 5(1):124–166, January 2011.

[5] C. J. Benmore. A Review of High-Energy X-Ray Diffraction from Glasses and Liquids. *ISRN Materials Science*, 2012:1–19, 2012.

[6] J W M DuMond. Gamma-Ray Spectroscopy by Direct Crystal Diffraction. *Annual Review of Nuclear Science*, 8(1):163–180, December 1958.

[7] J. Michael Hollas. *Basic atomic and molecular spectroscopy*. Number 11 in Tutorial chemistry texts. Royal Society of Chemistry, Cambridge, 2002.

[8] T. H. Maiman. Stimulated Optical Radiation in Ruby. *Nature*, 187(4736):493–494, August 1960.

[9] P. A. Franken, A. E. Hill, C. W. Peters, and G. Weinreich. Generation of Optical Harmonics. *Physical Review Letters*, 7(4):118–119, August 1961.

References

[10] R. W. Terhune, P. D. Maker, and C. M. Savage. Optical Harmonic Generation in Calcite. *Physical Review Letters*, 8(10):404–406, May 1962.

[11] E.J. Woodbury and W. K. Ng. Ruby laser operation in the near IR. *Proc. IRE.*, (50):2347–2348, 1962.

[12] J. E. Geusic, H. M. Marcos, and L. G. Van Uitert. LASER OSCILLATIONS IN Nd-DOPED YTTRIUM ALUMINUM, YTTRIUM GALLIUM AND GADOLINIUM GARNETS. *Applied Physics Letters*, 4(10):182, 1964.

[13] C. Breck Hitz, J. J. Ewing, and Jeff Hecht. *Introduction to laser technology*. Wiley-IEEE Press, Hoboken, N.J, 4th ed edition, 2012.

[14] P. F. Moulton. Spectroscopic and laser characteristics of Ti:Al_2O_3. *Journal of the Optical Society of America B*, 3(1):125, January 1986.

[15] Helmut Frowein. Titan-Saphir Laser: Grundlagen und Anwendungen des wichtigsten Kurzpulslasersystems. *Optik & Photonik*, 2(1):48–53, March 2007.

[16] J. A. Giordmaine and Robert C. Miller. Tunable Coherent Parametric Oscillation in LiNb O 3 at Optical Frequencies. *Physical Review Letters*, 14(24):973–976, June 1965.

[17] Peter Hannaford, editor. *Femtosecond laser spectroscopy*. Springer, New York, NY, 2005.

[18] Ralf Menzel. *Photonics linear and nonlinear interactions of laser light and matter*. Springer, Berlin; New York, 2007.

[19] D. N. Basov, Richard D. Averitt, Dirk van der Marel, Martin Dressel, and Kristjan Haule. Electrodynamics of correlated electron materials. *Reviews of Modern Physics*, 83(2):471–541, June 2011.

[20] Felix Deschler, Enrico Da Como, Thomas Limmer, Raphael Tautz, Tillmann Godde, Manfred Bayer, Elizabeth von Hauff, Seyfullah Yilmaz, Sybille Allard, Ullrich Scherf, and Jochen Feldmann. Reduced Charge

Transfer Exciton Recombination in Organic Semiconductor Heterojunctions by Molecular Doping. *Physical Review Letters*, 107(12), September 2011.

[21] Etienne Pelletier, Alexander Sell, Alfred Leitenstorfer, and RJ Dwayne Miller. Mid-infrared optical parametric amplifier based on a LGSe crystal and pumped at 16 um. *Optics Express*, 20(25):27456, December 2012.

[22] Jingzhi Shang, Suxia Yan, Chunxiao Cong, Howe-Siang Tan, Ting Yu, and Gagik G. Gurzadyan. Probing near Dirac point electron-phonon interaction in graphene. *Optical Materials Express*, 2(12):1713, December 2012.

[23] Giti A. Khodaparast, Mithun Bhowmick, Tetsuya D. Mishima, Michael B. Santos, Caitlin Feeser, Bruce W. Wessels, and Yasuhiro H. Matsuda. Probe of coherent and quantum states in narrow-gap based semiconductors with strong spin-orbit coupling. pages 77600X–77600X–7, August 2010.

[24] Boerner Manfred. Patent: ELECTRO-OPTICAL TRANSMISSION SYSTEM UTILIZING LASERS. http://worldwide.espacenet.com/publicationDetails/biblio?CC=DE\&NR=1254513\&KC

[25] Allan W. Snyder and J. D. Love. *Optical waveguide theory*. Number 190 in Science paperbacks. Chapman and Hall, London ; New York, 1983.

[26] O.V. Butov, K.M. Golant, A.L. Tomashuk, M.J.N. van Stralen, and A.H.E. Breuls. Refractive index dispersion of doped silica for fiber optics. *Optics Communications*, 213(4-6):301–308, December 2002.

[27] Sunil Pratap Singh and Nar Singh. NONLINEAR EFFECTS IN OPTICAL FIBERS: ORIGIN, MANAGEMENT AND APPLICATIONS. *Progress In Electromagnetics Research*, 73:249–275, 2007.

[28] D. Tran, G. Sigel, and B. Bendow. Heavy metal fluoride glasses and fibers: A review. *Journal of Lightwave Technology*, 2(5):566–586, 1984.

References

[29] A Zakery and S.R Elliott. Optical properties and applications of chalcogenide glasses: a review. *Journal of Non-Crystalline Solids*, 330(1-3):1–12, November 2003.

[30] Xin Jiang, Nicolas Y. Joly, Martin A. Finger, Fehim Babic, Gordon K. L. Wong, John C. Travers, and Philip St. J. Russell. Deep-ultraviolet to mid-infrared supercontinuum generated in solid-core ZBLAN photonic crystal fibre. *Nature Photonics*, 9(2):133–139, January 2015.

[31] Christian Agger, Christian Petersen, Sune Dupont, Henrik Steffensen, Jens Kristian Lyngso, Carsten L. Thomsen, Jan Thogersen, Soren R. Keiding, and Ole Bang. Supercontinuum generation in ZBLAN fibers - detailed comparison between measurement and simulation. *Journal of the Optical Society of America B*, 29(4):635, April 2012.

[32] Guanshi Qin, Xin Yan, Chihiro Kito, Meisong Liao, Chitrarekha Chaudhari, Takenobu Suzuki, and Yasutake Ohishi. Ultrabroadband supercontinuum generation from ultraviolet to 6.28 Î¼m in a fluoride fiber. *Applied Physics Letters*, 95(16):161103, 2009.

[33] Jacek Swiderski and Maria Michalska. High-power supercontinuum generation in a ZBLAN fiber with very efficient power distribution toward the mid-infrared. *Optics Letters*, 39(4):910, February 2014.

[34] Kun Liu, Jiang Liu, Hongxing Shi, Fangzhou Tan, Yijian Jiang, and Pu Wang. High power mid-infrared supercontinuum generation in a single-mode ZBLAN fiber pumped by amplified picosecond pulses at 2 um. page 93440Z, March 2015.

[35] Weiqiang Yang, Bin Zhang, Ke Yin, Xuanfeng Zhou, and Jing Hou. High power all fiber mid-IR supercontinuum generation in a ZBLAN fiber pumped by a 2 um MOPA system. *Optics Express*, 21(17):19732, August 2013.

[36] R.S. Watt, C.F. Kaminski, and J. Hult. Generation of supercontinuum radiation in conventional single-mode fibre and its application to broad-

band absorption spectroscopy. *Applied Physics B*, 90(1):47–53, January 2008.

[37] Sune Dupont, Christian Petersen, Jan Thogersen, Christian Agger, Ole Bang, and Soren Rud Keiding. IR microscopy utilizing intense supercontinuum light source. *Optics Express*, 20(5):4887, February 2012.

[38] I Grenthe. *Nobel Lectures in Chemistry 1996-2000*. World Scientific, published for the Nobel Foundation, Singapore; River Edge, NJ, 2003.

[39] N. Thejo Kalyani and S.J. Dhoble. Organic light emitting diodes: Energy saving lighting technology - A review. *Renewable and Sustainable Energy Reviews*, 16(5):2696–2723, June 2012.

[40] Serap GÃ¼nes, Helmut Neugebauer, and Niyazi Serdar Sariciftci. Conjugated Polymer-Based Organic Solar Cells. *Chemical Reviews*, 107(4):1324–1338, April 2007.

[41] Luisa Torsi, Maria Magliulo, Kyriaki Manoli, and Gerardo Palazzo. Organic field-effect transistor sensors: a tutorial review. *Chemical Society Reviews*, 42(22):8612, 2013.

[42] Oksana Ostroverkhova, editor. *Handbook of organic materials for optical and (opto)electronic devices: properties and applications*. Number number 39 in Woodhead Publishing series in electronic and optical materials. Woodhead Publishing, Oxford, 2013.

[43] J.L. Stevenson and R.B. Dyott. Optical-fibre waveguide with a single-crystal core. *Electronics Letters*, 10(22):449, 1974.

[44] Dug Y. Kim, William E. Torruellas, Jin Kang, Christian Bosshard, George I. Stegeman, Petar Vidakovic, Joseph Zyss, W. E. Moerner, R. Twieg, and G. Bjorklund. Second-order cascading as the origin of large third-order effects in organic single-crystal-core fibers. *Optics Letters*, 19(12):868, June 1994.

References

[45] Yanyi Huang, Yong Xu, and Amnon Yariv. Fabrication of functional microstructured optical fibers through a selective-filling technique. *Applied Physics Letters*, 85(22):5182, 2004.

[46] S. Kedenburg, T. Gissibl, T. Steinle, A. Steinmann, and H. Giessen. Towards integration of a liquid-filled fiber capillary for supercontinuum generation in the 1.2-2.4 micrometer range. *Optics Express*, 23(7):8281, April 2015.

[47] P. W. Bridgman. Certain Physical Properties of Single Crystals of Tungsten, Antimony, Bismuth, Tellurium, Cadmium, Zinc, and Tin. *Proceedings of the American Academy of Arts and Sciences*, 60(6):305, 1925.

[48] Donald C. Stockbarger. The Production of Large Single Crystals of Lithium Fluoride. *Review of Scientific Instruments*, 7(3):133, 1936.

[49] J Czochralski. Ein neues Verfahren zur Messung der Kristallisationsgeschwindigkeit der Metalle" [A new method for the measurement of the crystallization rate of metals]. *Zeitschrift fuer Physikalische Chemie*, (92):219–221, 1918.

[50] James Coble Brice. *The growth of crystals from liquids*. Number 12 in Series of monographs on selected topics in solid state physics. North-Holland [u.a.], Amsterdam, 1973.

[51] Govindhan Dhanaraj, editor. *Springer handbook of crystal growth*. Springer, Heidelberg ; New York, 2010.

[52] M. E. Glicksman. *Principles of solidification: an introduction to modern casting and crystal growth concepts*. Springer Verlag, New York, 2011.

[53] R.A Laudise, Ch Kloc, P.G Simpkins, and T Siegrist. Physical vapor growth of organic semiconductors. *Journal of Crystal Growth*, 187(3-4):449–454, May 1998.

[54] E. Glockner and H.C. Wolf. The intrinsic fluorescence of the mixed crystal system anthracene-perdeuteroanthracene, amalgamated exciton band. *Chemical Physics*, 10(2-3):479–496, September 1975.

[55] S. Banerjee and A. K. Tyagi, editors. *Functional materials: preparation, processing and applications*. Elsevier insights. Elsevier, London ; Waltham, MA, 1st ed edition, 2012.

[56] Ivan Fanderlik, editor. *Silica glass and its application*. Number v. 11 in Glass science and technology. Elsevier, Amsterdam ; New York, 1991.

[57] Fu-hsi Kan. *Optical and spectroscopic properties of glass*. Springer-Verlag ; Shanghai Scientific and Technical Publishers, Berlin ; New York : Shanghai, 1992.

[58] Andrew T. Young. Rayleigh scattering. *Applied Optics*, 20(4):533, February 1981.

[59] Franz Urbach. The Long-Wavelength Edge of Photographic Sensitivity and of the Electronic Absorption of Solids. *Physical Review*, 92(5):1324–1324, December 1953.

[60] Bernard Bendow. Temperature dependence of intrinsic multiphonon absorption in crystals. *Applied Physics Letters*, 23(3):133, 1973.

[61] B. Szigeti. Compressibility and Absorption Frequency of Ionic Crystals. *Proceedings of the Royal Society A: Mathematical, Physical and Engineering Sciences*, 204(1076):51–62, November 1950.

[62] Jerzy Zarzycki and Robert W. Cahn, editors. *Materials science and technology:: a comprehensive treatment. 9: Glasses and amorphous materials*. VCH, Weinheim, 1991.

[63] K. J. Rao. *Structural chemistry of glasses*. Elsevier, Amsterdam ; New York, 1st ed edition, 2002.

[64] Mark Telford. The case for bulk metallic glass. *Materials Today*, 7(3):36–43, March 2004.

[65] Ruediger Paschotta. *Encyclopedia of laser physics and technology*. Wiley-VCH, Weinheim, 2008.

[66] John M. Senior and M. Yousif Jamro. *Optical fiber communications: principles and practice*. Financial Times/Prentice Hall, Harlow, England ; New York, 3rd ed edition, 2009.

[67] G. P. Agrawal. *Nonlinear fiber optics*. Quantum electronics–principles and applications. Elsevier / Academic Press, Amsterdam ; Boston, 4th ed edition, 2007.

[68] Dietrich Marcuse. *Theory of dielectric optical waveguides*. Quantum electronics–principles and applications. Academic Press, Boston, 2nd ed edition, 1991.

[69] John A. Buck. *Fundamentals of optical fibers*. Number 1349 in Wiley series in pure and applied optics. John Wiley & Sons, Hoboken, N.J, 2nd ed edition, 2004.

[70] R. P. Khare. *Fiber optics and optoelectronics*. Oxford University Press, New Delhi ; New York, 2004.

[71] Thiab R. Taha. A numerical scheme for the nonlinear Schroedinger equation. *Computers & Mathematics with Applications*, 22(9):77–84, 1991.

[72] Robert A. Fisher and William K. Bischel. Numerical studies of the interplay between self-phase modulation and dispersion for intense plane-wave laser pulses. *Journal of Applied Physics*, 46(11):4921, 1975.

[73] Kristian Nielsen, Danny Noordegraaf, Thorkild Sorensen, Anders Bjarklev, and Theis P Hansen. Selective filling of photonic crystal fibres. *Journal of Optics A: Pure and Applied Optics*, 7(8):L13–L20, August 2005.

[74] Yanyi Huang, Yong Xu, and Amnon Yariv. Fabrication of functional microstructured optical fibers through a selective-filling technique. *Applied Physics Letters*, 85(22):5182, 2004.

[75] John McMurry. *Organic chemistry*. Brooks/Cole, Pacific Grove, CA, 5th ed edition, 2000.

[76] Charles Kittel. *Introduction to solid state physics*. Wiley, Hoboken, NJ, 8th ed edition, 2005.

[77] Hermann Haken and Hans Christoph Wolf. *Molecular Physics and Elements of Quantum Chemistry Introduction to Experiments and Theory*. Springer Berlin Heidelberg, Berlin, Heidelberg, 2004.

[78] William M. Haynes, editor. *CRC handbook of chemistry and physics: a ready-reference book of chemical and physical data*. CRC Press, Boca Raton, Fla., 95. rev. ed edition, 2014.

[79] Rudolf Ernst Peierls. *Quantum theory of solids*. Oxford classic texts in the physical sciences. Clarendon Press ; Oxford University Press, Oxford : New York, 2001.

[80] Martin Pope and Charles E. Swenberg. *Electronic processes in organic crystals*. Number 39 in Monographs on the physics and chemistry of materials. Clarendon Press ; Oxford University Press, Oxford : New York, 1982.

[81] J. Franck and E. G. Dymond. Elementary processes of photochemical reactions. *Transactions of the Faraday Society*, 21(February):536, 1926.

[82] Edward Condon. A Theory of Intensity Distribution in Band Systems. *Physical Review*, 28(6):1182–1201, December 1926.

[83] Markus Schwoerer, Hans Christoph Wolf, and William D. Brewer. *Organic molecular solids*. Physics textbook. Wiley-VCH, Weinheim, 2007.

[84] P. W. Atkins and Julio De Paula. *Atkins' Physical chemistry*. Oxford University Press, Oxford ; New York, 9th ed edition, 2010.

[85] Michael Kasha. Characterization of electronic transitions in complex molecules. *Discussions of the Faraday Society*, 9:14, 1950.

[86] S. E. Braslavsky. Glossary of terms used in photochemistry, 3rd edition (IUPAC Recommendations 2006). *Pure and Applied Chemistry*, 79(3), January 2007.

[87] Robert Hull and Institution of Electrical Engineers, editors. *Properties of crystalline silicon*. Number 20 in EMIS datareviews series. INSPEC, London, 1999.

[88] S. Alvarado, P. Seidler, D. Lidzey, and D. Bradley. Direct Determination of the Exciton Binding Energy of Conjugated Polymers Using a Scanning Tunneling Microscope. *Physical Review Letters*, 81(5):1082–1085, August 1998.

[89] H. Baessler, V.I. Arkhipov, E.V. Emelianova, A. Gerhard, A. Hayer, C. Im, and J. Rissler. Excitons in Pi-conjugated polymers. *Synthetic Metals*, 135-136:377–382, April 2003.

[90] Jean-Luc Bredas, David Beljonne, Veaceslav Coropceanu, and Jerome Cornil. Charge-Transfer and Energy-Transfer Processes in Pi-Conjugated Oligomers and Polymers: A Molecular Picture. *Chemical Reviews*, 104(11):4971–5004, November 2004.

[91] T. Holstein. Studies of Polaron Motion. *Annals of Physics*, 281(1-2):706–724, April 2000.

[92] J. T. Devreese. Polarons. volume 678, pages 3–56. AIP, 2003.

[93] L.D. Landau. ueber Die Bewegung der Elektronen in Kristallgitter. *Phys. Z. Sowjetunion*, Vol. 3:pp. 644–645., 1933.

[94] Ch Bosshard, editor. *Organic nonlinear optical materials*. Number v. 1 in Advances in nonlinear optics. Gordon and Breach, Basel, Switzerland, 1995.

[95] J. L. Oudar and J. Zyss. Structural dependence of nonlinear-optical properties of methyl-(2,4-dinitrophenyl)-aminopropanoate crystals. *Physical Review A*, 26(4):2016–2027, October 1982.

[96] J.L. Oudar and D.S. Chemla. Theory of second-order optical suscep-tibilities of benzene substitutes. *Optics Communications*, 13(2):164–168, February 1975.

[97] A. Dulcic and C. Sauteret. The regularities observed in the second order hyperpolarizabilities of variously disubstituted benzenes. *The Journal of Chemical Physics*, 69(8):3453, 1978.

[98] R.A. Huijts and G.L.J. Hesselink. Length dependence of the second-order polarizability in conjugated organic molecules. *Chemical Physics Letters*, 156(2-3):209–212, March 1989.

[99] Frank Wuerthner, Franz Effenberger, Ruediger Wortmann, and Peter Kraemer. Second-order polarizability of donor-acceptor substituted olig-othiophenes: substituent variation and conjugation length dependence. *Chemical Physics*, 173(2):305–314, June 1993.

[100] J. W. Wu, J. R. Heflin, R. A. Norwood, K. Y. Wong, O. Zamani-Khamiri, A. F. Garito, P. Kalyanaraman, and J. Sounik. Nonlinear-optical processes in lower-dimensional conjugated structures. *Journal of the Optical Society of America B*, 6(4):707, April 1989.

[101] J. R. Heflin, K. Y. Wong, O. Zamani-Khamiri, and A. F. Garito. Nonlin-ear optical properties of linear chains and electron-correlation effects. *Physical Review B*, 38(2):1573–1576, July 1988.

[102] K.C. Rustagi and J. Ducuing. Third-order optical polarizability of conju-gated organic molecules. *Optics Communications*, 10(3):258–261, March 1974.

[103] D. C. Hutchings and E. W. Van Stryland. Nondegenerate two-photon absorption in zinc blende semiconductors. *Journal of the Optical Society of America B*, 9(11):2065, November 1992.

[104] Joel M. Hales, David J. Hagan, Eric W. Van Stryland, K. J. Schafer, A. R. Morales, K. D. Belfield, P. Pacher, O. Kwon, E. Zojer, and J. L. Bredas.

Resonant enhancement of two-photon absorption in substituted fluorene molecules. *The Journal of Chemical Physics*, 121(7):3152, 2004.

[105] Olga V. Przhonska, Scott Webster, Lazaro A. Padilha, Honghua Hu, Alexey D. Kachkovski, David J. Hagan, and Eric W. Van Stryland. Two-Photon Absorption in Near-IR Conjugated Molecules: Design Strategy and Structure-Property Relations. In Alexander P. Demchenko, editor, *Advanced Fluorescence Reporters in Chemistry and Biology I*, volume 8, pages 105–147. Springer Berlin Heidelberg, Berlin, Heidelberg, 2010.

[106] Herbert Rabin, Chung Liang Tang, and N. Bloembergen, editors. *Quantum electronics: a treatise*. Academic Press, New York, 1975.

[107] Randy Wayne. *Light and video microscopy*. Elsevier, Academic Press, Amsterdam, 2nd edition edition, 2014.

[108] ZEISS Microscopy Online Campus | Live-Cell Imaging | Microscopy Techniques.

[109] Agilent. AGILENT CARY 4000/5000/6000i SERIES UV-VIS-NIR SPEC-TROPHOTOMETERS.

[110] Inc. J.A. Woollam Co. CompleteEASE Data Analysis Manual, 2011.

[111] *Operator's Manual The Coherent RegA 9000*.

[112] PCDTBT | Sigma-Aldrich http://www.sigmaaldrich.com/catalog/product/aldrich/75399

[113] [60]PCBM by Solenne BV http://www.solennebv.com/60pcbm.htm.

[114] Yingying Wang, Meshaal Alharbi, Thomas D. Bradley, Coralie Fourcade-Dutin, Benoit Debord, Benoit Beaudou, Frederic Gerome, and Fetah Benabid. Hollow-core photonic crystal fibre for high power laser beam delivery. *High Power Laser Science and Engineering*, 1(01):17–28, March 2013.

[115] M. L. Meade. *Lock-in amplifiers: principles and applications*. Number 1 in IEE electrical measurement series. P. Peregrinus on behalf of the Institution of Electrical Engineers, London, 1983.

[116] Robert R. Alfano, editor. *The supercontinuum laser source: fundamentals with updated references*. Springer, New York, 2nd ed edition, 2006.

[117] F. Silva, D.R. Austin, A. Thai, M. Baudisch, M. Hemmer, D. Faccio, A. Couairon, and J. Biegert. Multi-octave supercontinuum generation from mid-infrared filamentation in a bulk crystal. *Nature Communications*, 3:807, May 2012.

[118] Stefan Fischbach, Andrey V. Gorbach, Daniele Di Nuzzo, and Enrico Da Como. Near infrared ultrafast pump-probe spectroscopy with ZrF4-BaF2-LaF3-AlF3-NaF fiber supercontinuum. *Applied Physics Letters*, 107(2):021103, July 2015.

[119] John M. Dudley, Rim Cherif, Stephane Coen, and Goery Genty. Ultrafast Nonlinear Fibre Optics and Supercontinuum Generation. In Robert Thomson, Christopher Leburn, and Derryck Reid, editors, *Ultrafast Nonlinear Optics*, pages 177–193. Springer International Publishing, Heidelberg, 2013.

[120] Xiushan Zhu and N. Peyghambarian. High-Power ZBLAN Glass Fiber Lasers: Review and Prospect. *Advances in OptoElectronics*, 2010:1–23, 2010.

[121] Kun Liu, Jiang Liu, Hongxing Shi, Fangzhou Tan, and Pu Wang. High power mid-infrared supercontinuum generation in a single-mode ZBLAN fiber with up to 21.8 W average output power. *Optics Express*, 22(20):24384, October 2014.

[122] Mariusz Klimczak, Grzegorz Sobon, Rafal Kasztelanic, Krzysztof M. Abramski, and Ryszard Buczynski. Direct comparison of shot-to-shot noise performance of all normal dispersion and anomalous dispersion

supercontinuum pumped with sub-picosecond pulse fiber-based laser. *Scientific Reports*, 6:19284, January 2016.

[123] What is a fluoride fiber ? https://www.fiberlabs-inc.com/technology/.

[124] M.K. Reed and M.K.S. Shepard. Tunable infrared generation using a femtosecond 250 kHz Ti:sapphire regenerative amplifier. *IEEE Journal of Quantum Electronics*, 32(8):1273–1277, August 1996.

[125] D. V. Skryabin and A. V. Gorbach. Theory of supercontinuum and interaction of solitons with dispersive waves. In J. M. Dudley and J. R. Taylor, editors, *Supercontinuum Generation in Optical Fibers*, pages 178–198. Cambridge University Press, Cambridge, 2010.

[126] Irnis Kubat, Christian S. Agger, Peter Morten Moselund, and Ole Bang. Mid-infrared supercontinuum generation to 4.5 um in uniform and tapered ZBLAN step-index fibers by direct pumping at 1064 or 1550 nm. *Journal of the Optical Society of America B*, 30(10):2743, October 2013.

[127] Fabian Etzold, Ian A. Howard, Nina Forler, Don M. Cho, Michael Meister, Hannah Mangold, Jie Shu, Michael Ryan Hansen, Klaus Muellen, and Frederic Laquai. The Effect of Solvent Additives on Morphology and Excited-State Dynamics in PCPDTBT:PCBM Photovoltaic Blends. *Journal of the American Chemical Society*, 134(25):10569–10583, June 2012.

[128] Daniele Di Nuzzo, Daniele Viola, Florian S. U. Fischer, Giulio Cerullo, Sabine Ludwigs, and Enrico Da Como. Enhanced Photogeneration of Polaron Pairs in Neat Semicrystalline Donor-Acceptor Copolymer Films via Direct Excitation of Interchain Aggregates. *The Journal of Physical Chemistry Letters*, 6(7):1196–1203, April 2015.

[129] Raphael Tautz, Enrico Da Como, Christian Wiebeler, Giancarlo Soavi, Ines Dumsch, Nils Froehlich, Giulia Grancini, Sybille Allard, Ullrich Scherf, Giulio Cerullo, Stefan Schumacher, and Jochen Feldmann. Charge Photogeneration in Donor-Acceptor Conjugated Materials: Influence

of Excess Excitation Energy and Chain Length. *Journal of the American Chemical Society*, 135(11):4282–4290, March 2013.

[130] I.W. Hwang, C. Soci, D. Moses, Z. Zhu, D. Waller, R. Gaudiana, C.J. Brabec, and A.J. Heeger. Ultrafast Electron Transfer and Decay Dynamics in a Small Band Gap Bulk Heterojunction Material. *Advanced Materials*, 19(17):2307–2312, September 2007.

[131] G. Grancini, M. Maiuri, D. Fazzi, A. Petrozza, H-J. Egelhaaf, D. Brida, G. Cerullo, and G. Lanzani. Hot exciton dissociation in polymer solar cells. *Nature Materials*, 12(1):29–33, December 2012.

[132] Dmitry V. Skryabin and Andrey V. Gorbach. *Colloquium* : Looking at a soliton through the prism of optical supercontinuum. *Reviews of Modern Physics*, 82(2):1287–1299, April 2010.

[133] Harry Figi, Mojca JazbinÅ¡ek, Christoph Hunziker, Manuel Koechlin, and Peter GÃ¼nter. Electro-optic single-crystalline organic waveguides and nanowires grown from the melt. *Optics Express*, 16(15):11310, July 2008.

[134] F. H. Babai, R. B. Dyott, and E. A. D. White. Crystal growth of organic materials in glass capillaries. *Journal of Materials Science*, 12(5):869–872, May 1977.

[135] R. Balasubramanian, K.B.R. Varma, and A. Selvarajan. Growth and characterization of single crystal cored fibers (SCCF) of novel nonlinear organic optical materials. *Journal of Crystal Growth*, 151(1-2):140–144, May 1995.

[136] B. K. Nayar. Nonlinear Optical Interactions in Organic Crystal Cored Fibers. In David J. Williams, editor, *Nonlinear Optical Properties of Organic and Polymeric Materials*, volume 233, pages 153–166. AMERICAN CHEMICAL SOCIETY, WASHINGTON, D.C., September 1983. DOI: 10.1021/bk-1983-0233.ch007.

[137] Sigma-Aldrich Raman DPA http://www.sigmaaldrich.com/spectra/rair/RAIR012801.PDF

[138] N. Abasbegovic, N. Vukotic, and L. Colombo. Raman Spectrum of Anthracene. *The Journal of Chemical Physics*, 41(9):2575, 1964.

[139] Norman B. Colthup, Lawrence H. Daly, and Stephen E. Wiberley. *Introduction to infrared and Raman spectroscopy*. Academic Press, Boston, 3rd ed edition, 1990.

[140] A.K. Tripathi, M. Heinrich, T. Siegrist, and J. Pflaum. Growth and Electronic Transport in 9,10-Diphenylanthracene Single Crystals - An Organic Semiconductor of High Electron and Hole Mobility. *Advanced Materials*, 19(16):2097–2101, August 2007.

[141] Ryohei Yamakado, Shin-ichi Matsuoka, Masato Suzuki, Daisuke Takeuchi, Hyuma Masu, Isao Azumaya, and Koji Takagi. Synthesis, reaction, and optical properties of cyclic oligomers bearing 9,10-diphenylanthracene based on an aromatic tertiary amide unit. *RSC Advances*, 4(13):6752, 2014.

[142] Roberto Vadrucci, Christoph Weder, and Yoan C. Simon. Low-power photon upconversion in organic glasses. *Journal of Materials Chemistry C*, 2(16):2837, 2014.

[143] H. W. Offen. Fluorescence Spectra of Several Aromatic Crystals under High Pressures. *The Journal of Chemical Physics*, 44(2):699, 1966.

Appendix

Acronyms

Abbreviation	Full name
AOM	acousto-optic modulator
BBO	beta-barium borate
BP	band pass filter
BPA	9,10-Bis(phenylethynyl)anthracene
BS	beam splitter
CD	cavity dumper
DPA	9,10-Diphenyl-anthracene
DPSS	diode-pumped solid state laser
GVD	group velocity dispersion
HMF	heavy metal fluorides
HOMO	highest occupied molecular orbital
IR	infrared
LP	Lone pair
LUMO	lowest unoccupied molecular orbital
MIR	mid-infrared
NIR	near-infrared
ND	neutral density
NLO	nonlinear optics
NLSE	nonlinear Schroedinger equation
PCBM[60]	[6,6]-phenyl-C61 butyric acid methyl ester

PCDTBT	Poly[N-9'-heptadecanyl-2,7-carbazole-alt-5,5-(4',7'-di-2-thienyl-2',1',3'-benzothiadiazole)], Poly[[9-(1-octylnonyl)-9H-carbazole-2,7-diyl]-2,5-thiophenediyl-2,1,3-benzothiadiazole-4,7-diyl-2,5-thiophenediyl]
OPA	optical parametric amplifier
QS	Q-switch
SA	strong anti-binding
SB	strong binding
SC	supercontinuum
SHG	second harmonic generation
SNR	signal-to-noise ratio
SPM	self-phase modulation
SRS	stimulated Raman scattering
SSFM	split-step Fourier method
TE	transverse electrical
Ti:Sa	titanium:sapphire
TIR	total internal reflection
TM	transverse magnetical
TPA	two-photon absorption
WA	weak anti-binding
WB	weak binding
WL	white light
XFROG	cross-correlated frequency-resolved optical gating
XPM	cross-phase modulation
ZD	zero dispersion
ZBLAN	$55 ZrF_4$, $18 BaF_2$, $6 LaF_3$, $4 AlF_3$, $17 Na_F$

List of Publications

Journal Publications

S. Fɪsᴄʜʙᴀᴄʜ, A. V. Gᴏʀʙᴀᴄʜ, D. Dɪ Nᴜᴢᴢᴏ, E. Dᴀ Cᴏᴍᴏ. Near infrared ultrafast pump-probe spectroscopy with ZrF4-BaF2-LaF3-AlF3- NaF fiber supercontinuum. *Applied Physics Letters*, 107(2):021103, July 2015.

S. Fɪsᴄʜʙᴀᴄʜ, S. Mɪʟʟᴇʀ, S. Cᴀʙᴀssɪ, R. Pᴜʀᴋɪss, P.J. Mᴏsʟᴇʏ, E. Dᴀ Cᴏᴍᴏ Hybrid fibers with organic single crystal core (in preparation)

Conferences and Worshops

S. Fɪsᴄʜʙᴀᴄʜ, E. Dᴀ Cᴏᴍᴏ. Ultrafast spectroscopy of few layer graphene. *Symposium on 2D Materials for Optoelectronics, Plasmonics and Photonics*

S. Fɪsᴄʜʙᴀᴄʜ, E. Dᴀ Cᴏᴍᴏ. A novel design for ultrafast optical infrared spectroscopy. *Research afternoon University of Bath*

S. Fɪsᴄʜʙᴀᴄʜ, E. Dᴀ Cᴏᴍᴏ. Optical spectroscopy of graphene and 2d materials. *Nanoscience group Bath*

S. Fɪsᴄʜʙᴀᴄʜ, S. Mɪʟʟᴇʀ, E. Dᴀ Cᴏᴍᴏ. ZBLAN fibre for pump probe spectroscopy and crystal filled hollow core fibres. *Centre for Photonics and Photonic Materials Bath*